INVESTIGATIONS SUR LES DÉVIATIONS EXPÉRIMENTALES GÉOMÉTRIQUES DU PROCÉDÉ 3DP-LPBF

par

Teega Wende Floriane Régina ZONGO

THÈSE PAR ARTICLES PRÉSENTÉE À L'ÉCOLE DE TECHNOLOGIE SUPÉRIEURE COMME EXIGENCE PARTIELLE À L'OBTENTION DU DOCTORAT EN GÉNIE
Ph. D.

MONTRÉAL, LE 19 DÉCEMBRE 2019

ÉCOLE DE TECHNOLOGIE SUPÉRIEURE
UNIVERSITÉ DU QUÉBEC

PRÉSENTATION DU JURY

CETTE THÈSE A ÉTÉ ÉVALUÉE
PAR UN JURY COMPOSÉ DE :

M. Souheil-Antoine TAHAN, ing., Ph.D., Directeur de Thèse
Département de Génie mécanique à l'École de Technologie supérieure

M. Vladimir BRAILOVSKI, ing., Ph.D., Co-Directeur de Thèse
Département de Génie mécanique à l'École de Technologie supérieure

M. Louis RIVEST, ing., Ph.D., président du Jury
Département de Génie des systèmes à l'École de Technologie supérieure

M. Martin VIENS, ing., Ph.D., membre du jury
Département de Génie mécanique à l'École de Technologie supérieure

M. Farbod KHAMENEIFAR, ing., Ph.D., membre du jury indépendant
Département de Génie Mécanique, Polytechnique Montréal

ELLE A FAIT L'OBJET D'UNE SOUTENANCE DEVANT JURY ET PUBLIC

LE 16 DÉCEMBRE 2019

À L'ÉCOLE DE TECHNOLOGIE SUPÉRIEURE

REMERCIEMENTS

Je tiens à remercier mes directeurs de thèse, les professeurs Antoine Tahan et Vladimir Brailovski pour leur grande aide et le soutien permanent dont j'ai bénéficié pendant la thèse. Je tiens à vous remercier pour votre disponibilité, votre accessibilité, votre complémentarité, votre résilience quand il le fallait, votre conciliance et plus particulièrement pour vos conseils. Merci encore, j'ai beaucoup appris à vos côtés.

De plus, j'aimerais remercier le Conseil de recherches en sciences naturelles et en génie du Canada (CRSNG) et l'École de Technologie supérieure (ÉTS) pour leur soutien et leur contribution financière, qui m'ont permis de concentrer la majorité de mon temps à mes activités de recherches.

J'adresse également mes très sincères remerciements à M. Louis RIVEST, Président du jury. J'exprime également mes remerciements à tous les membres du jury d'avoir bien voulu examiner et juger ce travail de recherche.

Je remercie également tous les ami(e)s et collègues de l'ÉTS ainsi que les membres passés et présents du Laboratoire LAMSI.

Je remercie du plus profond de mon cœur ma magnifique famille. Ma chère mère Jeanne Lingane et mon cher père Antoine Zongo, pour leur infaillible soutien et leur constant encouragement ainsi que ma sœur Bénédicte et mon frère Victorien bien aimés pour leur soutien moral.

Merci à mes très chers amis pour votre soutien indéfectible surtout dans les moments difficiles que j'ai rencontrés en cette fin de thèse. Vous êtes ma deuxième famille.

INVESTIGATIONS SUR LES DÉVIATIONS EXPÉRIMENTALES GÉOMÉTRIQUES DU PROCÉDÉ 3DP-LPBF

Floriane ZONGO

RÉSUMÉ

Ce projet s'inscrit dans le domaine de la fabrication additive (FA), plus précisément, il vise l'identification des performances dimensionnelles du procédé de *Laser Powder Bed Fusion* (LPBF) ou fusion sélective par laser. Les travaux portent sur l'identification du retrait dimensionnel et la quantification des variations dimensionnelles et géométriques sur les pièces issues de ce procédé.

Le procédé LPBF étant relativement jeune, il n'existe que très peu d'informations ou de normes qui abordent la capabilité de ce procédé. Dans une démarche de 'Conception pour fabrication' (*Design for Manufacturing*), la connaissance *a priori* des performances dimensionnelles du procédé LPBF est incontournable. Ce projet se propose de les étudier et de les quantifier.

Le premier jalon de notre recherche consiste à mesurer et à quantifier l'effet de la position de la pièce produite dans la chambre de fabrication sur les déviations dimensionnelles. Le but de la démarche est de déceler l'existence d'un motif de distribution des erreurs afin de compenser l'erreur systématique, et de proposer un guide de positionnement aux concepteurs qui interviennent dans le domaine. Ce jalon consiste également à quantifier l'inter (d'une impression à une autre) et l'intra (plusieurs composants identiques dans la même impression) répétabilité du procédé. Cette étape a fait l'objet d'une publication dans un journal avec comité de lecture. « *Intra- and Inter-Repeatability of Profile Deviations of an AlSi10Mg Tooling Component Manufactured by Laser Powder Bed Fusion », Journal of Manufacturing and Materials Processing, 2018, 2(3), 56-70.*

Le second jalon consiste à quantifier les effets d'échelle et de la répartition de la matière sur les déviations dimensionnelles et géométriques. Ce jalon quantifie également les effets du post traitement que subit la pièce après fabrication, soit le traitement thermique de relaxation des contraintes, le détachement des pièces de la plaque de fabrication et le nettoyage de la pièce par projection de matière sur sa surface. Cette étude a fait l'objet d'une deuxième publication dans un journal avec comité de lecture avec le titre de « *Scale, Material Concentration, Stress Relief and Part Removal Effects on the Dimensional Behaviour of Selected AlSi10Mg Components Manufactured by Laser Powder Bed Fusion* », *Journal of Manufacturing and Materials Processing, 2019, 3(2), 49-67.*

Le troisième jalon est une investigation expérimentale de la capacité de prédiction d'un simulateur numérique du procédé. En effet, après la mise sur le marché du logiciel *ANSYS Additive Print* par ANSYS inc., et dont l'une des fonctionnalités est justement de prédire les déviations géométriques du procédé LPBF, nous avons jugé intéressant de valider ses performances en comparant les prédictions numériques avec les déviations telles que mesurées expérimentalement. Nous avons donc conçu des pièces spécifiquement pour l'étude. Cette

investigation a fait l'objet d'une présentation orale à la première conférence canadienne sur la FA, (HI AM 2019), et d'une publication dans un journal avec comité de lecture, avec le titre de « *Geometric deviations of laser powder bed fused AlSi10Mg components: Numerical Predictions versus Experimental Measurements* ». *Additive Manufacturing Journal, article soumis.*

Le quatrième jalon de cette étude s'articule autour de la construction d'un modèle prédictif simple des déviations dimensionnelles des pièces issues du procédé. Le modèle est basé sur des métriques qui estiment les déviations dimensionnelles en fonction du niveau de concentration (ou répartition) de la matière tout en tenant compte de l'effet d'échelle. Nous présentons les résultats du modèle et nous comparons ses performances avec les simulations numériques et les mesures expérimentales.

Mots clés – Fabrication additive, *Laser Powder Bed Fusion*, fusion sur lit de poudre, capabilité des procédés, complexité, métrologie, GD&T.

INVESTIGATIONS ON GEOMETRICAL EXPERIMENTAL DEVIATIONS OF THE 3DP-LPBF PROCESS

Floriane ZONGO

ABSTRACT

This project applies in the field of additive manufacturing (FA). More exactly, it aims of the identification of Laser Powder Bed Fusion (LPBF), or selective laser melting process (3DP-LPBF) performances. Within the framework of the present project, we are interested in the shrinkage and in the dimensional and geometrical variations, which intervenes on parts stemming from this process. LPBF processes are relatively young, and because of a lack of data, there is only small amount of information or standards, which address the process capability. The knowledge of the dimensional performances of the process LPBF is essential in a 'Design for Manufacturing' process. This project propose to study and quantify them.

The first step of this research project consists of quantifying the parts position on the manufacturing chamber effect on the geometrical and dimensional deviations. The aim of the approach is to detect a deviation distribution pattern in the chamber and propose a positioning guide to the designers. The first step also consists of quantifying the process inter (from one impression to another) and intra (identical components in the same impression) repeatability. This step has been the subject of a first publication in a peer-reviewed journal. « Intra- and Inter-Repeatability of Profile Deviations of an AlSi10Mg Tooling Component Manufactured by Laser Powder Bed Fusion *» Journal of Manufacturing and Materials Processing, 2018, 2(3), 56-70.*

The second step consisted of quantifying the material repartition effect, along with the scale effect on the dimensional and geometrical deviations of the parts. This step also consisted on quantifying the process post-treatment steps effects on the printed distortions, which are the stress-relieving heat treatment, the part removal from the build plate, and the shot peening. This step has been the subject of a second publication in a peer-reviewed journal. « Scale, Material Concentration, Stress Relief and Part Removal Effects on the Dimensional Behaviour of Selected AlSi10Mg Components Manufactured by Laser Powder Bed Fusion », *Journal of Manufacturing and Materials Processing, 2019, 3(2), 49-67.*

With the arrival of ANSYS Additive (by ANSYS incorporation) , which one of the functionalities is to predict the geometrical deviations of LPBF, we found interesting to validate its performances through numerically predicted and experimentally measured distortions comparison of artifacts designed and printed for the case study. This step has been the subject of an oral presentation at the HI AM conference, and a publication in a peer-reviewed journal. « Geometric deviations of laser powder bed fused AlSi10Mg components: Numerical Predictions versus Experimental Measurements » *Additive Manufacturing Journal, submitted article*.

The fourth step of this study consists on successively implement the quantified effect on a model to predict LPBF parts dimensional deviations. The model is based on metrics that estimate the dimensional deviations based on the material repartition (or concentration), which implicitly takes in account the scale effect. We present the results of the model and compare its performance with other numerical simulations and experimental measurements.

Key words – Additive manufacturing, Laser Powder Bed Fusion, selective laser melting, process capability, complexity, metrology, GD&T.

TABLE DES MATIÈRES

Page

LISTE DES TABLEAUX

LISTE DES FIGURES

LISTE DES ABRÉVIATIONS, SIGLES ET ACRONYMES

3DP	*Three Dimensional Printing*
LPBF	*Laser Powder Bed Fusion*
CAO	Conception assistée par ordinateur
AM	*Additive Manufacturing*
FA	Fabrication additive
FDM	*Fused Deposition Modeling*
SLM	*Selective Laser Melting*
DFM	*Design for Manufacturing*
CMM	*Coordinate Measuring Machine*
NPCDF	*Non Parametric Cumulative Deviation Function*
GD&T	*Geometric and Dimensionning Tolerancing*

INTRODUCTION

Selon la norme ISO/ASTM52901-16 [1], « *la fabrication additive (FA) est un procédé de mise en forme d'une pièce par ajout de matière, par empilement de couches successives ».* Cette norme décrit les principes généraux des différents procédés de la famille de la FA. Leur terminologie est régie par la norme ISO/ASTM 52900:2017 [2].

Après un léger déclin en 2009, le marché de la FA a connu une croissance continue et soutenue durant les dix dernières années. La croissance moyenne des revenus générés par la FA durant les 30 dernières années est de 26.9% selon le Wohlers report de 2019. En 2017, les revenus générés sont de l'ordre de $7 336 milliards. Ils ont augmenté de 33.5% pour atteindre $9 795 milliards en 2018. Le Canada n'est pas en reste de cette expansion. Le Gouvernement fédéral du Canada continue de considérer la promotion de la FA comme une priorité. Il a investi plus de $200 millions dans NGen, un organisme sans but lucratif pour promouvoir la technologie. Le Gouvernement du Québec a également investi $20 millions pour supporter Tekna, une entreprise qui fabrique de la poudre métallique pour la FA. Le *Holistic Innovation in Additive Manufacturing*, premier réseau de FA canadien a organisé sa première conférence à l'Université de Waterloo à Vancouver en juin 2019.

En 2016, parmi les 7 familles de procédés de la FA, 4 utilisaient comme matériau le métal : la projection de liant, la stratification, la fusion/friction sur lit de poudre et le dépôt de matériau sous énergie concentrée. Ce nombre est passé à 6 en 2019 quand l'extrusion de matière et la projection de matériau sont entrées dans le rang des procédés de FA métallique.

La croissance des revenus de la branche métallique de la FA est encore soutenue. En 2015, les revenus enregistrés étaient de l'ordre de $88,1 millions. Ce chiffre est passé à $126,8 millions en 2016, $183.4 millions de 2017, pour atteindre $260,2 millions en 2018, soit une croissance annuelle de 41.9% selon le Wohlers Report 2019. Cette croissance s'explique principalement par l'adaptation de nouveaux matériaux pour la FA, mais aussi par l'adaptation de techniques de FA déjà existantes pour les matériaux métalliques.

Le présent projet étudie le procédé de la fusion sur lit de poudre (FLP) ou *Laser Powder Bed Fusion* (LPBF). C'est un procédé qui utilise l'énergie thermique à partir d'un laser pour faire fondre et fusionner localement des poudres thermo formables, sous atmosphère contrôlée. Ce procédé présente de nombreux atouts, mais aussi des limitations résumées dans le Tableau 1.1.

Tableau 1.1. Quelques atouts et limitations du procédé LPBF

Atouts	**Limitations**
Réduction des délais de production, Conception optimisée, Diminution des assemblages, Capacité à fabriquer des pièces très complexes, Personnalisation non coûteuse, Recyclage facile des poudres, Élimination des coûts liés à l`outillage, Réduction du temps de cycle « *buy to fly* », Diminution des stocks, etc.	État de surface (rugosité), Précision géométrique (retrait), Nouveaux procédés: connaissance de la capabilité et des performances, Les limitations dimensionnelles (étendue limitée à la taille de la chambre d'impression), Pas adapté pour la production de masse, Le choix relativement limité de poudres, Les opérations de post-traitement, Le manque de standardisation, etc.

Bien que reconnus comme étant un procédé répétitif et qui procure généralement une bonne précision dimensionnelle, la prédiction *a priori* des déviations dimensionnelles (longueur et angle) et géométriques (forme, localisation, orientation et profil) ainsi que l'état de surface du procédé LPBF est une question cruciale pour le concepteur de composants désignés à être fabriqués par cette famille de procédés. En effet, à notre connaissance, il n'existe pas encore de norme ou de standard qui abordent la capabilité du procédé.

Le présent projet s'intéresse à produire des statistiques fiables et de nouvelles connaissances en ce qui concerne le comportement dimensionnel des pièces produites par le procédé LPBF.

CHAPITRE 1

REVUE DE LA LITTÉRATURE, MÉTHODOLOGIE ET STRUCTURE DE LA THÈSE

1.1 Introduction

Ce chapitre présente une revue de littérature qui s'articule autour de deux grands axes. Le premier est les benchmarks géométriques qui ont été employés pour explorer les limites et performances du procédé. Après avoir défini les benchmarks géométriques tels que perçus par nos prédécesseurs, nous énumérons les règles de conception de ces artéfacts. S'en suit un historique des benchmarks qui ont été conçus et fabriqués de 1991 à 2019. Nous formulons les principales conclusions tirées de ces études sur la caractérisation et le comportement dimensionnel des pièces fabriquées.

Le deuxième grand axe concerne l'investigation des paramètres du procédé ayant une influence directe sur le comportement dimensionnel des pièces fabriquées, avec un accent sur les essais d'implémentation des tendances identifiées dans un modèle prédictif des déviations dimensionnelles.

Ce chapitre présente également les objectifs de recherche, les contributions anticipées, la méthodologie et enfin la structure de la thèse.

1.2 Benchmarks géométriques – Artéfacts de comparaison

Déjà en 2005, Mahesh et al. [3] identifient trois types d'artéfacts de comparaison (benchmarks) pour la FA :

1. Les artefacts géométriques permettent d'évaluer le potentiel (faisabilité et/ou capabilité) du système à fabriquer des géométries spécifiques, à analyser la répétabilité de ces géométries et de leur état de surface;
2. Les artefacts dédiés aux tests mécaniques et qui sont employés pour déterminer et évaluer les propriétés mécaniques des pièces issues de différentes poudres (comme la résistance à la rupture, la résistance à la fatigue, etc.);

3. Les testeurs de procédé permettent d'évaluer et d'optimiser le procédé comme tel (productivité, consommation d'énergie, coût de fabrication, etc.).

Dans le cadre du présent projet, nous nous intéressons spécifiquement aux benchmarks géométriques pour évaluer l'aptitude du procédé à fournir les géométries demandées avec une précision acceptable, leur niveau de répétabilité et l'impact de l'effet d'échelle (*Scalibility*), de la concentration de matière et des post-traitements sur ces géométries.

1.2.1 Règles de conception d'un benchmark géométrique

Confrontés au besoin d'avoir une évaluation quantitative de la précision dimensionnelle que peut offrir la FA, Richter et Jacobs [4] ont établi, dès 1992, une liste des qualités que doit avoir un benchmark idéal :

- Avoir des dimensions assez larges pour tester les performances de la machine à la fois aux bordures de l'espace de travail qu'au centre;
- Avoir un nombre substantiel de petits, moyens et grandes formes simples pour étudier l'effet d'échelle;
- Avoir des cavités (alésages) et des saillies (arbres) pour permettre de tester la compensation de la largeur du faisceau;
- Ne pas être trop long à construire;
- Ne pas consommer trop de matière;
- Être facile à caractériser (mesures);
- Avoir des éléments géométries qu'on retrouve sur les « vraies » pièces (parois minces, surfaces planes, trous, etc.).

À noter que, d'après nos lectures, la plupart des études sur les testeurs d'artéfacts se sont basées sur ces directives tout en les améliorant continuellement.

En 2003, Byun & Lee [5] ont ajouté que le testeur devrait avoir des éléments géométriques distincts pour chaque axe, et devrait contenir des artéfacts très petits pour déterminer la plus

petite taille imprimable par la machine. En 2005, Kruth et al. [6] ont ajouté que le testeur devrait aussi contenir des formes dont l'analyse permettrait d'ajuster et d'optimiser le procédé. Dans la même lancée, en 2012, Moylan et al. [7] donnent des orientations pour concevoir un artéfact. Ils préconisent de faire le lien entre la machine de fabrication, la fonctionnalité testée et l'artéfact, à travers des critères de démonstration de la capabilité et des limitations, des critères d'identification et de quantification des erreurs de la machine, et d'autres considérations générales comme la facilité de construction du testeur d'artéfacts et sa facilité à être caractérisé.

1.2.2 Quelques benchmarks géométriques de 1991 à 2019

Le graphique à la Figure 1.1 présente quelques uns des benchmarks géométriques apparus entre 1991 et 2019 que nous avons recensés [3, 5-53] . La totalité de notre recensement est disponible à l'ANNEXE I.

Quelques études se sont attardées à optimiser le procédé selon un protocole expérimental planifié (ex. DOE Taguchi) [54]. Ces études avaient pour but :

- L'optimisation du système de conception (sélection de valeurs des paramètres de conception, sélection d'équipements de production, de matériaux);
- L'optimisation des paramètres de production (dans le but d'améliorer la qualité des pièces);
- La détermination et analyse de la tolérance avec les paramètres précédemment optimisés.

Nous émettons plus bas quelques-unes des principales conclusions, avec un accent mis sur la technique de fusion sur lit de poudre.

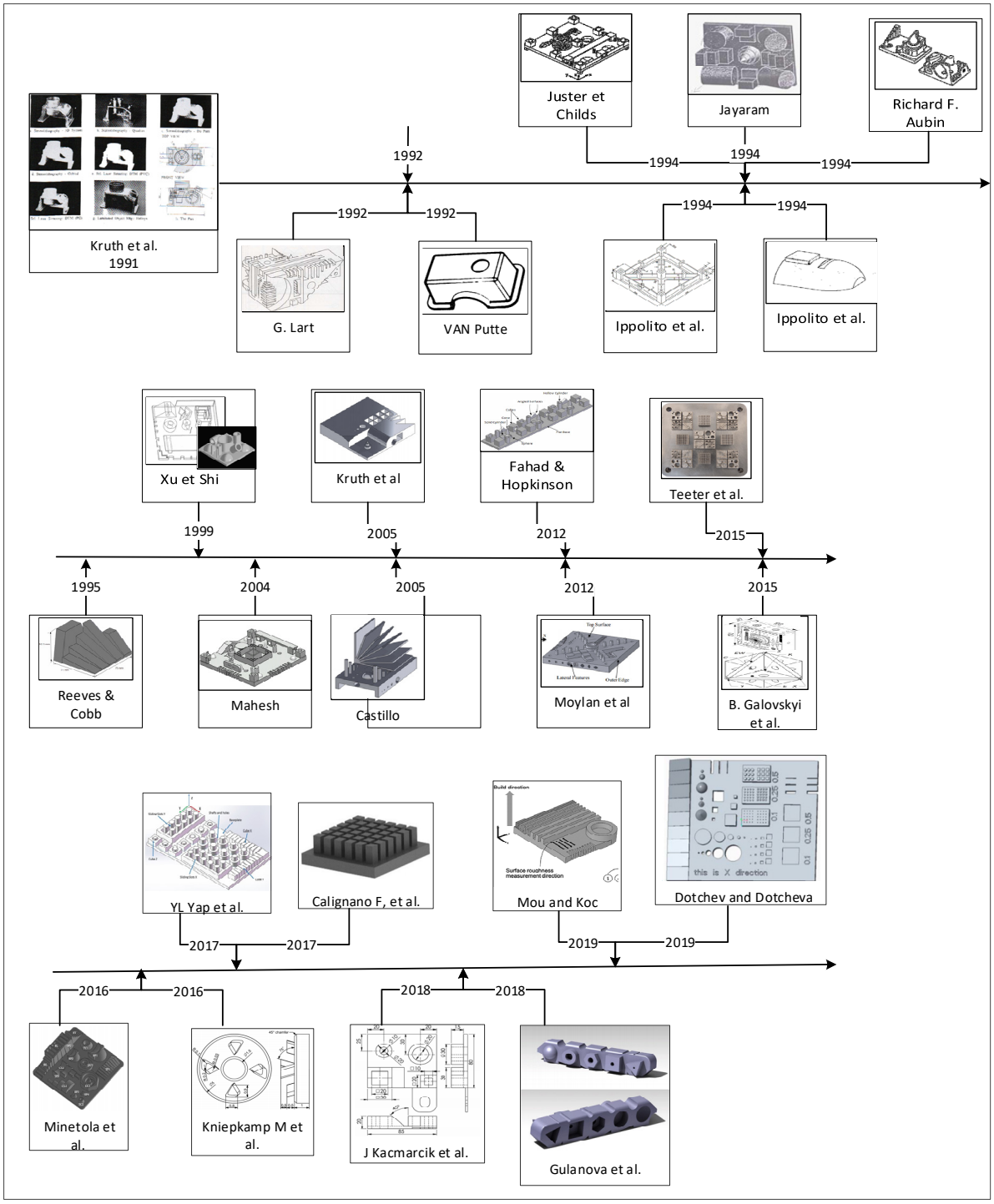

Figure 1.1 Quelques benchmarks géométriques répertoriés (1991 - 2019)

En 2007, Raghunath & Pandey [55] ont étudié le retrait en SLS, en se basant sur l'hypothèse que les retraits dans les directions X, Y et Z sont indépendants.

De l'analyse des données recueillies pendant l'optimisation des paramètres de production, il sort que les facteurs qui les influencent le plus le retrait sont :

- La puissance de laser et la longueur du balayage pour l'axe X;
- La puissance du laser et la vitesse du faisceau pour l'axe Y;
- La vitesse du faisceau, la taille du plateau et la température du lit de poudre pour l'axe Z.

Dans le but d'évaluer la capacité des procédés SLS (fusion sélective par laser) et 3DP (extrusion de matériaux) à reproduire une anatomie craniomaxillaire, Silva et al. [56] ont numérisé puis imprimé un crâne dans ces deux procédés. Ils ont observé une erreur dimensionnelle de l'ordre de 2.1% sur le crâne imprimé en SLS et de 2.7% sur celui imprimé en 3DP. De leur étude, il ressort que les modèles sont fidèles, sauf au niveau des os fins, des petits foramina (trous anatomiques), et des projections osseuses aiguës.

Dans l'intention de tester le procédé LPBF, et plus précisément la capabilité du procédé, Teeter et al.[57] ont conçu et imprimé en acier inoxydable un benchmark pour des tests métrologiques dimensionnels. Cet artéfact (Figure 1.2) est l'un des seuls dans le domaine à contenir 5 répétitions du même motif, qui ont pour but de tester les différences de fabrications dues à l'emplacement dans la chambre de fabrication.

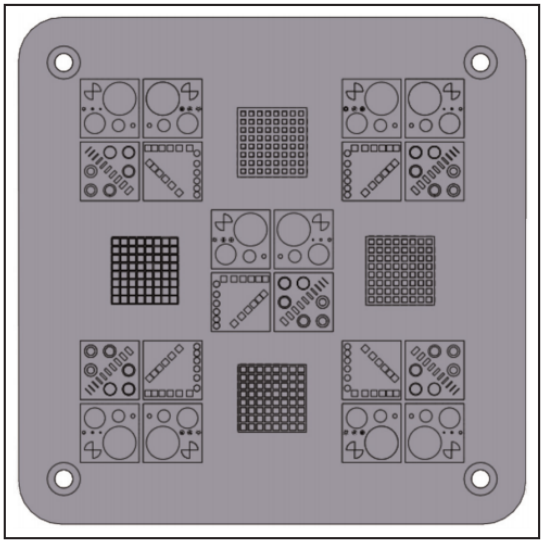

Figure 1.2 Benchmark géométrique [57]

Cet artéfact a été imprimé par fusion sur lit de poudre avec une machine de *3D Systems Corporation* avec des paramètres optimisés par le fabricant, et les mesures ont été effectuées en utilisant un microscope (*Olympus*) (précision ≈ ±0.5 μm). Les résultats obtenus démontrent qu'il n'y a pas de différence significative de fabrication (des motifs) aux 5 points de la chambre. Globalement, les performances du système se sont révélées excellentes avec quelques microns en moins sur les structures ayant une taille supérieure à 0.3 mm. En dessous de cette taille, les structures n'ont pas été imprimées pour les cylindres, et ont présenté un amas de matière pour les trous. Les structures qui n'ont pas été imprimées laissent penser qu'il y a une relation complexe dans les paramètres d'impression, puisque le diamètre de la poudre, l'épaisseur de couche (d'impression) et la taille du laser qui étaient tous à moins de 0.05 mm pendant la fabrication n'ont pas pu imprimer des structures de 0.3 mm. Cette étude permet une appréciation qualitative du procédé. En effet, elle donne une limite dimensionnelle minimale chiffrée à partir de laquelle, la machine ne peut plus fabriquer la géométrie demandée. Cette valeur (0.30 mm) est en effet la plus fréquente dans la littérature.

Cependant, l'étude ne met pas assez l'accent sur la différence de fabrication aux cinq différents points de la chambre. Sachant que la similitude dimensionnelle parfaite des structures imprimées dans les mêmes conditions est impossible, et connaissant le phénomène de la différence de température dans la chambre d'impression, nous doutons de la cohérence dimensionnelle '*parfaite*' des cinq motifs imprimés.

En étudiant les effets de la poudre (taille, distribution) et le paramétrage de la machine sur les propriétés physiques, mécaniques et chimiques d'implants osseux en titane, Basalah et al.[58] ont remarqué que la porosité et les propriétés mécaniques de la pièce finale peuvent être contrôlées à partir du paramétrage de la machine de fabrication, plus spécifiquement la taille de tête du fusionneur de poudre.

1.3 Différence entre capabilité et faisabilité

Comme mentionné précédemment, en se basant sur la norme ISO 22514, une étude de capabilité est impérativement statistique et est basée sur les caractéristiques du procédé (ex. profil 3D, orientation, rugosité, etc.). De notre étude bibliographique, nous constatons qu'une grande partie des benchmarks sont axés sur la faisabilité. Ils sont conçus dans le but de tester les limites des procédés à imprimer les formes les plus standard possible à des échelles différentes, pour quantifier la fidélité à les reproduire (Figure 1.3).

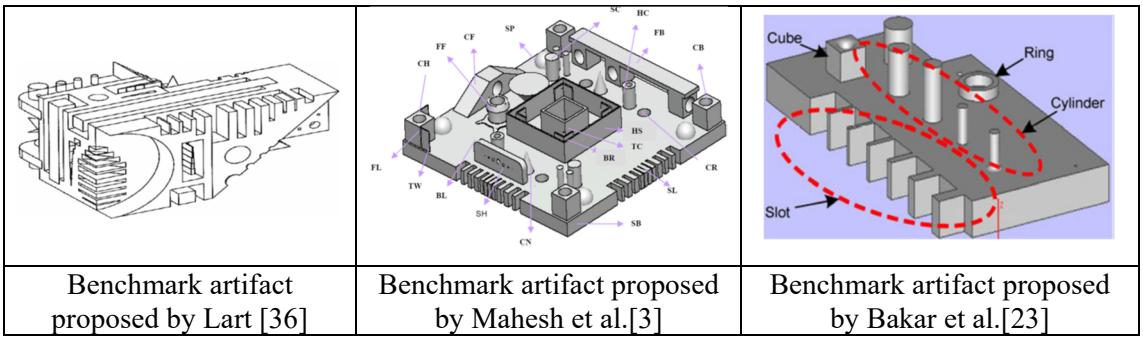

Benchmark artifact proposed by Lart [36]	Benchmark artifact proposed by Mahesh et al.[3]	Benchmark artifact proposed by Bakar et al.[23]

Figure 1.3 Benchmarks géométriques proposés

Cependant, certaines d'entre elles se rapprochent de la capabilité, en reproduisant sur le même benchmark, la même forme plusieurs fois (Figure 1.4 et Figure 1.5). Dans ces cas, la répétition permet une étude statistique, et le facteur de la position dans la chambre de fabrication doit être pris en compte pour une étude de capabilité.

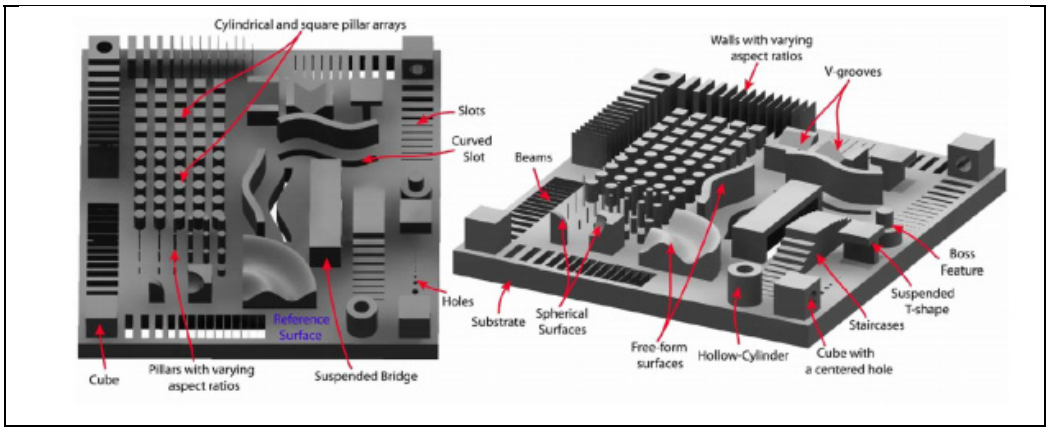

Figure 1.4 Artefact proposé par Hao et al. [59]

Par exemple, l'artéfact de Ferrar et al. [60] a été utilisé pour étudier et quantifier l'influence du débit de gaz sur la porosité de la pièce finale. Cependant, aucune étude n'a encore été réalisée pour déterminer les performances du procédé à rencontrer des tolérances géométriques telles que définies par la norme ASME Y14.5.

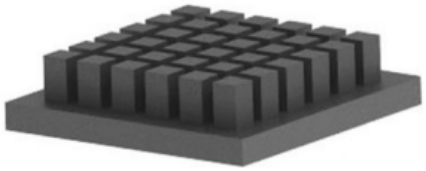	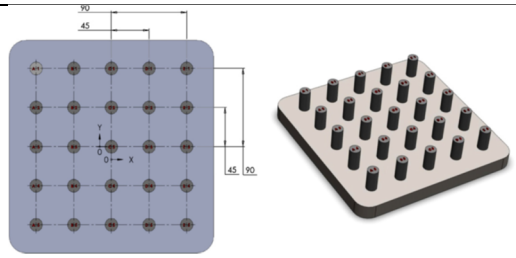
Benchmark artifact by [47]	Benchmark artifact by [60]

Figure 1.5 Benchmarks permettant une étude statistique

1.4 Essais de prédiction du comportement dimensionnel des pièces

Raghunath & Pandey [55] ont tenté de prédire le retrait dimensionnel des pièces imprimées. En se basant sur les paramètres optimisés par un DOE, ils ont analysé le retrait qui survient sur les pièces grâce à une analyse ANOVA (analyse de la variance) qui a permis d'identifier les paramètres influents et d'établir un modèle linéaire de régression. Après comparaison, les résultats obtenus expérimentalement étaient dans les intervalles prédits, mais ces intervalles prédits étaient très larges par rapport aux valeurs cibles de l'étude. Par exemple, pour un retrait expérimental de 0.267% dans la direction Y, l'intervalle de retrait prédit était de [0.084%–0.653%].

En 2012, Singh el al. [61] ont proposé un modèle pour prédire le retrait en fonction de :

- La puissance de laser;
- L'espacement des lignes de hachures;
- La température du lit de poudre;
- La longueur des hachures ;
- Le nombre de passages du laser sur une couche (scan count).

Ils ont imprimé une série de 60 échantillons en Polyamide par fusion sur lit de poudre (SLS). Ces pièces ont le même fichier CAO, mais les paramètres de fabrication étudiés (énumérés plus haut) sont différents sur chaque pièce. En se basant sur les déviations géométriques des pièces, ils ont mis en lumière la longueur des lignes de hachures comme principale caractéristique influençant les propriétés géométriques. Avec l'analyste de variance pour le retrait (ANOVA), ils ont écrit une équation de prédiction de celui-ci. L'application de cette équation sur tous les échantillons a donné une série de valeurs plus ou moins proche de la réalité (voir Figure 1.6).

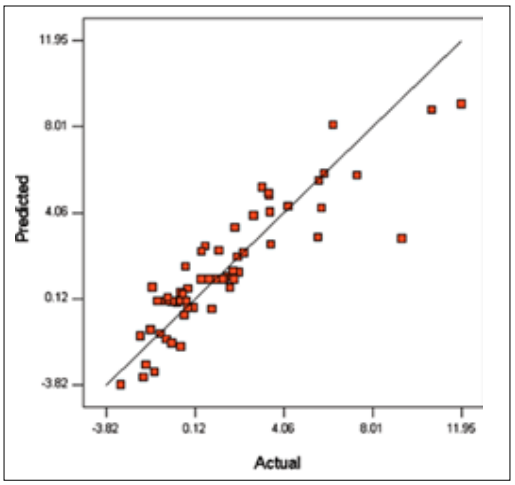

Figure 1.6 Retrait prédit vs. Observé,
Tiré de [61]

Il faut noter que la précision de ces prédictions s'affaiblit quand on est en présence d'échantillons avec un éventuel « *grand* » retrait. Nous pensons que cela pourrait être dû à la corrélation singulière de la longueur des lignes de hachures comme source d'influence primordiale sur le retrait, au détriment d'éléments tout aussi influençant comme la puissance du laser et le nombre de passages du laser (*Scan Count*).

1.5 Compensation des déviations dimensionnelles des pièces

Dans la littérature, trois stratégies sont proposées, pour améliorer la précision des pièces issues de FA :

- Adaptation du procédé, en fonction des déviations observées pendant l'impression;
- Ajustement du procédé en fonction des déviations observées sur une pièce finie;
- Modification des dimensions entrées (fichier CAO), en fonction des déviations géométriques observées sur la pièce finie.

Les études que nous allons explorer et critiquer ici sont essentiellement basées sur la troisième méthode. Pour mieux observer et prédire les déviations géométriques, on utilise les *benchmarks* géométriques (que nous avons présentés plutôt). Ces *benchmarks* sont dessinés avec des structures, sur lesquels l'erreur d'impression peut être plus facilement reliée aux entrées d'impression comme la poudre, la température de la chambre, la puissance du laser, etc.

Dans le but d'étudier, prédire et compenser l'erreur géométrique générée, Senthilkumaran et al. [62] ont développé un modèle qui prend en compte la géométrie de l'échantillon et le décalage du faisceau. Il se résume à un schéma de compensation qui intervient à chaque couche, contrairement aux autres schémas qui effectuent une compensation globale sur les pièces.

La méthode repère les points d'intersection entre les contours et les lignes de hachure et les range par nombre ascendant de coordonnés dans les directions $-x$ et $-y$. Pour chaque point elle génère des lignes de balayage, puis le décale de Δ_C (mm) qui varie selon la longueur du segment de hachure dont on traite le point de contour. Enfin, elle réécrit un nouveau contour prenant en compte cette modification (voir Figure 1.7). Un exemple de compensation sur une forme semi-circulaire est affiché à la Figure 1.8.

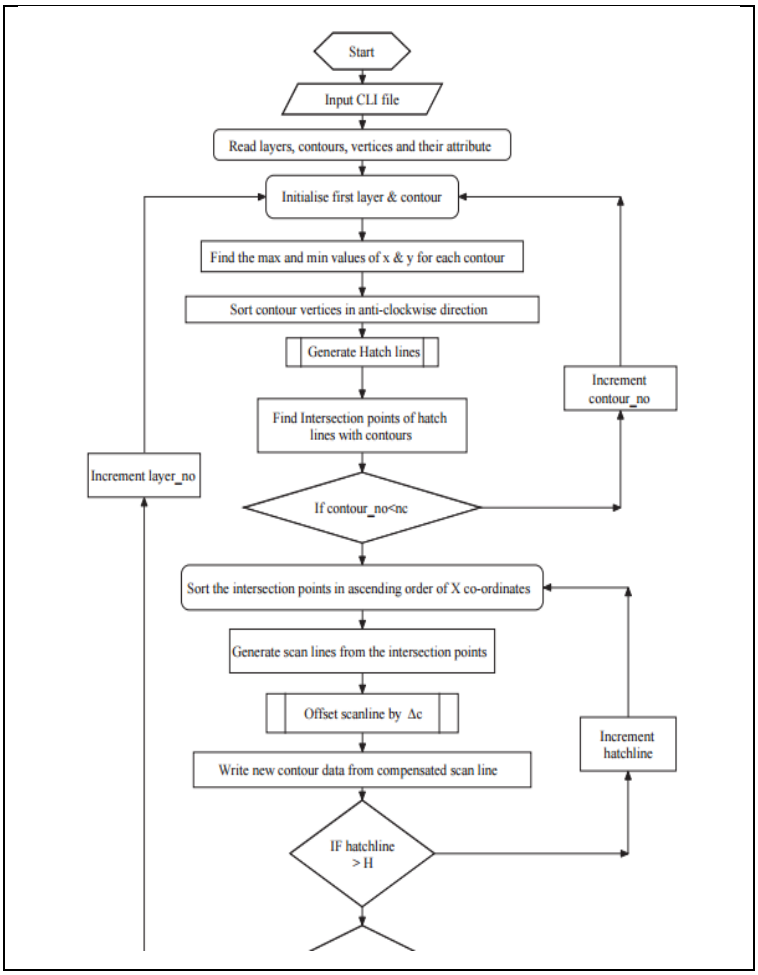

Figure 1.7 Diagramme de la procédure de compensation
Tiré de [62]

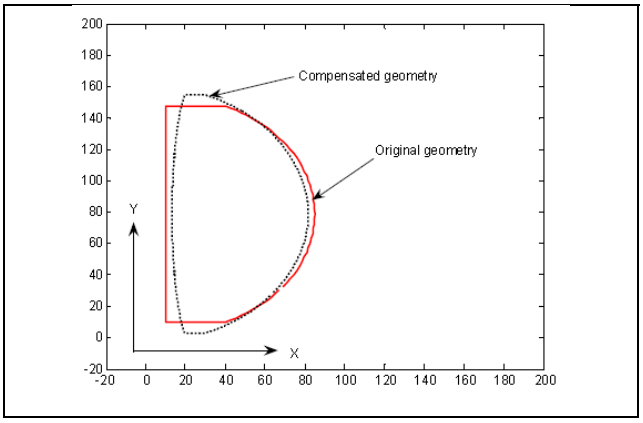

Figure 1.8 Compensation sur une forme semi-circulaire
à l'aide de la procédure proposée [62]

Dans une étude qui vise à connaitre la capabilité et à optimiser la robustesse et la contrôlabilité de l'impression des structures de Ti6AI4V poreuses par LPBF, Van Bael et al.[63] s'attaquent au problème en réduisant l'inadéquation des propriétés morphologiques et mécaniques entre la pièce dessinée et conçue, en deux séries de fabrication.

Pour fabriquer des objets poreux servant ici de *benchmarks,* 6 types d'objets poreux avec le même modèle de cellule, et des tailles de pores différentes, entre 700 et 1000 mm ont été imprimés, scannés et caractérisés sous forme d'équations, puis comparés au modèle CAO (voir Figure 1.9). Ensuite, le modèle CAO est ajusté en fonction des dérives observées précédemment (équations obtenues avec la caractérisation dimensionnelle des pièces de la première série), pour la fabrication d'une seconde série.

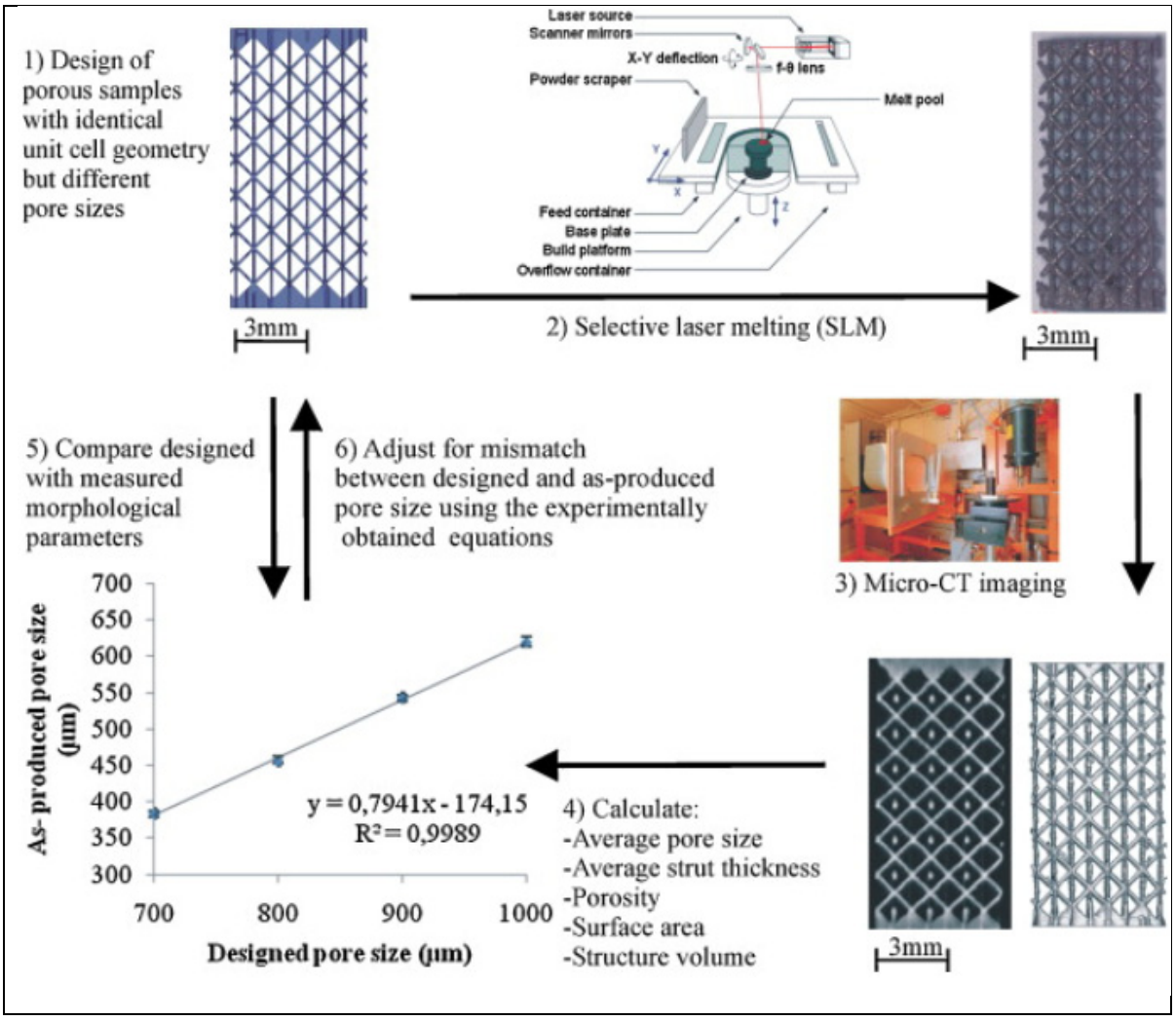

Figure 1.9 Vue schématique de la boucle de retour entre le design et la production incluant la caractérisation mécanique des pièces fabriquées [63]

En observant les défauts de la première série, on peut noter une augmentation de l'épaisseur des grilles de l'ordre de 113% en moyenne. Les raisons justificatives avancées par les auteurs sont les suivantes :

- Les vecteurs de balayage, qui décrivent les frontières de l'épaisseur des structures de liaison (du grillage), se sont décalé 40 µm vers l'intérieur pour compenser la taille du spot laser (80 µm) ;
- L'angle d'impression des structures de liaison de 45° favorise l'augmentation de l'épaisseur et de l'ondulation (à cause de l'effet escalier en AM);

- Les structures de liaison étant construites avec un angle de 45°, chaque couche est partiellement bâtie sur de la poudre libre. Avec le transport de chaleur, il y a des particules de poudre qui restent collées sur la surface.

Cette augmentation de l'épaisseur a entrainé une plus petite porosité, -18% en moyenne, une augmentation de la surface de 38% en moyenne et du volume de 180% en moyenne.
Les propriétés mécaniques sont bien en corrélation avec la densité relative ($R^2 > 0,97$), ce qui est *a priori* prometteur en termes de contrôle des propriétés mécaniques. En outre, même si nous jugeons que le nombre des différents niveaux est relativement faible (4 dans l'étude), la valeur numérique du coefficient de détermination confirme que les propriétés mécaniques (la rigidité et la résistance) sont très sensibles à la fraction du volume (1-porosité). Ils ont aussi réussi à établir des corrélations entre la taille des pores, la porosité, la surface, le volume des grilles obtenues, et la taille des pores désirée (voir Figure 1.10).

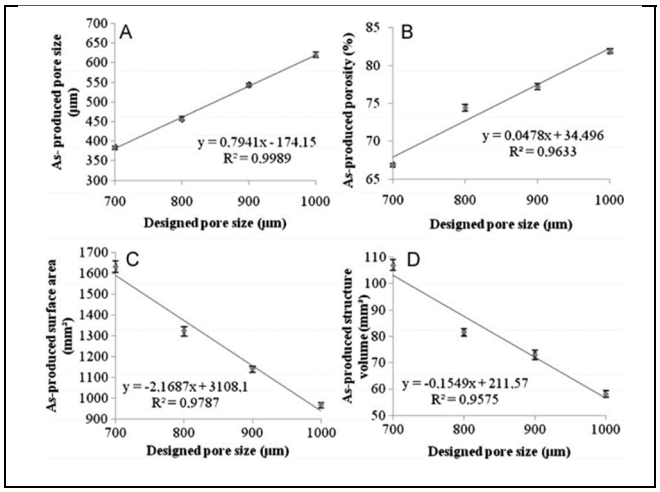

Figure 1.10 Caractérisations des échantillons imprimés en fonction du CAD [63]

Ces différentes corrélations ont été utilisées comme « outil » de prédiction pour reproduire les objets avec d'autres paramètres. Cette deuxième série avait des propriétés morphologiques et mécaniques semblables aux contraintes prévues. La différence entre la taille des pores prévue et imprimée est passée de 45% à 5% d'erreur à la deuxième série selon les auteurs. Il faut noter qu'il n'y a dans l'article, pas de données chiffrées sur la seconde série pour effectuer une

comparaison objective. Aussi, sur les figures de comparaison, l'auteur attribut à chaque caractéristique évaluée, une échelle de son choix pour mettre en lumière son coefficient directeur, plutôt que la standardisation pour permettre une appréciation globale et qualitative des données.

1.6 Étude de caractérisation de pièces en structure lattice grâce au traitement d'image

En 2016, Vanderesse et al. [64] proposent une méthode d'évaluation géométrique de structures lattices métalliques produites par LPBF. Pour ce, des échantillons sont fabriqués avec des dimensions différentes (voir Figure 1.11) puis analysés.

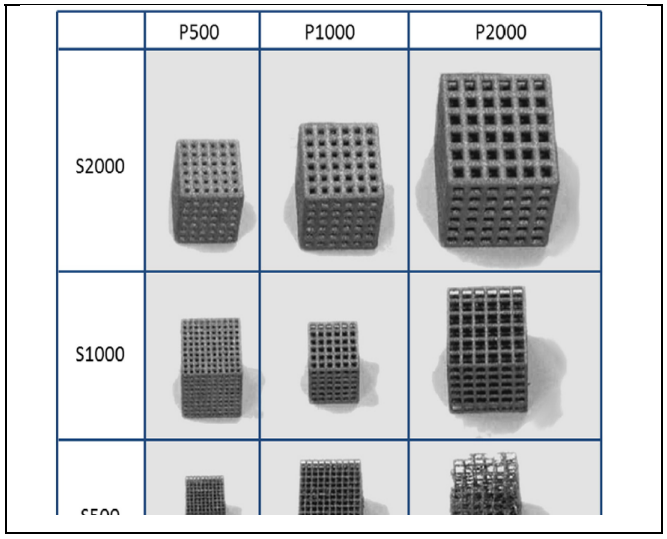

Figure 1.11 Échantillons métalliques en structure lattice,
Tiré de [64]

La méthode utilisée pour les caractériser est décrite à la Figure 1.12. C'est une combinaison bien pensée de méthodes conventionnelles de traitement d'image. L'image optique subit d'abord une carte de relief voir Figure 1.13-A. Le résultat est ensuite segmenté (image topologique seuillée + opérateurs morphologiques : ouverture et fermeture), voir Figure 1.13-B. Le résultat est soumis à une transformation de l'axe médian (squelettisation, et carte de

distances appliquées séparément, puis combinaison des résultats), voir Figure 1.13-C. S'en suit enfin l'identification des nœuds et des entretoises, voir Figure 1.13-D.

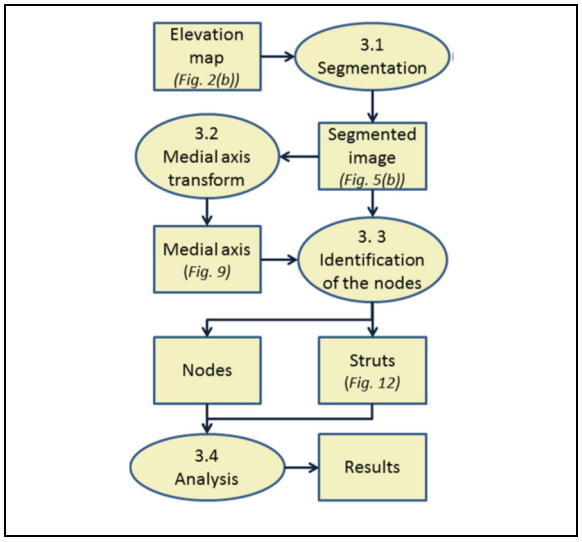

Figure 1.12 Diagramme de la méthode, [64]

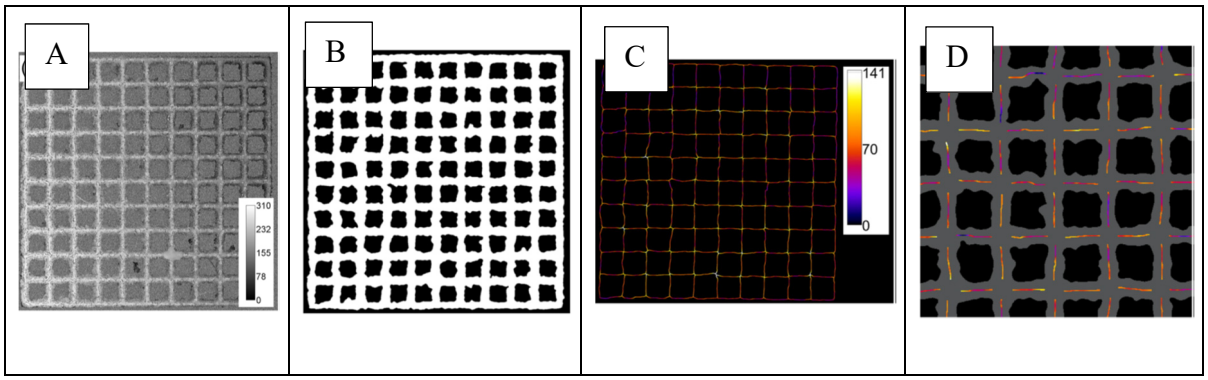

Figure 1.13 Échantillons métalliques en structure lattice, A, B, C et D Tiré de [64]

1.7 Conclusion de la Revue de littérature

De nombreuses études ont été réalisées, notamment sur les benchmarks géométriques. Cependant, peu d'entre elles se sont penchées sur l'investigation statistique (sur plusieurs pièces) du comportement des pièces imprimées. Aussi, les études ont été réalisées avec des machines d'impression différentes, et des matériaux différents. Aucune tentative de construction d'une bibliothèque conséquente de données sur les pièces fabriquées par une machine d'impression avec un matériau précis n'a été répertoriée à ce jour. Ce manque de

données limite les travaux de modélisation et de conception. La nature (systématique ou aléatoire) des déviations dimensionnelles doit être basée sur des effets observés, quantifiés et répertoriés. Cependant de nombreux essais de prédiction prometteurs ont été réalisés ces dernières années, notamment avec des modèles thermomécaniques pour investiguer sur les contraintes résiduelles [65] ou encore sur le champ de température [66].

1.8 Objectifs du projet de recherche

L'objectif à long terme est de proposer un *guide de conception* pour des composants destinés à la fabrication LPBF. Ce guide doit être basé sur une bonne connaissance des effets qui influencent le plus les déviations dimensionnelles des pièces « *as-built* » dans un premier temps, mais aussi sur les changements que subissent les pièces après chaque étape du post - traitement. Il permettra ainsi de proposer aux concepteurs des consignes réalistes reflétant fidèlement les performances de procédé.

Notre point de départ a été de se questionner. *Quel est l'intervalle probabiliste correspondant à 99,73% (équivalent à 6σ) des déviations géométriques d'une pièce imprimée? Les données d'inspection d'une forme géométrique simple (ex. cylindre, épaisseur, etc.) peuvent-elles êtes exploitées pour prédire les déviations du profil d'une pièce plus complexe? Dans une chambre d'impression, le choix de l'emplacement de la pièce influence-t-il systématiquement les défauts qu'elle aura? À quel point le procédé est-il répétable à l'intérieur de la même impression? Est-ce que cette répétabilité est constante d'une impression à une autre (avec les mêmes paramètres)?*

Ensuite, nous avons investigué l'effet d'échelle. *En émettant l'hypothèse qu'une même géométrie fabriquée à plusieurs échelles possède un comportement différent (amplitudes des déviations), Cette loi est-elle linéaire? Est-ce qu'elle est reproductible sur une autre géométrie?* Et comme corollaire à ce questionnement, *en concevant dans le même espace de travail (même échelle), des pièces ayant des répartitions de matière différentes (différentes concentrations de matière), est-ce que le niveau des déviations géométriques demeure constant? Ou alors, serait-il plus prononcé sur les pièces les plus denses?*

Finalement, quelle est l'influence dimensionnelle du traitement thermique de relaxation des contraintes (étape recommandée par les fabricants de systèmes d'impression métallique)? Quel est l'effet de ce traitement sur l'évolution des déviations géométriques des pièces imprimées? Est-ce que son effet est influencé par les dimensions (échelle) de la pièce ou de la répartition de matière sur la pièce?

Une étape obligatoire pour les pièces imprimées par le procédé LPBF est l'enlèvement (l'extraction) des pièces de la plaque d'impression. Cette opération qui est souvent réalisée

avec une lame chauffée ou une scie a un effet sur les déviations géométriques des pièces. *Cependant, son effet est-il différent en fonction de la taille de la pièce concernée? En fonction de la répartition de matière de la pièce?*

Une des limitations inhérentes au procédé LPBF est la qualité toute relative du fini de surface (rugosité) des pièces. L'opération de polissage par jet abrasif d'un mélange d'air et de sable (*Sand Blast*) ou par projection de particules est un moyen d'y remédier à cette carence. Cette opération affecte directement des données externes, uniformément si elle est réalisée en respectant le temps de soufflage, la pression appliquée et la distance avec la pièce. *Dans des conditions d'exécution idéales, quel est son impact réel sur les pièces?*

La majeure partie des déviations de la pièce finale (après la relaxation des contraintes, l'enlèvement de la plaque et le nettoyage) survient au moment de l'impression. La modification du fichier CAO (ou CAD) en prévision de ses déviations à cette étape est donc un moyen robuste de diminuer les défauts des pièces finales. Cependant, pour corriger le modèle original CAD, il faut d'abord être capable de prédire les déviations systématiques des pièces « *as-built* ». Cette dernière problématique a fait l'objet de nombreux travaux durant la dernière décennie, qui ont, pour certains, abouti à la mise sur le marché des logiciels dédiés à cette tâche, plus ou moins performants. L'un d'entre eux ANSYS Additive Print® (ANSYS, Canonsburg, PA, USA) a particulièrement attiré notre attention par les performances affichées. Nous nous sommes intéressés à la capabilité de prédiction des déviations dimensionnelles.

Découlant de ces questionnements, nos objectifs de recherche sont les suivants :

- **Objectif 1, contribution 1 :** Quantifier la répétabilité du procédé. Confirmer ou infirmer la présence d'une empreinte (motif, *pattern*) de déviations dans la chambre de fabrication grâce à une quantification précise des variations qui interviennent en fonction de la position (intra-répétabilité); quantifier la variation qui intervient entre plusieurs impressions prévues pour être identiques (inter-répétabilité). Quantifier la capabilité du procédé.
- **Objectif 2, contribution 2** : Quantifier l'effet d'échelle. Une quantification des variations géométriques qui interviennent sur la même pièce imprimée à différentes échelles;

- **Objectif 3, contribution 2** : Quantifier l'effet de la concentration de matière. Une quantification des variations géométriques qui interviennent en fonction de la densité de matière fusionnée dans le même volume de conception;
- **Objectif 4, contribution 2** : Investiguer sur l'effet des post-traitements (traitements thermiques de relaxation de contrainte, détachement de la plaque et du nettoyage surfacique) sur les pièces imprimées.
- **Objectif 5, contribution 3** : Investiguer la capabilité de prédiction des déviations dimensionnelles, de l'outil ANSYS Additive Print**;**
- **Objectif 6, contribution 4** : Proposer un outil de prédiction des déviations dimensionnelles, tenant compte des effets quantifiés.

1.9 Contributions anticipées

Ce projet va contribuer à améliorer les connaissances de la communauté scientifique sur un nouveau procédé de fabrication. Par conséquent, il permettra d'optimiser l'utilisation de ce procédé dès la phase de conception. En d'autres termes, les travaux vont nous emmener à faire un pas de plus vers le « concevoir bon et fabriquer bon du premier coup » dont les retombées économiques sont immenses. Ce projet va donc tenter de répondre à des problématiques que rencontrent les concepteurs pour la FA.

À travers une approche empirique rigoureuse, et des mesures effectuées selon le standard ASME Y14.5 [67], ce projet permettra de répondre à la question de l'effet de la position dans la chambre de fabrication. Une pratique courante dans le peu d'entreprises possédant une machine de FA, est de placer les pièces critiques au milieu, pour s'assurer d'avoir les meilleures performances de la machine sur leur fabrication. En quantifiant cet effet, ce projet permettra d'infirmer ou de confirmer l'utilité de cette pratique souvent couteuse en termes d'optimisation spatiale de la chambre, et donc couteuse d'un point de vue économique.

Ce projet va également confirmer l'importance de l'optimisation topologique, et surtout, quantifier l'effet de la répartition de la matière dans un même espace de conception pour ce qui concerne la FA.

Après la fabrication des pièces, un traitement thermique est effectué, pour relaxer les contraintes résiduelles intrinsèques au procédé. Ce projet va quantifier les effets de la relaxation des contraintes sur les pièces fabriquées par FA. Pour aller plus loin, ce projet va investiguer sur la différence de l'effet de la relaxation des contraintes (1) sur des pièces identiques fabriquées à des échelles différentes et (2) sur des pièces fabriquées dans le même espace de conception, avec différentes quantités et répartitions de matière.

Une étape incontournable du *Post-Processing* est le détachement des pièces fabriquées de la plaque. Pendant la fabrication, la plaque fait office de puits de température, et maintient la pièce à la bonne place pour la fusion des couches à venir. Le détachement des pièces induit donc des déformations sur la pièce. Ce projet va quantifier les déformations induites par la relaxation des contraintes, sur les pièces fabriquées par FA.
Le procédé n'étant pas encore parfaitement maitrisé au niveau industriel, cette étude augmentera le niveau de confiance dans le procédé LPBF au travers d'analyses métrologiques rigoureuses et participera à favoriser son intégration industrielle pour en faire un atout pour des futures applications industrielles concrètes.

Finalement, nous sommes convaincus que l'approche adoptée et qui est d'investiguer les effets de chaque facteur, avant de les implémenter dans un outil prédictif du comportement dimensionnel sera bénéfique pour notre étude. Il ne faut pas oublier que le but à long terme du projet est d'offrir un outil d'aide aux concepteurs dans une démarche d'ingénierie concurrente et de DFM (*Design for Manufacturing*).

1.10 Méthodologie proposée et structure de la thèse

Dans notre thèse, certaines hypothèses de travail sont communes à tous les jalons.

- Notre projet concernera exclusivement le procédé de fabrication additive, *Laser Powder Bed Fusion (3DP-LPBF)*.
- Aussi, la machine employée sera toujours la même : une EOSINT M280 (*Electro Optical System, Germany*) qui nous offre un espace de travail de 250×250×325 mm (Figure 1.14).

Figure 1.14 Machine de fabrication LPBF

- Nous n'inclurons pas l'effet du matériau. Les modèles seront imprimés avec l'alliage d'aluminium AlSi10Mg. Par conséquent, les conclusions ne seront applicables que sur ledit matériau. Les propriétés de l'alliage sont disponibles à la référence [68].
- À chaque impression, nous utilisons les mêmes paramètres d'impression proposés par le fabricant de la machine pour l'alliage : *AlSi10Mg_speed_103* et le même traitement thermique, soit 300°C pendant deux heures. Toute intervention sur les paramètres par défaut sera mentionnée.
- Pour les définitions qui traitent des performances et des capabilités d'un procédé à rencontrer des requis, nous utilisons la norme ISO 22514.
- Pour les déviations dimensionnelles et géométriques, nous retenons le formalisme du standard ASME Y14.5-2009.
- Pour les mesures dimensionnelles, nous procédons par étapes. Une première est celle de la captation d'un nuage de points avec un scanner laser METRIS monté sur l'AMT (CMM) Mitutoyo® au laboratoire de métrologie de l'ÉTS (précision de l'ordre de ±7.5 µm). L'étape suivante qui concerne les analyses et les traitements sur le nuage de points sera effectuée sur le logiciel Polyworks® (*Innovmetric Metrological Software*,

Québec, QC, Canada). Finalement, l'étape de l'analyse statistique sera effectuée sur le logiciel Matlab® 2017b (*MathWorks, Natick, MA, USA*) et l'analyse graphique sur le logiciel Minitab® 17 (*Minitab Inc., State College, PA, USA*).

- Pour les mesures volumiques, nous utilisons le µ-CT XT H 225 de la marque Nikon *(Nikon, Brighton, MI, USA)*, disponible à l'ÉTS. La reconstruction est effectuée avec le logiciel CT Pro 3D fourni avec l'appareil, et l'exploitation des voxels avec DragonFly *Dragonfly V2 software (Object Research Systems, Montreal, Canada)*.

Cette thèse comporte (5) chapitres, une conclusion qui résume les principales contributions et finalement, des recommandations pour des futurs travaux de recherche. Les contributions de cette thèse sont réalisées par la publication de trois (3) articles de revues (avec comité de lecture), et la participation à deux (2) conférences (Figure 1.15).

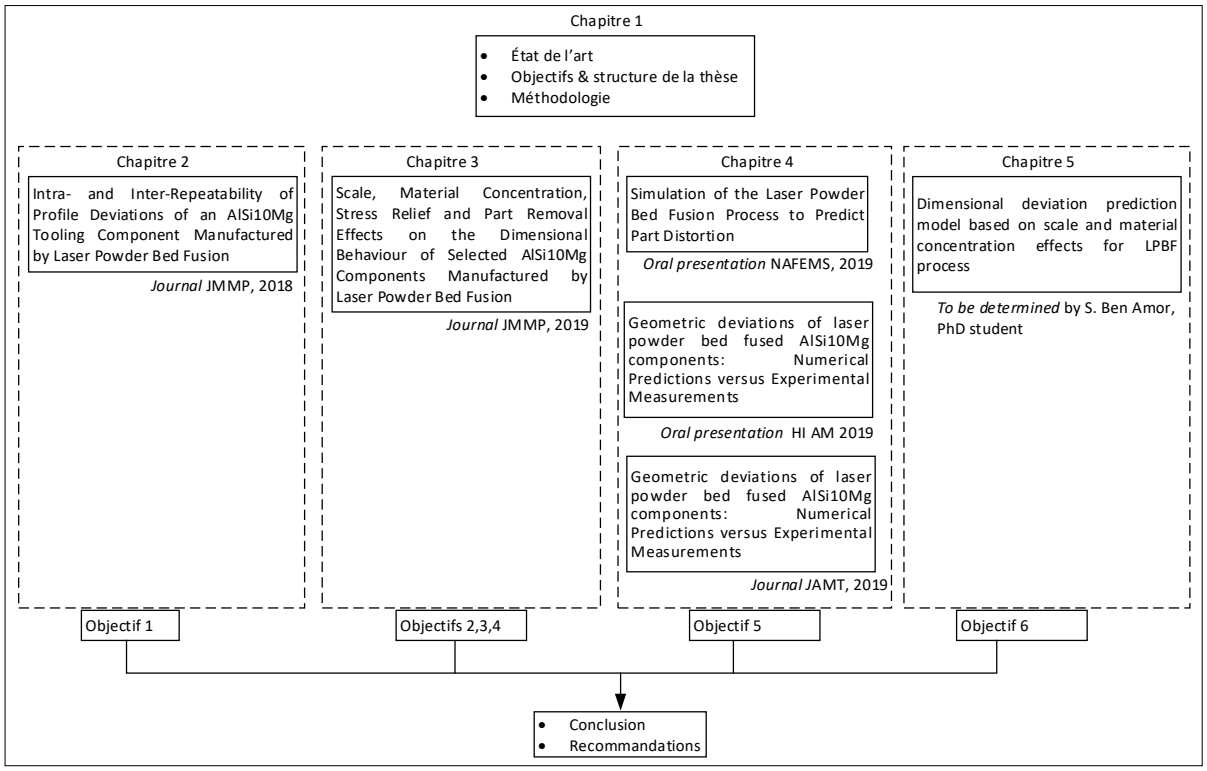

Figure 1.15 Références bibliographique des contributions scientifiques du projet

CHAPITRE 2

INTRA- AND INTER-REPEATABILITY OF PROFILE DEVIATIONS OF AN ALSI10MG TOOLING COMPONENT MANUFACTURED BY LASER POWDER BED FUSION

Floriane Zongo, Antoine Tahan *, Ali Aidibe and Vladimir Brailovski

Department of Mechanical Engineering, École de Technologie Supérieure (ÉTS), Montreal, QC H3C 1K3, Canada; teega-wende-floriane.zongo.1@etsmtl.net (F.Z.); ali.aidibe.1@etsmtl.net (A.A.); vladimir.brailovski@etsmtl.ca (V.B.)
*Correspondence: antoine.tahan@etsmtl.ca; Tel.: +1-514-396-8687

Received: 13 July 2018; Accepted: 15 August 2018; Published: date 21 August 2018

Abstract: Laser powder bed fusion (LPBF) is one of the most potent additive manufacturing (AM) processes. Metallic LPBF is gaining popularity, but one of the obstacles facing its larger industrial use is the limited knowledge of its dimensional and geometrical performances. This paper presents a metrological investigation of the geometrical and dimensional deviations of a selected LPBF-manufactured component, according to the ASME Y14.5-2009 standard. This approach allows for an estimation of both the process capability, as per ISO 22514-4 standard, and the correlations between the part location in the manufacturing chamber and the profile deviations. Forty-nine parts, which are representative of a typical aerospace tooling component (30 mm in diameter and 27.2 mm in height) were manufactured from AlSi10Mg powder using an EOSINT M280 printer and subjected to a stress relief annealing at 300 °C for two hours. This manufacturing procedure was repeated three times. A complete statistical analysis was carried out and the results of the investigation show that LPBF performances for all geometrical variations of 147 identical parts fall within a range of 230 μm at a 99.73% level.

Keywords: additive manufacturing; laser powder bed fusion; selective laser melting; metrology; inter-repeatability; intra-repeatability; geometrical dimensioning and tolerancing (GD and T); process capability.

2.1 Introduction

Additive manufacturing (AM) technologies produce 3D engineered parts from nominal CAD files in an additive manner, generally layer by layer. The term “additive” is used to highlight the fact that these technologies do not require conventional tooling to build components and that the shape is created by adding, rather than removing or deforming, material. The material can be polymer, metal, composite, ceramic, concrete, or even human cells. Many AM processes have been developed and are commercially available, including stereolithography (SL), fused deposition modeling (FDM), three-dimensional printing (3DP), powder bed fusion (PBF), direct metal deposition (DED), and sheet lamination (SL). The PBF technologies include two variants depending on the nature of the heat source: the electron beam powder bed fusion (EBPBF) and the laser powder bed fusion (LPBF). Their general principles are described on ISO/ASTM52901-16 [1].The processes terminologies used are from ISO/ASTM 52900:2017 [2]standard terminology for AM.

Wohler’s report stated that 13,058 AM machines were sold in 2016 [69]. The use of these processes is expanding and can be explained by the benefits they provide: free complexity and easy customization, as well as the reduced setup time, delivery time, and tooling cost. LPBF is one of the most potent metallic AM technologies. However, the laser power, temperature field heterogeneity, and other phenomena inherent to the process generate residual stresses responsible for distortions of the produced parts [70]. Geometrical and dimensional deviations (GD and T) in LPBF parts are among the main concerns as far as it concerns facing wider industrial applications of this technology. There is a need to study the process and improve part precision, which has been criticized by many researchers.

Wang et al. [71] studied the correlations between shrinkage, laser beam offset, and the weight of LPBF parts. After statistical analysis, sampling theory and three calculation methods, the conclusion was that the shrinkage remains nearly unchanged irrespective of the weight of AM parts. However, the beam offset increases with part weight. One of the first shrinkage calibrators for metallic AM was also proposed. Zhu et al. [72] studied the shrinkage of direct laser sintered metallic powder parts. Two types of shrinkage, thermal and sintering shrinkage, were isolated and quantified. Thermal shrinkage results from cyclic heating, while sintering

shrinkage is caused by densification and is a type of elastic compressive shortening. The conclusion was that the higher the laser power and the smaller the scan speed and spacing, the higher the thermal shrinkage. Additionally, the total shrinkage in the Z plane is significantly higher than in the X-Y planes.

Raghunath and Pandey [55] identified the sources of deviation for each build axis using the Analysis of Variance (ANOVA) technique. Laser power and scan length were identified as the primary sources of deviations in the X-axis, laser power and beam speed in the Y-axis, and part bed temperature, hatch spacing and beam speed in the Z-axis. Islam and Shacks [44] investigated the influence of build parameters on the dimensional errors of 60 selective laser sintered polyamide parts. Senthilkumaran et al. [62] developed a model for shrinkage compensation in LPBF which operates in each layer. Galovskyi et al. [73] tested some work pieces for LPBF.

Detailed investigations of AM part geometrical deviations have been carried out in [7, 11, 12, 15, 16, 25, 35, 36, 46, 63, 64, 74, 75]. Fahad and Hopkinson [27] proposed a benchmark to evaluate and compare the accuracy and repeatability of the AM processes. This benchmark has three repetitions of features with standard geometries. With the intention of testing the LPBF process, Teeter et al. [57] conducted a metrological study about deviations appearing according to part location in the manufacturing chamber. After printing five pattern repetitions on a plate (the inspection was performed using an Olympus microscope with a resolution of ±0.5 μm), there was no difference between the pattern profile deviations. Ferrar et al. [60] investigated the gas flow effect on SLS repeatability and performance. In their study, variations in gas flows have been shown to affect both the value, the density and the compression strength range of the samples tested. Aidibe et al. [76] investigated the repeatability of the LPBF technology with five Ti-6Al-4V parts. The conclusion was that the LPBF process can provide acceptable metrological performances in terms of repeatability, overall deviations and geometric/dimensional errors, comparable to turning. Rebaioli and Fassi [77] identified some benchmark artefacts designed to evaluate the geometrical performance of the AM processes and their design guidelines. Sing et al. [78] investigated the effect of LPBF processing parameters on the dimensional accuracy and mechanical properties of cellular lattice structure using a statistical modeling. The conclusion was that the strut dimensions of LPBF fabricated

lattice structures are most sensitive to laser power, as compared to layer thickness and scanning speed. Calignano [79] investigated the accuracy and surface roughness of parts manufactured by LPBF in the AlSi10Mg powder. The conclusion was that the STL file, build orientation, and process parameters affects the accuracy.

Globally, researchers have focused more on feasibility rather than on capability studies, the former revealing process limitations in printing some specific geometric features, while the latter provides an estimation of the probabilistic behavior of some metrological characteristics of the part produced by this process. Since the latter aspect represents a main goal of this study, this paper quantifies the LPBF process intra and inter repeatability, and capability with AlSi10Mg powders. The paper is organized as follows: Section 2 describes the experimental procedure. The results are presented in Section 3 and discussed in Section 4. Finally, a summary is provided and future works are presented in Section 5.

2.2 Experimental Protocol

The first goal of the experimental procedure is to identify and quantify the variations in the geometrical deviations of a selected part as a function of its location in the LPBF manufacturing chamber. Then, this experiment is intended to provide an answer to the hypothesis of a repeatable pattern of such deviations.

To this end, 49 identical AlSi10Mg parts equally distributed on a build plate (Figure 2.1) were printed three (3) times in the same LPBF system using the same process and post-process parameters, and analyzed by the same operator using the same equipment. The printed part is a typical aerospace tooling component, 30 mm in diameter and 27.2 mm in height. This part was chosen because it is an industrial tooling component used in jig construction, it is a kind of case study for industries interested in manufacturing by LPBF. Secondly, it is a topologically-optimized part. Finally, this part allows us to have an adequate sample size (49 parts/plate) for our study. Since we are concerned by GD and T variations as a function of part location in the fabrication chamber, an interesting element of this study is the number of repetitions which is 49 times three (49×3). This means that information from 49 different emplacements on the plate quantifies the variations occurring at the same place three times.

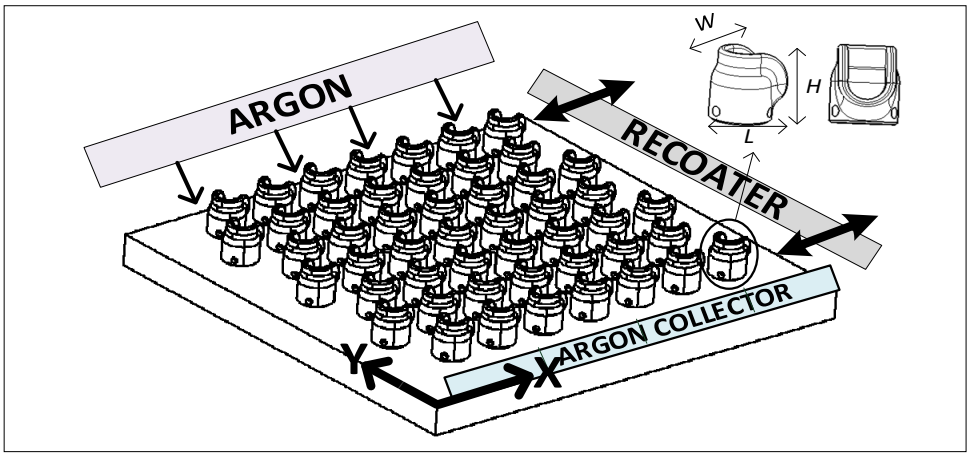

Figure 2.1 Parts disposition in the chamber for each build (EOS M 280).

In most cases, to reduce the risk of distortions caused by thermal gradients, while firmly attaching the part to the build plate during printing, the part needs to be built with support structures. In this study, specialized software Magics v.17.02 (Materialise, Leuven, Belgium) was used to generate support structures. The assembly was then loaded in the process software (PSW.3.4), where it was duplicated 49 times. The process parameters set, called *AlSi10Mg_speed_103* and recommended by the manufacturer EOS (Krailling, Germany) for an AlSi10Mg alloy, was used, with 30 µm-thick layers (Figure 2.2-a). After printing, the build plate was stress relieved at 300 °C for two hours with no visible effect on the outer surface of the parts (Figure 2.2-b).

Next, the point cloud of printed parts was obtained by means of a Metris LC50 laser scan mounted on a Mitutoyo Coordinate Measuring Machine (CMM) (accuracy ≤7 µm at the 95% level), Figure 2.2-c. Before each scan, the devices were calibrated using a master sphere and the data collection was performed on nine (9) angles to maximize the information collection on inner surfaces. A real-time visualization was possible with the Focus Inspector specialized software. A thin layer of talcum powder was used to reduce part surface reflection. In doing so, the potential point cloud density was increased to ensure the best measurement. The point clouds was then assembled (from the nine angles) and cleaned. The parts were scanned before and after being cut off the plate. The best-fit technique was then carried out using PolyWorks® v.16 (Innovmetric Metrological Software, Quebec, QC, Canada). The data were then loaded into a Matlab® 2017b (software of MathWorks, Natick, MA, USA), using a code to extract the

deviation at each point. Minitab® v.17 (a statistical software of Minitab Inc., State College, PA, USA) was used for the graphics and statistical studies (Figure 2.2-d).

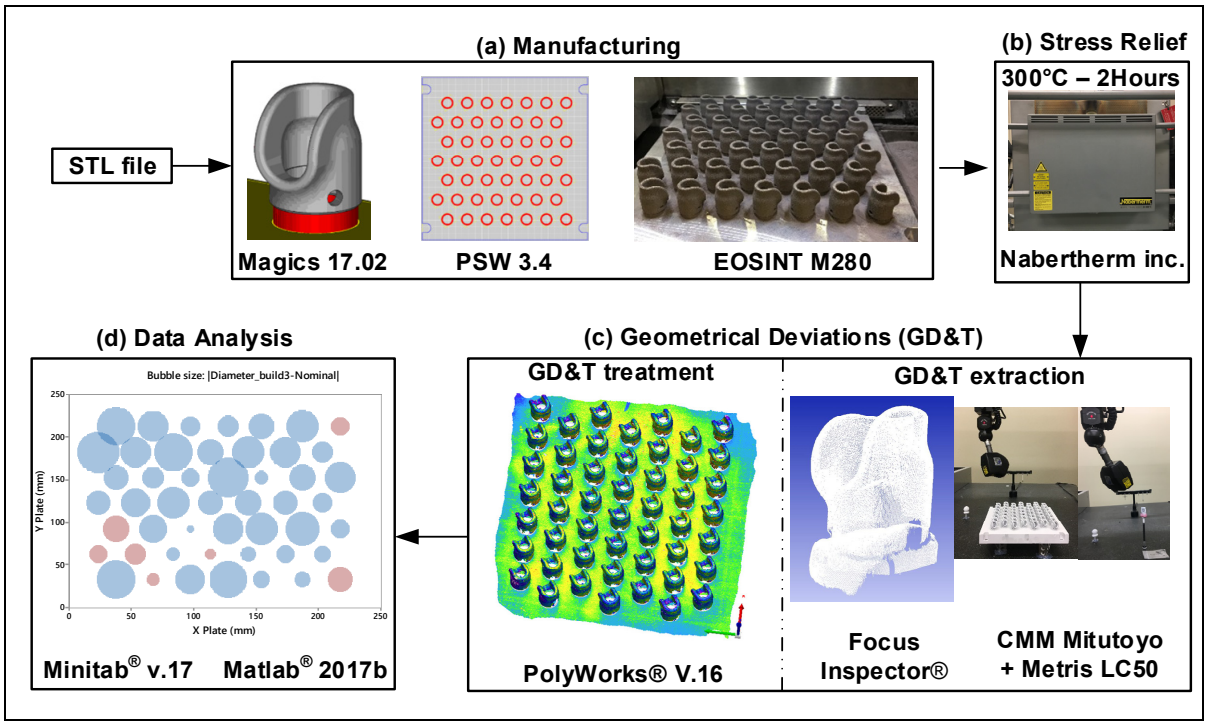

Figure 2.2 Experimental protocol: (**a**) manufacturing sequence, (**b**) stress relief heat treatment, (**c**) geometrical deviation measurements, and (**d**) data analysis.

Four types of analysis were performed based on ASME Y14.5 (2009): Intra-build variation study (Analysis 1), inter-build variation study (Analysis 2), and a capability study according to ISO 22514-4 (Analysis 3).

2.2.1 Intra-Build Variations Study

The intra-build variation study (Analysis 1) consisted of measuring the profile deviations (without a frame of reference) between the digitized parts (SCAN) and the nominal part (CAD). The digitization provided an average of 400,000 points for each part. The overall 3D profile deviations were extracted using the IMInspect module of PolyWorks® v.16 for each part, and represented by their nonparametric medians. In the first part of this intra-build variation study (Analysis 1a), visualizing the repartition of the profile deviations in the

manufacturing chamber was the main interest. The second object of interest was the deviations of the external diameter of the parts at a height of z = 1.2 mm (Analysis 1b). This plan z = 1.2 mm has been chosen because it is the mid-value between the chamfer and the holes in the cylindrical feature of the part. For each of the 147 parts, the absolute difference between the measured diameter (using best fit criteria) and the nominal diameter (Ø19.05 mm) was extracted using the IMInspect module of PolyWorks® v.16 and plotted using Minitab® v.17. The Analysis 1c consisted of a correlation study of the two previous variables, the overall 3D profile deviation and the external diameter at a height of z = 1.2 mm. This analysis was carried out using a regression equation, which is an algebraic representation of the regression line used to describe the relationship between the response and predictor variables. In our case, the measured diameter was used as a predictor variable, while the overall 3D profile deviation represented by its median was considered as a response variable. Minitab v.17 linear regression analysis was used to obtain the equations for the three builds. Finally, a basic statistical study was also conducted with the overall 3D profile deviations and the external diameter at a height of z = 1.2 mm (Analysis 1d).

2.2.2 Inter-Build Variations Study

In order to quantify the inter-build variations (Analysis 2), which is the variation behavior among three builds, two statistical analyses were performed: the Kolmogorov–Smirnov (KS) test (Analysis 2a) and the inter-repeatability quantification (Analysis 2b). A visual comparison was also carried out using the best-fit technique with PolyWorks® v.16. The KS test and visual comparison were performed using the data acquired before cutting the parts off the plate for Build #2 and Build #3 (Build #1 data before cutting the parts were not available). The KS test is a nonparametric goodness-of-fit test that compares cumulative distribution functions (CDF). It is explained below in equations (2.1 and 2.2). In this case, the KS test was used to compare the CDF of the 3D profile deviation of Build #2 and Build #3 acquired before the part removal. Given n data points $x_1, x_2, \ldots, x_n$ of the build #j, the empirical CDF is defined as:

$$F_{j,n_j}(t) = \frac{1}{n_j}\sum_{i=1}^{n_j} 1_{x_i \le t} \tag{2.1}$$

where 1_{x_i} is the indicator of event x_i, n_j is the data size from build #j, and $F_{j,n_j}(t)$ is its corresponding empirical CDF. The KS test between Build #2 and Build #3 is based on the maximum distance between two curves:

$$KS_{n_2,n_3} = \sup_t \left| F_{2,n_2}(t) - F_{3,n_3}(t) \right| \tag{2.2}$$

The null hypothesis H_0 is F_{2,n_2} and F_{3,n_3} have identical CDF behavior. H_0 is rejected at a significance level $1-\alpha$ if:

$$KS_{n_2,n_3} > c(1-\alpha)\sqrt{(n_2+n_3)/n_2 n_3} \tag{2.3}$$

where $c(1-\alpha)$ is the inverse of the KS distribution at level $1-\alpha$. The *p*-value is used as criteria for acceptance/rejection of the KS test [80]. α is the type I error [31]. The significance level is this study is 95%. This significance level was chosen because he usually used in metrological analyses. If the *p*-value is lower than the significance level $\alpha = 0.05$, then the null hypothesis H_0 is rejected.

Analysis 2b is an inter-repeatability statistical study carried out using CDF of the 3D profile deviation of each part as shown in equations (2.4) to (2.6). Nine (9) different locations were selected (to be specified below) to uniformly cover the build space. The inter-variation study was performed for each position at a 95% level:

$$PV = \pm 1.96\sigma_{PV} \tag{2.4}$$

$$\sigma_{PV} = K_3 R \tag{2.5}$$

$$R = max(x_i) - \min(x_i) \tag{2.6}$$

With x_i is the capabilities as described in equation (2.7) of the profile deviation at location i for Build #j (1, 2, and 3), R is the range of the three parts, σ_{PV} is the standard deviation, and PV is the part variation. For this case, $K_3 = 0.5231$ [76].

2.2.3 Capability Study

According to the ISO 22514-4, the process capability is a statistical estimate of the outcome of a characteristic of a process which has been demonstrated to be in a state of statistical control (stable) and which describes the process ability to fulfill the requirements of a given characteristic. By definition, process capability is the interval between L_1 = 0.135% and L_2 = 99.865% of the individual values' distributions; in other words, the interval containing 99.73% of the data (Figure 2.3).

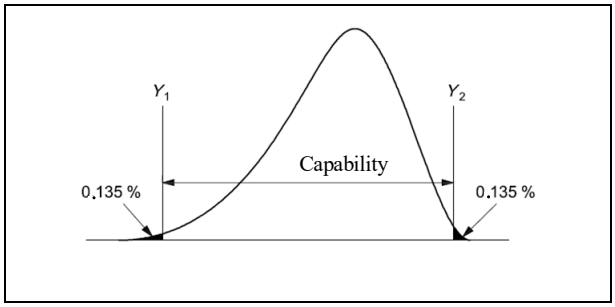

Figure 2.3 Capability interval in conformity with ISO 22514-4.

The capability study (Analysis 3) was performed using the non-parametric quantiles $L_{x\%}$ of the parts' profile deviations (Analysis 3a). The capability was obtained by:

$$\text{Capability} = L_{99.865\%} - L_{0.135\%} \tag{2.7}$$

Monte Carlo Simulation (MCS) [81] of the 3D profile deviation behavior was also carried out using Matlab® 2017b. For each part, the overall deviations were fitted to a normal distribution at a 95% confidence level. The MCS was then performed on the 147 normal distribution parameters, and the overall capability was extracted (Analysis 3b).

2.3 Results

The GD and T analysis was based on ASME Y14.5 (2009) and provides the following information: (1) Nonparametric intra-build variations study; (2) inter-build variations study, including goodness-to-fit test and; (3) capability study according to ISO 22514-4.

2.3.1 Intra-Build Variations

In the first study, each build is analyzed independently. This intra-build variation values are related to the location of each of the 49 parts uniformly distributed on the build plate and covering it entirely. In Analysis 1a, different colors are allocated to the deviation map shown in Figure 2.4 to represent the amplitude of the profile deviations (normal vector to the nominal surface).

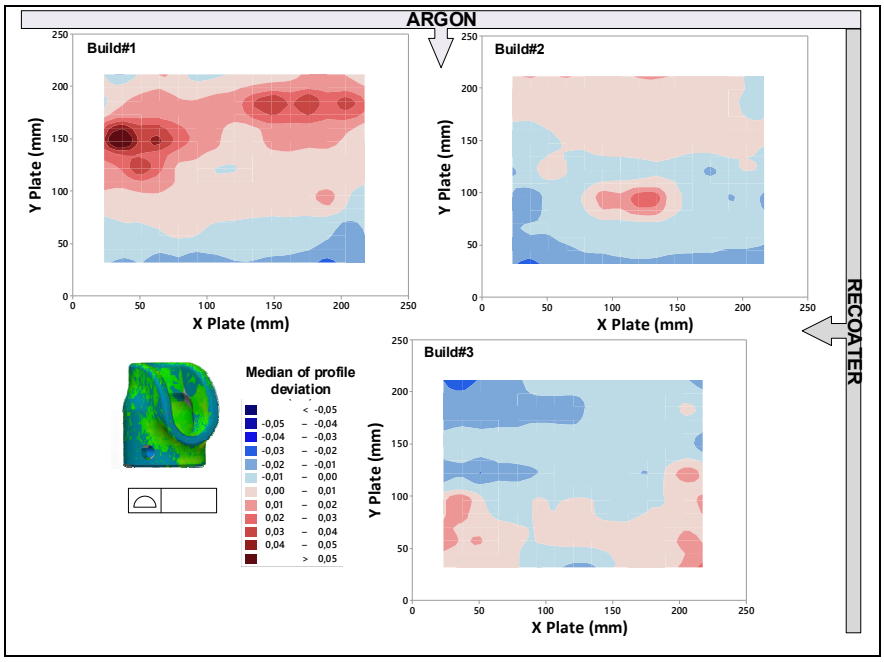

Figure 2.4 Contour plot of the profile deviation distribution using the median deviation of each part for all three builds.

The results of Analysis 1b are presented in Figure 2.5. Colors are brought about to distinguish the material withdrawal, when the feature is smaller than the nominal size in the least material

condition (LMC) direction from the addition which is an increase from the nominal size in the maximum material condition (MMC) direction as in ASME Y14. 5.1 [33]. Black bubbles are placed where this difference was less than 1µm.

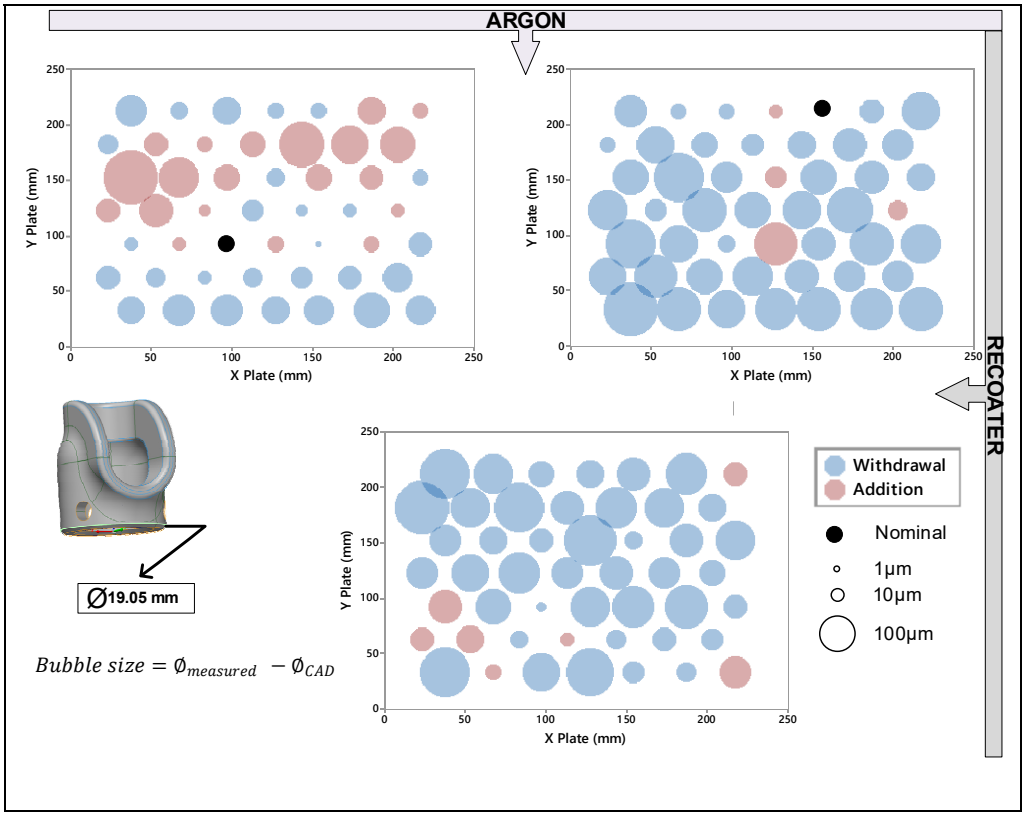

Figure 2.5 Bubble plot of the diameter deviation of each part of the three builds; the size of the bubble illustrates the absolute difference between the measured diameter and the nominal size of the part.

The results of Analysis 1c correlating the measured diameter (predictor) and the median profile deviations (response) are plotted in Figure 2.5. In Figure 2.6, the value of S is measured in units of the response variable and represents the standard distance data values from the regression line. For a given study, the better the equation predicts the response, the lower the S value. R-Sq represents the proportion of variation in the observed response values that is explained by the predictor variable, which is the measured diameter. Adjusted R-Sq(adj) is a modified R that has been adjusted for the number of terms in the model.

A basic statistical study was also conducted to evaluate the intra-build variation (Analysis 1d). The first objective of this analysis was the external diameter at a height of z = 1.2 mm extraction and characterization. The results are presented in Tableau 2.1. The second objective is the overall 3D profile deviations of each part, represented by the gap between the non-parametric quantiles $L_{1\%}$ and $L_{99\%}$ (Tableau 2.1) (with μ = mean; $StDev$ = Standard deviation)

Tableau 2.1 Descriptive statistics of the measured diameter for 49 parts (dimensions in mm).

Build	$\boldsymbol{\mu_{\emptyset}}$	$\boldsymbol{StDev_{\emptyset}}$	$\boldsymbol{Min_{\emptyset}}$	$\boldsymbol{Median_{\emptyset}}$	$\boldsymbol{Max_{\emptyset}}$
#1	19.053	0.054	18.970	19.041	19.243
#2	19.017	0.025	18.964	19.015	19.108
#3	19.012	0.038	18.936	19.011	19.095

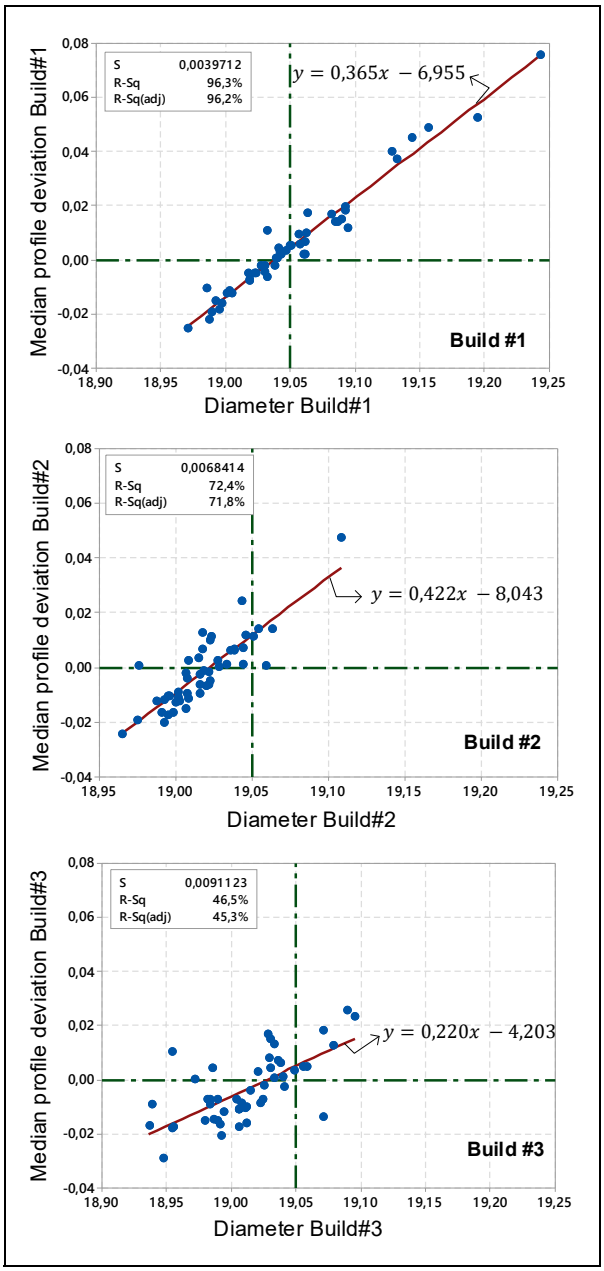

Figure 2.6 Correlation between the diameter deviation (predicton) and the profile deviation (response).

Tableau 2.2 Descriptive statistics of the measured Profile $\cap$ $(L_{99\%} - L_{1\%})$ for 49 parts (dimensions in mm).

Build	$\mu_{\cap}$	$StDev_{\cap}$	$Min_{\cap}$	$Median_{\cap}$	$Max_{\cap}$
#1	0.148	0.058	0.108	0.131	0.501
#2	0.152	0.023	0.124	0.149	0.276
#3	0.147	0.014	0.116	0.148	0.181

2.3.2 Inter-Build Variations

This study involves comparing the builds and quantifying and analyzing the differences. First of all, a visual comparison is carried out. For example, Figure 2.7 presents the overall 3D-profile deviations for Build #2 and Build #3, where the same color scale and parameters are used. This comparison reveals more material withdrawal in Build #3 than in Build #2 (more detailed discussion will be made in Section 4). Next, Figure 2.8 illustrates the results of Analysis 2a (KS test). Since the *p*-value is higher than 0.05 (α), no significant statistical differences between the CDFs of Build #2 and Build #3 can be reported (95% confidence level). The range of the inter-repeatability (Analysis 2b) for the 49 locations is 455 µm. The minimum part variation is 14 µm, and the maximum is 469 µm at a 95% confidence level, as will be shown in more detail in the next section.

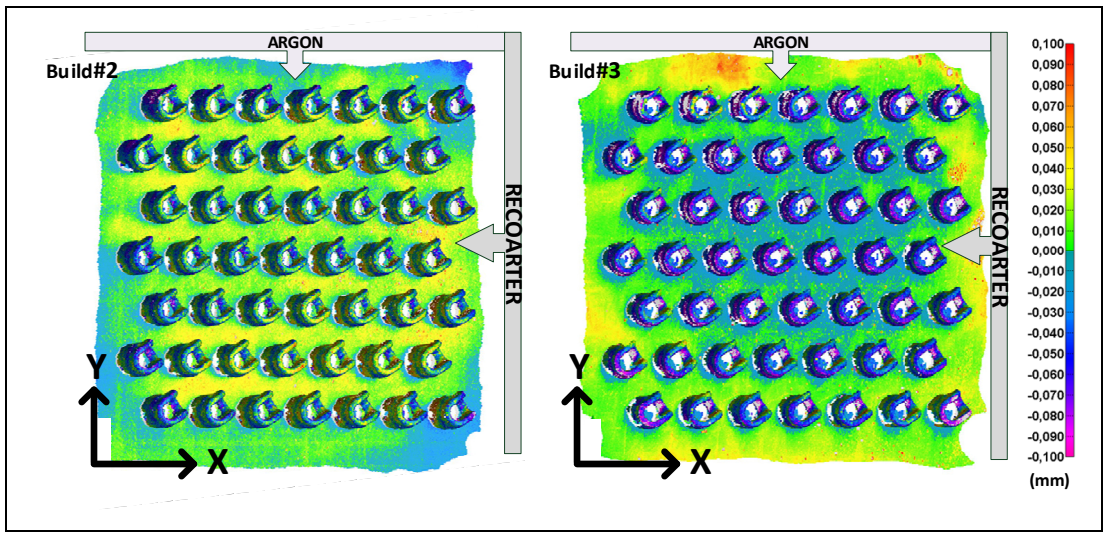

Figure 2.7 Overall 3D profile color deviation map for Build #2 and Build #3.

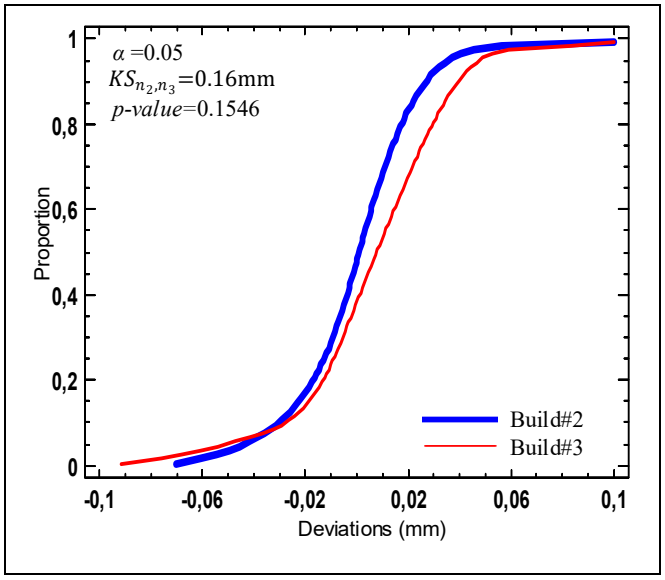

Figure 2.8 KS-test results for Build #2 and Build #3.

2.3.3 Capability

The capability study (Analysis 3) was performed on all 174 parts, and the results of this study are presented in Figure 2.9. Figure 2.9-a illustrates the external diameter extraction and quantification, Figure 2.9-b presents its non-parametric distribution Figure 2.9-c the distribution of the profile deviation of one part, with the capability interval highlighted, and Figure 2.9-d shows the distribution of the capability intervals of 49 parts.

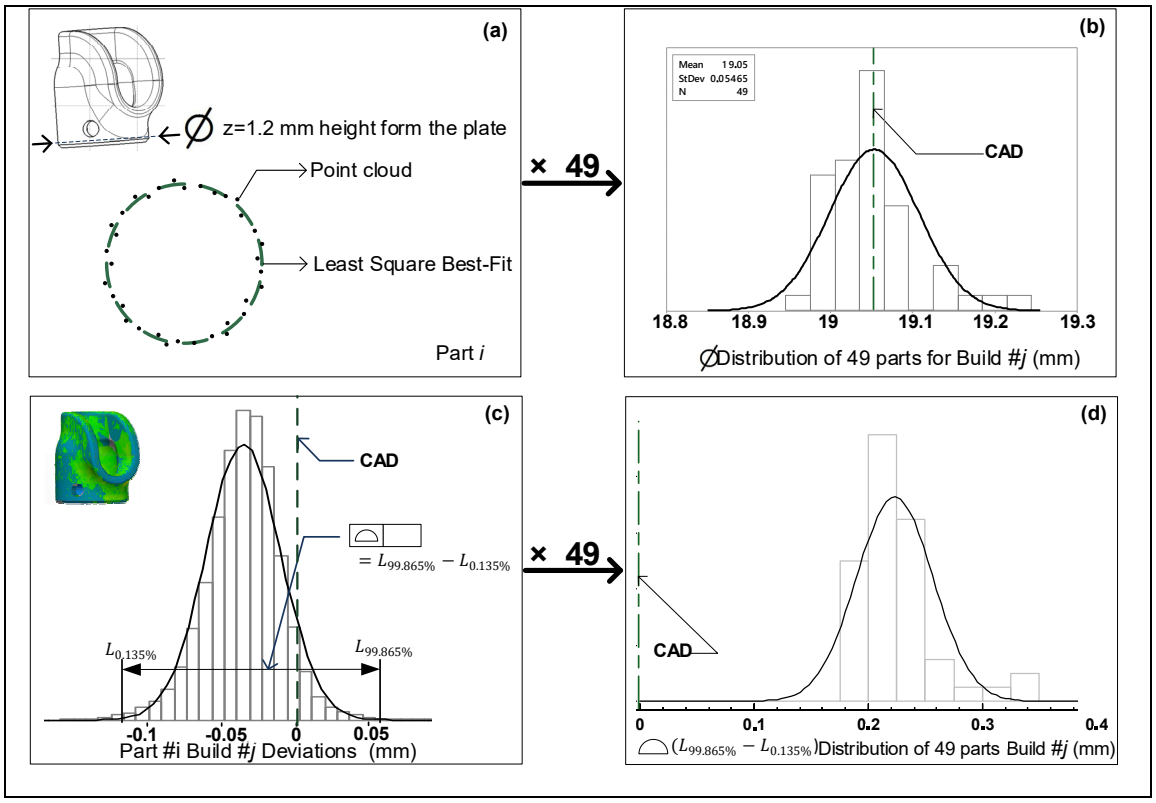

Figure 2.9 Capability and diameter deviation analyses: (**a**) Diameter quantification, (**b**) 49 parts' (one build) diameter distribution, (**c**) 3D profile deviation capability, and (**d**) 49 parts' (one build) 3D profile deviation capabilities distribution.

The results of Analysis 3a are presented in Figure 2.10, giving an overview of the capabilities (as in equation 2.7) over three builds for nine locations selected to uniformly cover the build space. Thus, for each of the selected part location, the capability (99.73%) and the 95% ($L_{97.5\%} - L_{2.5\%}$) intervals of profile deviations are provided for Build #1, Build #2, and Build #3. Tableau 2.3 presents the results of Analysis 3b for Builds #1, 2, 3 and for the overall 147 parts. It also reveals that the 3D profile deviation capability interval for the 147 parts falls within 228 µm at the 99.73% level.

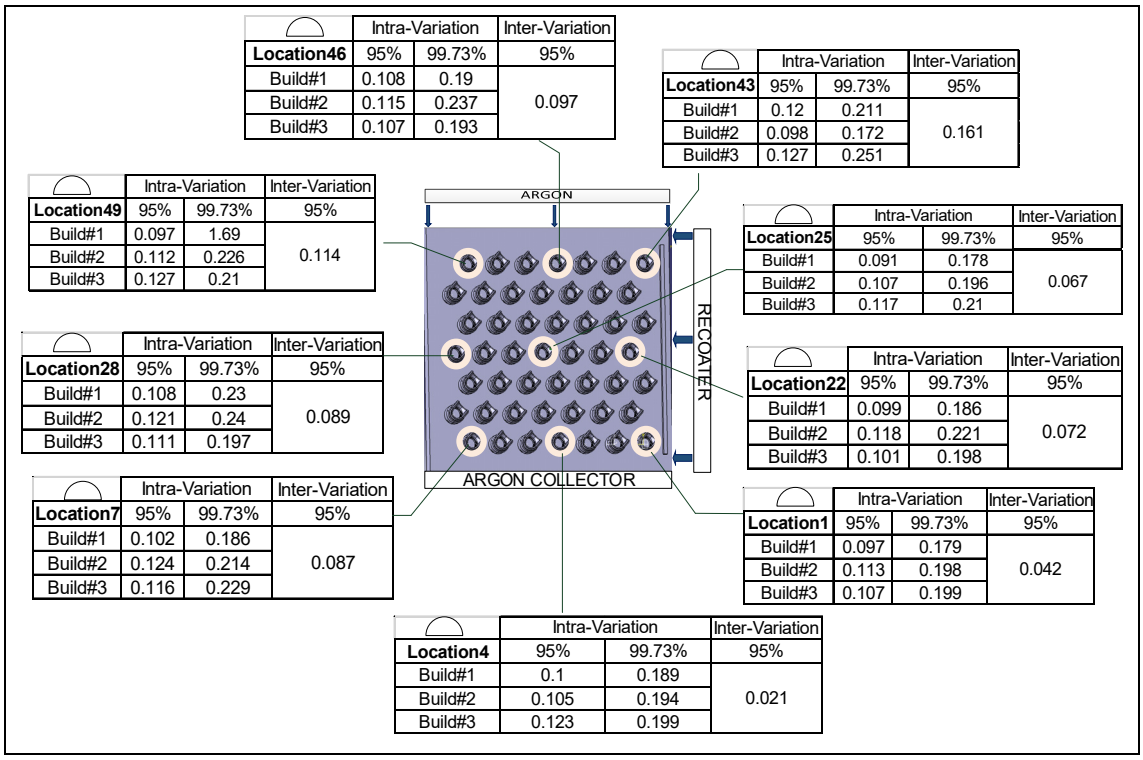

Figure 2.10 **.** Intra and inter-variation of part profile deviation study (mm).

Tableau 2.3 3D profile deviation (mm) and equivalent IT grade (International Tolerance Grade defined in ISO 286).

Build	$\mu_{\frown}$	$StDev_{\frown}$	**95%**	**97.73%**
#1	0.005	0.034	0.136	0.240
#2	0.000	0.032	0.127	0.225
#3	−0.002	0.030	0.121	0.191
Overall	0.001	0.032	0.128 (IT 11)	0.228 (IT 12)

2.4 Discussion

After the first build, neither the second nor the third build showed any similarity in terms of the distribution (pattern) of the 3D profile deviations in the manufacturing chamber. Globally, the deviation values are in the same range, but their distribution in the chamber is not repeating. We can then conclude there is no specific pattern of geometric deviations on the chamber for LPBF process with an EOS M280. The measured range of the intra-build means variations are

0.100 mm for the first build, 0.071 mm for the second, and 0.054 mm for the third build. The inter-build variation range is 0.104 mm. The intra-build variations are practically constant even if their distribution on the build plate is not similar. The observation of Figure 2.7 highlights more withdrawal in Build #3 than Build #2 (Figure 2.11-a). However, since the magnitude of the differences between the two builds is lower than the measurement equipment uncertainty which is ±5 µm, we cannot really conclude on the absence of any significant difference between these builds. The range of the intra-build diameter (Ø19.05 mm) variations at z = 1.2 mm is 0.273 mm for the first build, 0.144 mm for the second, and 0.159 mm for the third build. The overall diameter deviation variation range is 0.307 mm (Figure 2.11-b) which corresponds to an equivalent IT Grade IT 13. The 3D profile deviation behavior of the 147 parts falls within 128 µm at a 95% level, which corresponds to an IT 11. The 3D profile capability interval (99.73%) for the process is 228 µm, which is an IT 12 equivalent, comparable to turning and milling process tolerance.

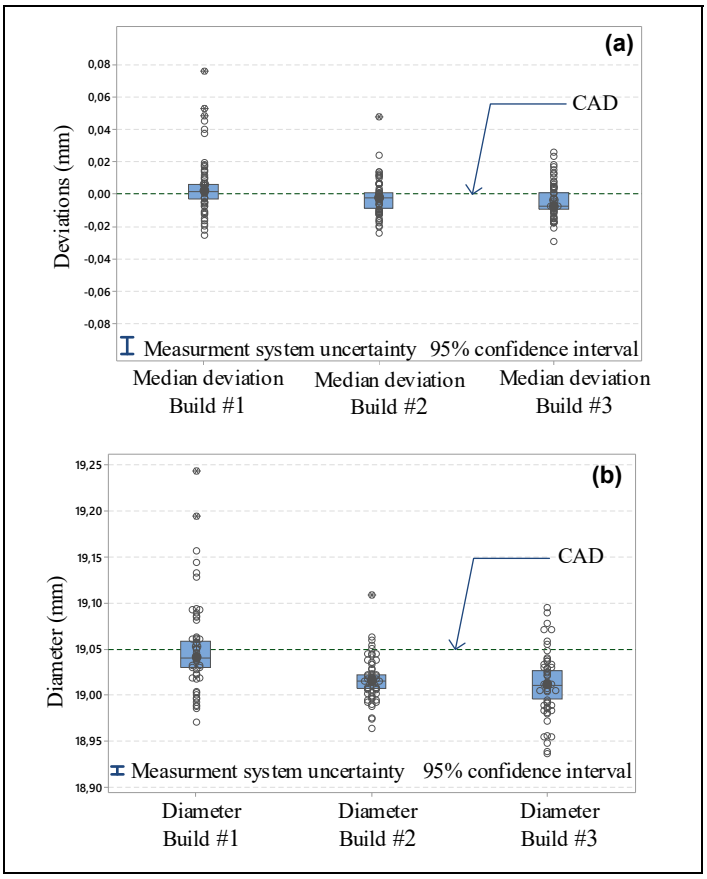

Figure 2.11 Box plot of the profile deviation (**a**) and diameter deviation (**b**).

2.5 Conclusions

This paper presents a metrological investigation carried out on 147 typical aerospace tooling components built in three print jobs using an AlSi10Mg powder and an EOS M280 LPBF system. The investigations were limited to the overall 3D profile and diameter deviation studies, specifically to their repartition in the build chamber. No significant statistical differences were revealed between the 49 locations over the three builds, and the deviation distribution in the build chamber appeared to be non-repeatable. However, inspection of part external diameters reveals a correlation between this feature and the overall 3D profile deviation. In fact, it was shown that the magnitude of these deviations is in the same range as the measurement equipment uncertainty, which is ±5 µm. Further studies with different geometries, such as cylinders, holes, cubes, and cones, could be promising.

The results of this study, and of the upcoming ones, will have a positive impact on increasing the competitiveness of the LPBF process. The findings of the study can also be directly applied to high technology industries, such as aerospace and automotive sectors, planning to use the metallic AM technology in their production cycle.

Author Contributions: The project objectives and methodology were proposed by A.T. and V.B. The specimen fabrication, scanning and data treatment were carried out by F.Z. with the help of A.T., V.B. and A.A. The article was written by F.Z. and revised by A.T., V.B. and A.A.

Funding: This research received no external funding.

2.6 Acknowledgments

The authors would like to thank the *Natural Sciences and Engineering Research Council* of Canada (*NSERC*) and *École de technologie supérieure* (*ETS*) for their supports. The authors are thankful to Joel Grignon, Anatoli Timercam, Morgan Letteneur, and Jean-René Poulin who assisted in this research.

Conflicts of Interest: The authors declare no conflict of interest

CHAPITRE 3

SCALE, MATERIAL CONCENTRATION, STRESS RELIEF AND PART REMOVAL EFFECTS ON THE DIMENSIONAL BEHAVIOUR OF SELECTED AlSi10Mg COMPONENTS MANUFACTURED BY LASER POWDER BED FUSION

Floriane Zongo, Antoine Tahan * and Vladimir Brailovski

Department of Mechanical Engineering, École de technologie supérieure (ÉTS), Montreal, QC H3C 1K3, Canada; teega-wende-floriane.zongo.1@etsmtl.net (F.Z.); vladimir.brailovski@etsmtl.ca (V.B.)
*Correspondence: antoine.tahan@etsmtl.ca (A.T.); Tel.: +1-514-396-8687
Received: 2 May 2019 / Accepted: 13 June 2019 / Published: 18 June 2019

Abstract: Laser Powder Bed Fusion (LPBF) is one of the most predominant Additive Manufacturing (AM) processes. While metallic LPBF is gaining popularity, one of the barriers facing its wider industrial use is the current relatively limited knowledge with respect to its dimensional and geometrical performance, as well as the inability to predict it. This paper presents an experimental investigation of the geometrical and dimensional deviations of selected LPBF-manufactured components according to ASME Y14.5 (2009) standard. In this study, two types of axisymmetric parts (cylinder and cylindrical pyramid) were designed with three different levels of material concentration, and replicated at three different scales for a total of 18 test artifacts. These parts were manufactured from AlSi10Mg powder using an EOSINT M280 printer, subjected to stress relief annealing at 300°C for two hours, removed from the platform and finished by micro shot peening. A complete statistical analysis was carried out on the artifacts before and after each post-processing step. The results of this investigation allowed the quantification of the intra- (same part) and inter- (different parts) scale effects, as well as of the material concentration, stress relief, part removal and micro shot peening effects on the overall 3D profile deviations and on the dimensional deviations of some selected features (e.g., diameter, thickness). For example, cylindrical pyramid parts showed the following average deviations of their outside diameters: a -63 µm shrinkage of the as-built part diameter as compared to its CAD value, a +20 µm expansion after stress relief annealing

as compared to the precedent step, a -18 µm shrinkage after part removal and finally, a -50 µm shrinkage, after micro shot peening.

Keywords: Additive manufacturing, laser powder bed fusion; selective laser melting; metrology; material concentration, post-processing; geometrical dimensioning and tolerancing.

3.1 Introduction

Additive Manufacturing (AM) is the term used for technologies that produce 3D functional parts from nominal CAD files using typically layer-by-layer material deposition techniques. These technologies do not require conventional tooling to build components since the shape is produced by adding, rather than removing or deforming, material. The material can be polymer, metal, composite, ceramic, concrete or even human cells. Many AM processes have been developed and are commercially available, including Stereolithography (SL), Fused Deposition Modelling (FDM), Three-Dimensional Printing (3DP), Powder Bed Fusion (PBF), Direct Metal Deposition (DMD), and Sheet Lamination (SL). The PBF technologies include two variants depending on the nature of the heat source: the Electron Beam Powder Bed Fusion (EBPBF) and the Laser Powder Bed Fusion (LPBF). AM standard terminologies are framed by ISO/ASTM 52900:2015 [82] and their general principles are described in ISO/ASTM52901-16 [2].

LPBF is one of the most used processes for metallic AM, which builds three-dimensional parts directly from metal powder. In a chamber filled with inert gas, high power laser beam selectively scans a thin layer of metallic powder, resulting in local melting. Dimensional accuracy prediction and control remains a major concern when it comes to the industrial adoption of this technology.

To investigate the process feasibility and transpose the information collected into the process performance, many researchers have proposed AM test artifacts, which are meant to quantify the capabilities, limitations and accuracy of the machine and the process, and to diagnose specific processing defects [7]. Richter and Jacobs [4] suggested that the standard test artifact should be large enough to test the performance of the machine near the edges of the platform

as well as near the center, have a substantial number of small, medium and large features, and have both holes and bosses to aid in verifying beam width compensation. In addition, it should not take too long to build, nor consume a large quantity of material, and should be easy to measure. Byun et al. [5] added that the test part should also have evaluation features to assess whether or not it is possible to manufacture fine features under the specific AM process. Accordingly, these fine features should be set up in all axes, and their size should be varied while considering the improvement in the process mechanisms and resolutions of AM machines. Kruth et al. [6] stated that such artifacts should not only be used to analyze the process limitations, but also to optimize the process iteratively. Some other authors have made notable advances in the field of AM artifact design [8, 9, 23, 27, 33, 34, 39, 42-45].

Globally, to date, researchers have focused more on the feasibility issues and less on the statistical effects of processing and post-processing operations on final part deviations. Knowing that geometrical deviations strongly impact the service performance of structural parts, this lack of reliable metrological information hinders widespread industrial adoption of AM technologies.

To fill this gap, different authors have studied and tried to predict dimensional and geometrical deviations of AM parts with varying levels of success. For example, Singh et al. [61] quantified the effects of laser power, scan spacing, powder bed temperature, hatch length and scan count on the geometrical deviations of SLS polyamide parts. Next, Huang et al. [83] investigated the compensation of the geometrical deviations on SLA SI500 (resin) parts. They presented a statistical predictive compensation approach to predict and improve the quality of cylindrical and prismatic parts. However, only the XY plane deformation errors were taken into account, while the Z coordinate was ignored. Moreover, after the compensation, the parts still presented the same systematic deformation pattern as before, and only the average profile deviation was improved, but not entirely corrected.

Similar works can be found on metal AM. For example, Zongo et al. [84] carried out an intra- and inter-repeatability study of profile deviations, and the results of the investigation demonstrated that the LPBF performance for geometrical variations of 147 identical AlSi10Mg parts falls within a range of 230 μm at a 99.73% confidence level. Using the same process, powder and stress relief annealing heat treatment, Calignano et al. [85] studied the dimensional

limits of geometries with sharp edges. They quantified the effect of STL file tolerances on the printed part deviations. Next, Van Bael et al. [63] investigated the geometrical controllability of LPBF-built Ti6Al4V porous structures by means of a feedback loop between the design and the printed part deviations. After two iterations, the average pore size mismatch was decreased from 45 to 5%. Li et al. [86] investigated the effect of micro-vibrations on the final part porosity and mechanical properties. They demonstrated that 969 Hz vibrations can decrease the density of AlSi10Mg parts printed using a KUKA six-axis robot from 100 to 99.1%. Next, Liu et al. [87] demonstrated that if each layer is scanned twice, the part density increases by 0.1%, and if it is scanned three times, the density is increased further by 0.3%. It is evident that these modifications in processing sequence must have affected not only the part density but also its geometry; this last aspect was not considered in these works.

Notwithstanding the above, the number of metrological studies of AM processes is still limited. This paper isolates and quantifies the intra- (same part) and inter- (different parts) scale effect, and the material concentration, stress relief, part removal and micro shot peening effects on the 3D profile deviations of selected simplified test components. The results of these analyses can serve as an accessible experimental database for the validation of numerical models intended to predict the geometrical and dimensional deviations of LPBF parts. The ultimate goal of this study is to improve the design support for the LPBF technologies.

The paper is organized as follows: Section 2 describes the part used and the experiment protocol followed. The results are presented and discussed in Section 3. Finally, a summary is provided and future work is described in Section 4.

3.2 Methodology

To isolate, test and quantify the effects influencing LPBF part geometrical deviations, two test artifacts were designed. The first, referred to as Shape A artifact, is a cylindrical part containing a coaxial cylindrical pocket displaying a diameter of half of the full cylinder (Figure 3.1). This artifact was manufactured in 12 versions. The variables are the pocket depth (from P1 being ¼ depth to P4 completely hollow) and the part size (from S1 small to S3 large), as described in Figure 3.1. Shape B artifact is a 4-step cylindrical pyramid. This artifact was manufactured in

6 versions. The variables are the absence or presence of a coaxial pocket with a diameter of half of the smallest cylinder (P0 means no pocket and P4 stands for completely hollow) and the part's relative scale S1-S3, as described in Figure 3.1.

The pocket depth variant (P) allows for the isolation and quantification of the impact of the material concentration on the part deviations, while the scale variant (S) allows the isolation and quantification of the impact of the scale effect on the part deviations.

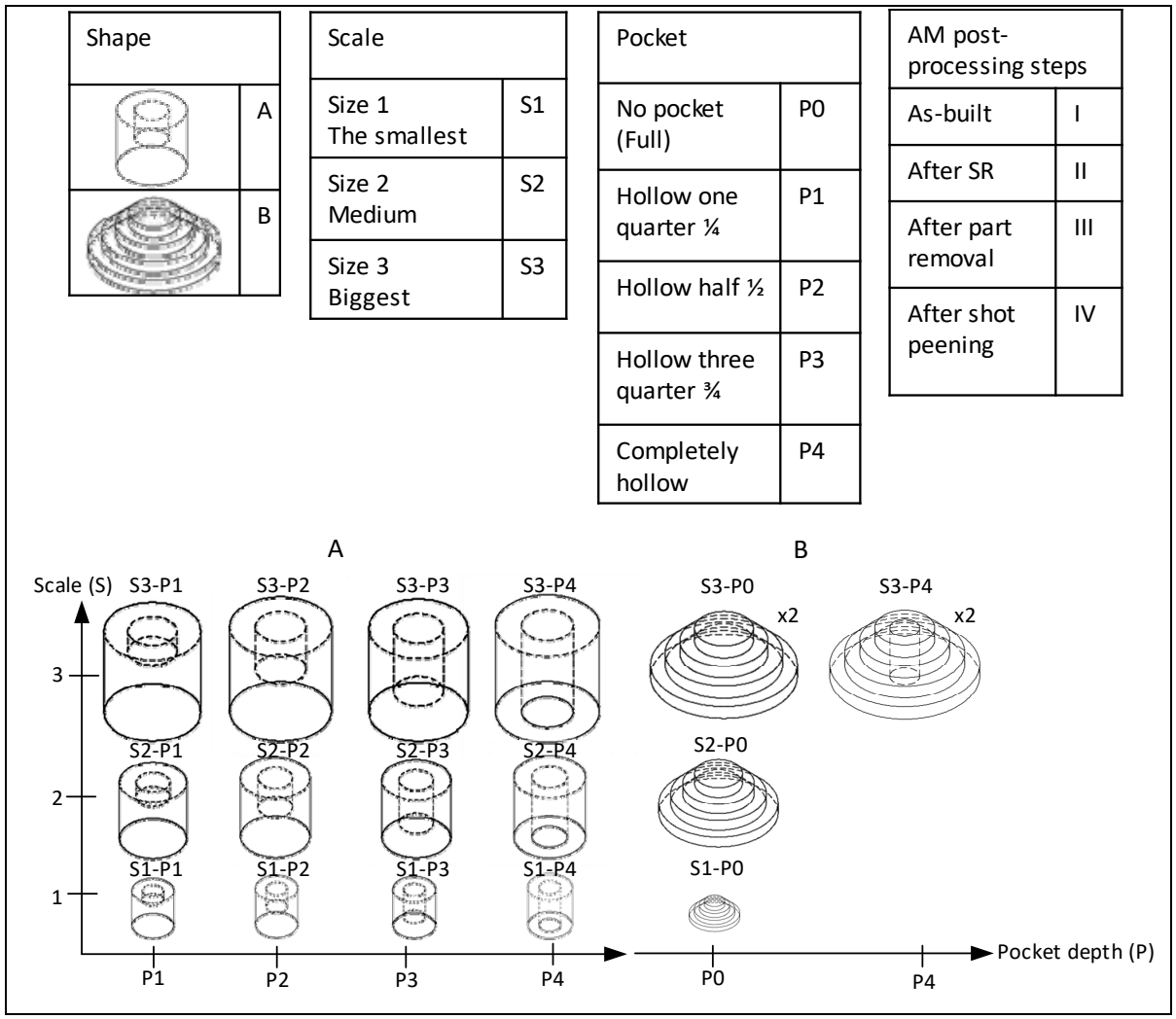

Figure 3.1 Variants of test artifacts used.

All the parts of this study were printed using an EOSINT M280 system (EOS, Germany), and AlSi10Mg powder with AlSi10Mg_Speed 103 process parameter set (laser power 370 W,

scanning speed 1300 mm/s, hatching space 0.19 mm, and layer thickness 30 µm). The AlSi10Mg powder used has a particle size distribution of D10=12.8 µm, D50=27.7 µm and D90=51.3 µm; the tap density 1.358 g/cm^3; the apparent density 1.081 g/cm^3, and the Hausner ratio 1.256 [88]. Prior to printing the test artifacts, a beam offset calibration was performed. To this end, the calibration part was printed and inspected (Figure 3.2-a). The part was then scanned by means of a Renishaw PH10 probe mounted on a Mitutoyo Coordinate Measuring Machine (CMM) (4 µm accuracy at a 95% confidence level). Data were collected on the as-built part and after stress relief of 300°C for two hours. The results of the as-built part inspection were used to assess the quality of the beam offset correction protocol suggested by the LPBF system manufacturer.

After the beam offset correction, eighteen (18) AlSi10Mg artifacts were printed using the same LPBF system, material and parameters for the calibration part (Figure 3.2-b). The point cloud of the parts printed was obtained by means of a Metris LC50 laser scan mounted on a CMM (≈7 µm accuracy at a 95% confidence level) (Figure 3.2). Before each scan, the devices were calibrated using a master sphere and data collection was performed under multiples angles to maximize the information collection on inner surfaces. A real-time visualization was possible with the Focus Inspector, a specialized software application. A thin layer of talcum powder was used to reduce part surface reflection. As a result, the potential point cloud density was increased to ensure the best measurements. The point clouds were then assembled from different angles and cleaned. Following a first Geometrical Deviations Extraction (GDE), a second GDE was carried out after stress relief annealing at 300°C for two hours, as recommended by the LPBF system manufacturer. The heat treatment was conducted under argon atmosphere followed by air-forced cooling down to room temperature. Next, a third GDE was carried out after the parts were removed from the plate using a 2°mm thick saw on a horizontal set up. Finally, as suggested by the LBPF system manufacturer, micro shot peening was then applied using an IEPCO MICRO 750 S system with the IEPCONORM-A agent (0.2-0.4 mm grain size of crushed corncob), applied with a 3 bar pressure at the perpendicular angle to the specimen surface, at 3-5 cm distance, before the fourth and final GDE. The Gaussian best-fit technique and data alignment were performed on the GDEs using PolyWorks® v.16 (Innovmetric Metrological Software). The data were then loaded into Matlab® 2017b

(MathWorks), using a code to extract the deviation at each point. Minitab® v.17 (statistical software by Minitab Inc.) was used for the graphic and statistical studies.

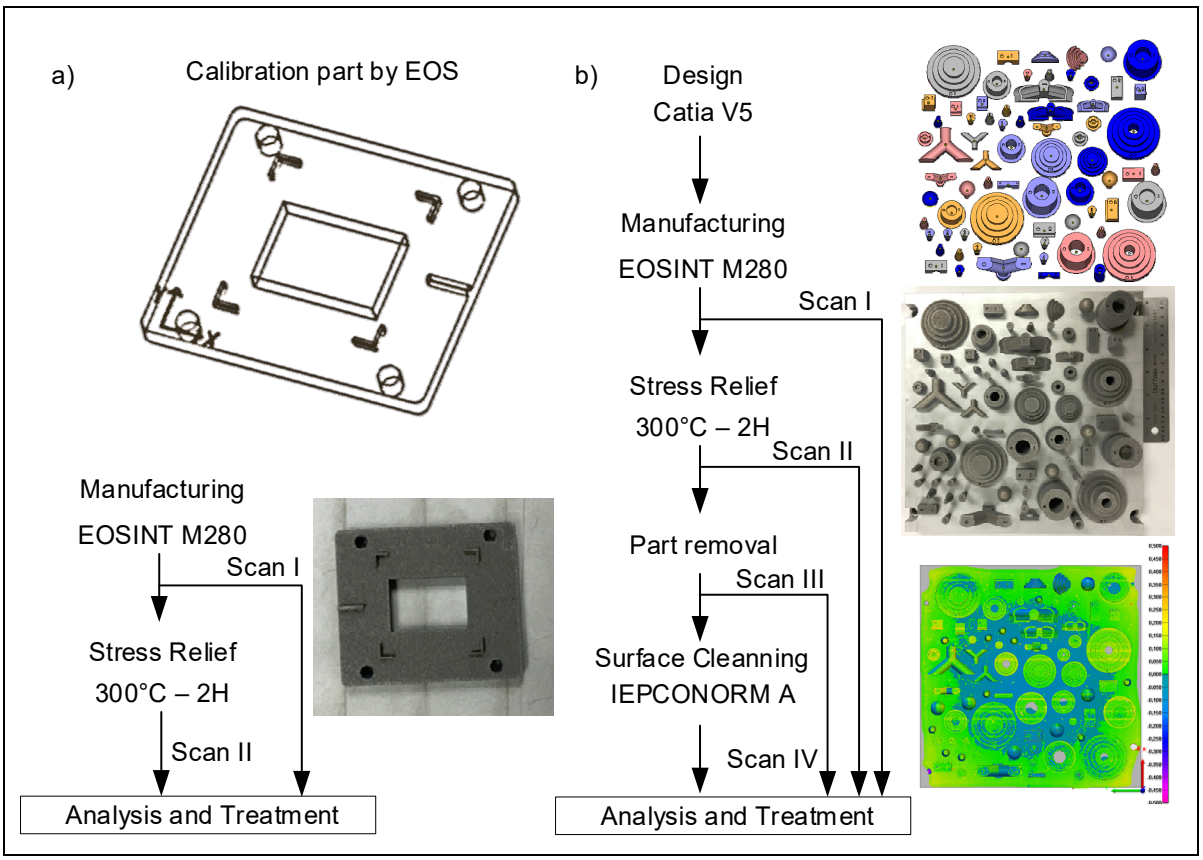

Figure 3.2 Experimental protocol: a) Beam offset correction, b) Test artifacts GDEs.

To sum up, the calibration analysis (Analysis A), and three types of deviation analyses were performed based on the ASME Y14.5 (2009) tolerancing standard: The scale effect analysis (Analysis B), the part material concentration effect analysis (Analysis C), and the post-processing effect analysis (Analysis D). Each of the deviation analyses was carried out using Shapes A and B artifacts.

Analysis A - Calibration part

The calibration part inspection was conducted according to the plan provided by EOS. The plan specifies which feature needs to be inspected (see Figure 3.3-a), and how to use the provided Excel sheet to calculate the beam offset, using the results of such an inspection. This

analysis was carried out using the part inspection results. The correlation between the feature inspected nominal size and the stress relief effect was investigated.

Analysis B - Scale effect

The scale effect analysis was carried out using Shapes A and B. First, an intra-part scale effect (scale effect on different features of the same printed part) was carried out using four cylindrical features of Shape B artifacts presented in Figure 3.3-b.

An inter-part scale effect study (comparing the same shape with different part sizes) was carried out using Shapes A and B. Regarding Shape A artifact, the as-built external diameter deviations were extracted and compared for three different sizes, S1, S2 and S3 (Figure 3.3-a). For the Shape B artifact, the 3D profile deviation nonparametric cumulative distribution functions (CDF) of all the parts at S1 and S2, as well as of two parts with no pocket (P0) at S3, were used for this study (Figure 3.3-b).

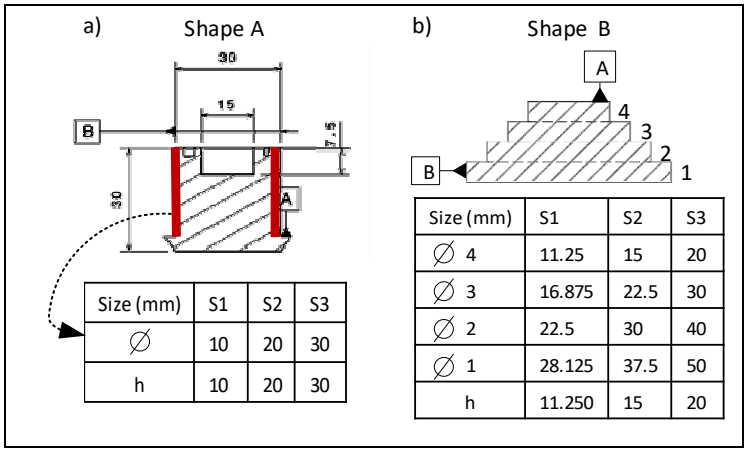

Size (mm)	S1	S2	S3
∅	10	20	30
h	10	20	30

Size (mm)	S1	S2	S3
∅ 4	11.25	15	20
∅ 3	16.875	22.5	30
∅ 2	22.5	30	40
∅ 1	28.125	37.5	50
h	11.250	15	20

Figure 3.3 Features inspected with nominal dimensions indicated in tables.

Analysis C - Material Concentration effect

In topology optimization, the material concentration or “pseudo-density” factor describes the layout of the material in a part within a given design space [22]. In this study, the material concentration effect was studied by means of the pockets variant (P0-P4) (Figure 3.1). To this end, A-S3-P0 and A-S3-P4 artifacts were printed twice on the plate to confirm the material

concentration effect on each of the two parts with different pocket depths. Comparisons were made between parts with the same global shapes and sizes, but pocketed at different depths. Regarding the Shape A artifact, the material concentration effect was studied using the 3D profile deviation of artifacts having four different pockets depths (P1-P4). The results are presented at each post-processing step (PPS). The parts used are at their biggest scale (S3). With the Shape B artifact, the part material concentration effect was studied using the 3D profile deviations of two P0 and P4 pockets depths, with each variation being printed twice. The mean 3D profile deviation is presented at each PPS. The parts used are at their biggest scale (S3).

Analysis D – Post-Processing effect

The post-processing effect was studied by observing overall 3D profile deviations and specific feature evolution before (as-built I), and after each post-processing step (PPS): stress relief (II), part removal (III), and micro shot peening (IV). The analysis was carried out using Shapes A and B. Regarding the Shape A artifact, the overall 3D profile deviation mean values, before and after stress relief and the deviation of the external diameter at each PPS were extracted and presented. The nominal values are specified in Figure 3.3-a. For the Shape B artifact, the overall 3D profile deviation mean values of four parts at S3 were carried out. Furthermore, the diameter deviations of four cylinders of the pyramidal shape (Figure 3.3-b) were extracted on each Shape B artifact, at each PPS.

General note: By definition, the deviation is the difference between the nominal value (as defined in the CAD file) and the experimental value extracted from the measurements. Positive deviation means that the measured value is greater than the nominal in the Maximum Material Condition (MMC) direction. Negative deviation means that the measured value is smaller than the nominal in the Least Material Condition (LMC) direction, as in ASME Y14.5.1 [23]. The interval bars presented on the graphics are the measurement system uncertainty at a 95% confidence level.

3.3 Results and discussions

The geometrical and dimensional analysis (GD and T) analysis is based on the ASME Y14.5 (2009) standard and provides the following information: (A) the calibration part deviations behaviour before and after the stress relief, (B_1) the intra-parts and (B_2) inter-parts scale effects on the Shapes A and B artifacts (18 parts), (C) the part material concentration effect, and (D) the post-processing steps effect. This section displays some analytical graphs (Refer to Appendix 3B for numerical values).

Analysis A - Calibration part inspection

The calibration part inspection results are presented in Figure 3.4-c and Figure 3.5. Figure 3.4 presents the deviations before the stress relief (blue) and after the stress relief (red). The numbers next to each point refer to the inspection map (Figure 3.4-a,b). The measurement system used has an accuracy of 2 µm at the 95% level. Figure 3.5 presents the difference between the same measurements before and after the stress relief depending on the nominal dimension inspected (after SR - before SR). On the vertical axe, zero value means no differences in the feature inspected before and after SR. Positive values mean there was an SR-induced expansion of the feature inspected, while negative values mean an SR-induced shrinkage of the feature inspected.

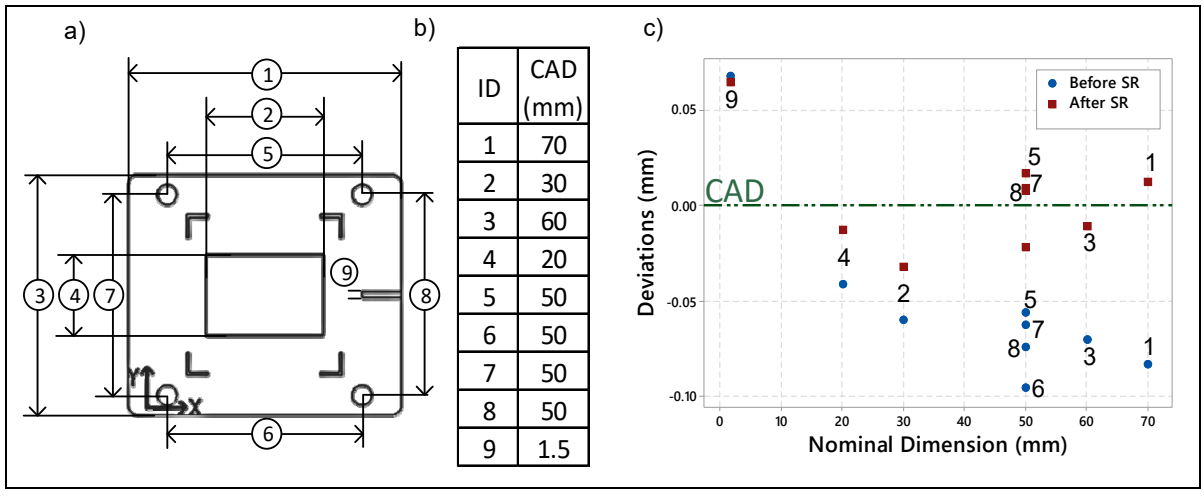

Figure 3.4 a) Calibration part inspection plan, b) nominal values of the features inspected, and c) inspection results.

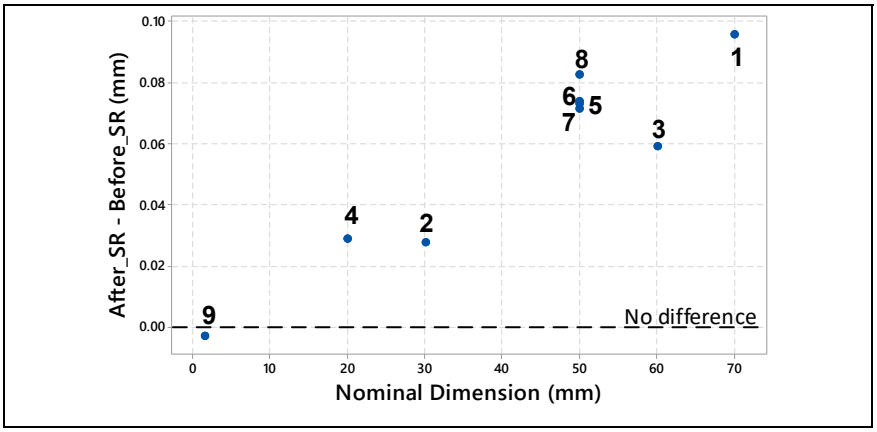

Figure 3.5 Stress relief effect depending on the feature nominal size.

We can observe in Figure 3.4 that after the stress relief, the distances measured on the calibration part are globally closer to the CAD than before it. This can be attributed to the reduction of internal stresses and therefore part distortions after this treatment.

In addition, the difference between the before and after stress-relief states seems to be proportional to the feature size (Figure 3.5). The distances 1, 3, 5, 6, 7, and 8 have a nominal value varying from 70 to 50 mm. The stress relief expanded them to an average of +60 µm in terms of feature expansion. The distances 4 and 2 have a nominal distance of 20 and 30 mm respectively. The stress relief expanded them to an average of +25 µm. The distance 9 has a nominal value of 1.5 mm. The stress relief shrinked it by -3 µm.

Analysis B_1 – Intra-part scale effect

The intra-part scale effect is the scale effect observed in features with different scales, inspected on the same part. Given that the Shape A artifact doesn't present features eligible for this analysis, the intra-part scale effect is only quantified and observed using Shape B artifact.

Shape B artifact

Figure 3.6 presents the diameter deviations at each of the four steps of the pyramidal shape. Each color represents the four diameters of the same part. Each line was fitted with the deviations of the four diameters of the same part. The measurements presented here were carried out in the as-built state (I). The figure highlights the intra-part scale effect, which is the

repartition of the deviations of the same part, depending on the nominal size of the inspected feature.

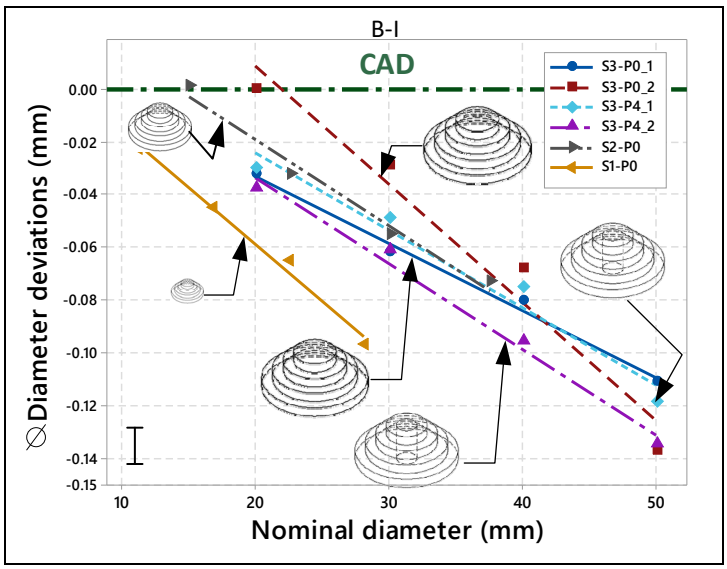

Figure 3.6 Intra-part scale effects of Shape B artifact carried out as-built, based on their cylinders diameters.

This study reveals a scale effect on different features of the same part. Each of the 6 parts of Shape B reveals an intra-part scale effect (Figure 3.6). The amplitude of this intra-part scale effect seems to be correlated to their feature nominal intra size amplitude, which is a difference between the maximum and minimum sizes of the features of the same part. The four S1 parts have a feature nominal intra size amplitude of 30 mm and an intra-part scale amplitude of 97 to 137 µm. The S2 and S3 parts have a feature nominal intra size amplitude of 22.5 and 17.1 mm, respectively, and an intra-part scale amplitude of 74 µm for both parts. Collecting more data is needed to confirm this relationship.

Analysis B_2 – Inter-part scale effect

Shape A artifact

Figure 3.7 presents the external diameter deviations of 12 Shape A artifacts. Each column presents the deviations of the 4 parts having the same scale.

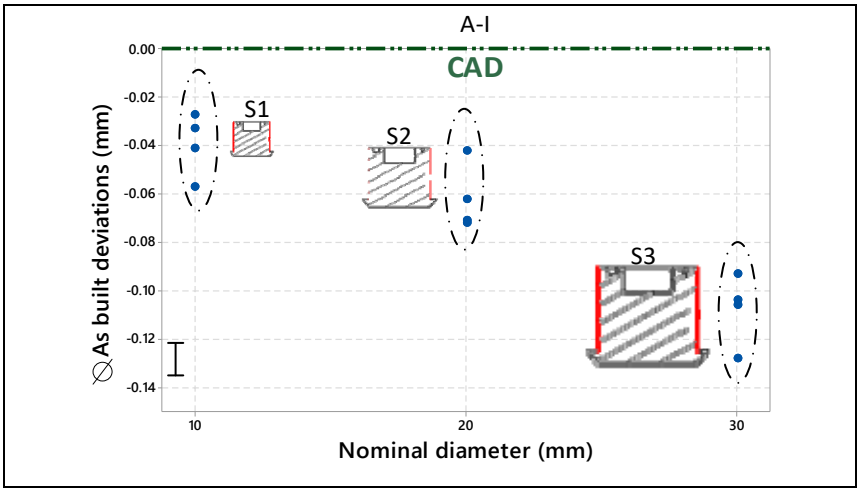

Figure 3.7 **.** Inter-parts scale effects of Shape A artifact (as-built state), based on their external diameter (highlighted in red).

The external diameter study of the 12 Shape A artifacts reveals and allows us to quantify an inter-part scale effect with a mean deviation of -39 µm shrinkage (-0.39%) on the (P1 to P4) S1 parts, -61 µm shrinkage (-0.3%) on S2 parts and -107 µm shrinkage (-0.35%) on S3 parts. The deviations clearly show a scale effect with a relative shrinkage more or less stable for the 12 parts.

Shape B artifact

Figure 3.8 presents the 3D profile deviation nonparametric cumulative distribution function of the parts with no pocket (P0) after the part removal (III). We can observe the scale effect between the four parts with three different scales.

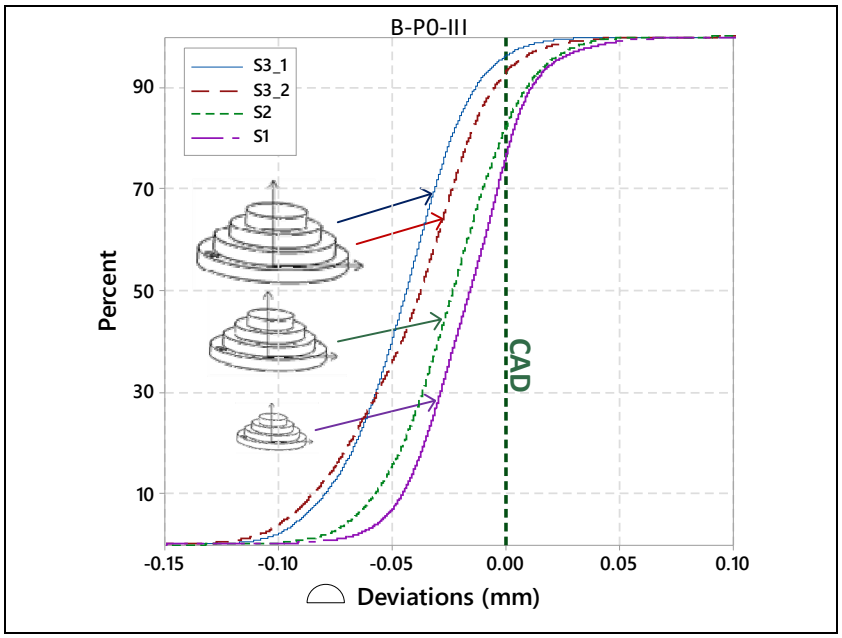

Figure 3.8 Non parametric cumulative distribution functions of four Shape B artifacts with no pockets (P0), carried out after part removal.

The nonparametric cumulative distribution function of the Shape B artifact deviation shows, and allows us to quantify, an inter-parts scale effect. The part B-P0-II-S3_1 (blue) 3D profile mean deviation is -44 µm. B-P0-II-S3_2 (red) mean deviation is -41 µm. B-P0-II-S2 (green) mean deviation is -23 µm. B-P0-II-S1 (purple) mean deviation is -16 µm.

Analysis C - Part material concentration effect

Shape A artifact

The part material concentration effect was tested using the differences in the deviations of the part having the same shape and scale, with some pockets at different depths. Figure 3.9 presents the 3D profile mean deviations of the parts having the same shape (A) and scale (S3), with different pocket depths P1 to P4. This figure highlights the material repartition effect on the profile deviations at each PPSs.

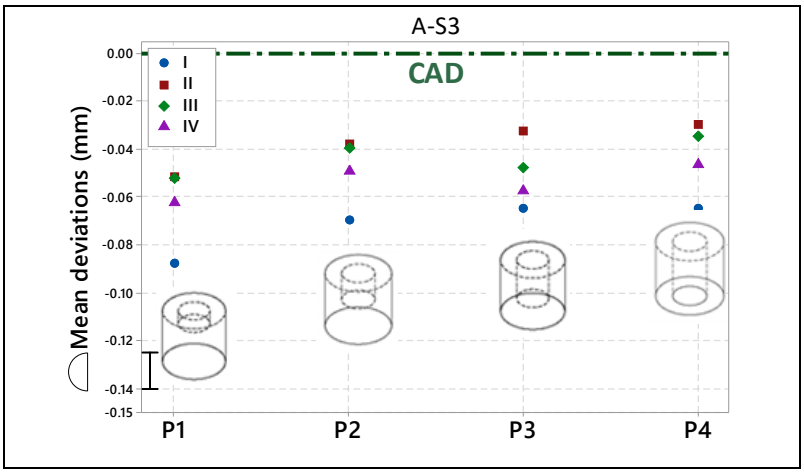

Figure 3.9 3D profile mean deviations of Shape A artifact having the biggest size S3 at each post-processing steps; Scan I as-built; Scan II after stress relief; Scan III after part removal, and Scan IV after shot peening.

The 3D profile mean deviation study of the 4 Shape A and Scale 3 artifacts seems to reveal a correlation between the part material concentration and the deviations. For the same size given, there appear to be less deviations in parts with less material concentration (manifested here by a deeper pocket) than in parts with the same shape, at the exception of a shallower pocket, and thereby, more material concentration. Collecting more data is needed to confirm this relationship. The same effect was observed with the Shape B artifact. The analysis is in Appendix 3A.

Analysis D – Post-processing effects

Shape A artifact

Figure 3.10 present the overall 3D profile deviation 95% interval of the 12 Shape A artifacts before (I) and after the stress relief (II).

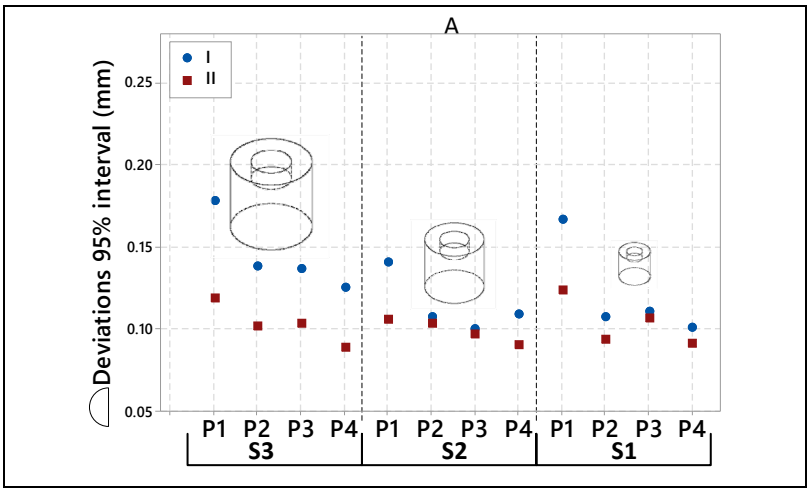

Figure 3.10 Nonparametric distribution function 95% interval of the 12 Shape A artifacts carried out as-built (blue) and after stress relief (red).

Figure 3.11 presents the 3D profile deviation mean value of 4 Shape A artifacts, only at S3, for the four different pocket depths P1-P4, at each PPS. This graph highlights the PPS effects on the profile deviations.

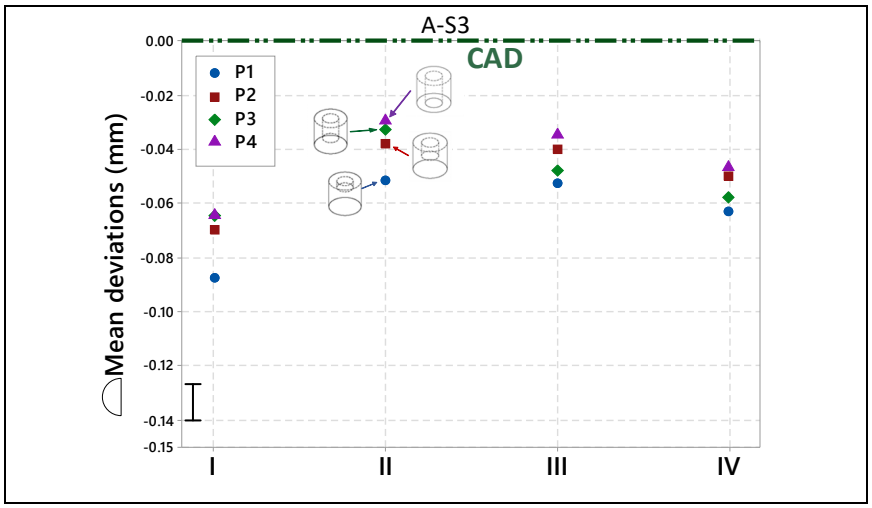

Figure 3.11 3D profile mean deviations of the Shape A artifact having the biggest size S3, carried out at each post-processing steps (as-built I, after stress relief II, after part removal III, and after shot peening IV); P1-P4 pocket depths.

Figure 3.12 presents the results of the extraction of the external diameter of Shape A artifact at each PPS. Each graph shows the deviations at one PPS. Each column corresponds to one

scale, and each colour, to one pocket depth. The numerical values are available in Appendix 3B.

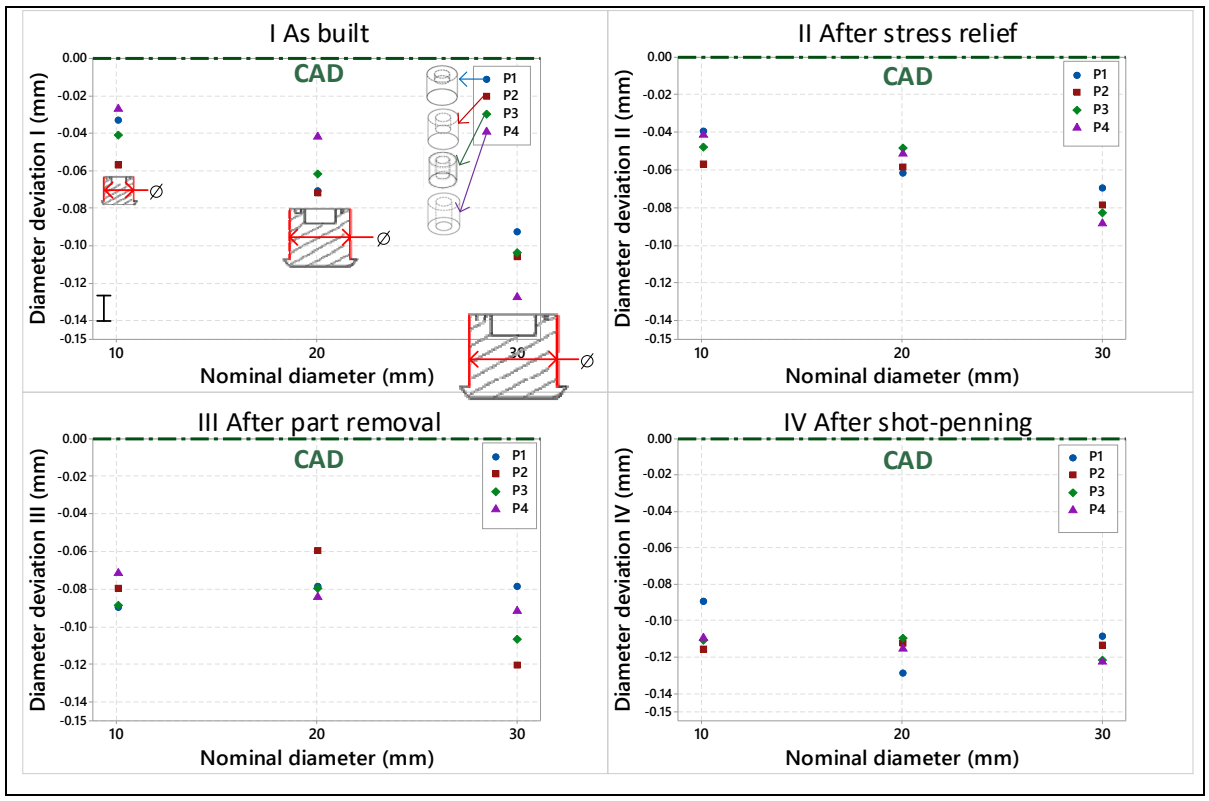

Figure 3.12 External diameter deviations of 12 Shape A artifacts at each post-processing steps (as-built I, after stress relief II, after part removal III, and after shot peening IV); P1-P4 pocket depth.

The stress relief effect can be observed in the overall 3D profile deviation 95% interval. By releasing the residual stresses and preventing part distortions, this PPS positively affects the overall 3D profile deviations by slimming its non-parametric distribution function at a 95% interval (Figure 3.10).

Figure 3.11 reveals the PPS effects on the overall 3D profile deviations for Shape A artifact, only at S3, for the four pockets depths P1-P4. We can observe that the part deviations in the as-built state (I) are in this case, the largest of the PSSs (-65 to -88 µm). This can be attributed to the residual stresses resulted from the repeated thermal expansions and contractions on the fused layers, as observed by Panda and Sahoo [89]. After the stress relief, the part deviations decrease and get closer to the CAD from +32 to +35 µm. The same observation was made by Aidibe et al.[90] on Inconel 718 parts. After part removal, the deviations increase from -1 to -

15 µm. The micro shot peening removes material (unfused particles) from the surface and affects the overall 3D profile deviation mean value by an average of -10 µm. From the SR to the PR states, the part deviations increase by -10 to -25 µm on the parts.

As mentioned before, there is a scale effect on the as-built parts, and SR has an effect proportional to the part scale. Those two facts result in a less severe scale effect between parts after SR, as observed in Figure 3.12. After stress relief, the part diameter deviations decrease at an average of +9 µm (II-I). After PR, each part shrinks for an average of -25 µm (III-II). After shot peening, shrinkage of each part diameter increases for an average of -27 µm (IV-III). This evolution of the diameters mean deviations at each PPS can be observed inFigure 3.15.

However, the scale effect remains after all the PPS for the part having the greater material concentration, Shape A (P1) artifact (Figure 3.12). Collecting more data is needed to confirm that the scale effect is more persistent to the PPS on the massive shapes.

Shape B artifact

Figure 3.13 presents the diameter deviation of Shape B artifact, at each PPS. Each colour represents one size of nominal diameter and each point represents a distinct diameter. There are 6 parts (all Shape B artifacts) × 4 (diameters at each of the four steps of pyramidal shape of one part), which makes 24 points represented. The 24 diameter deviations are presented at each PPS. The streaked line is a no effect line, which means that a point on this line has not changed during the post-processing presented. The graph highlights the PPS effects.

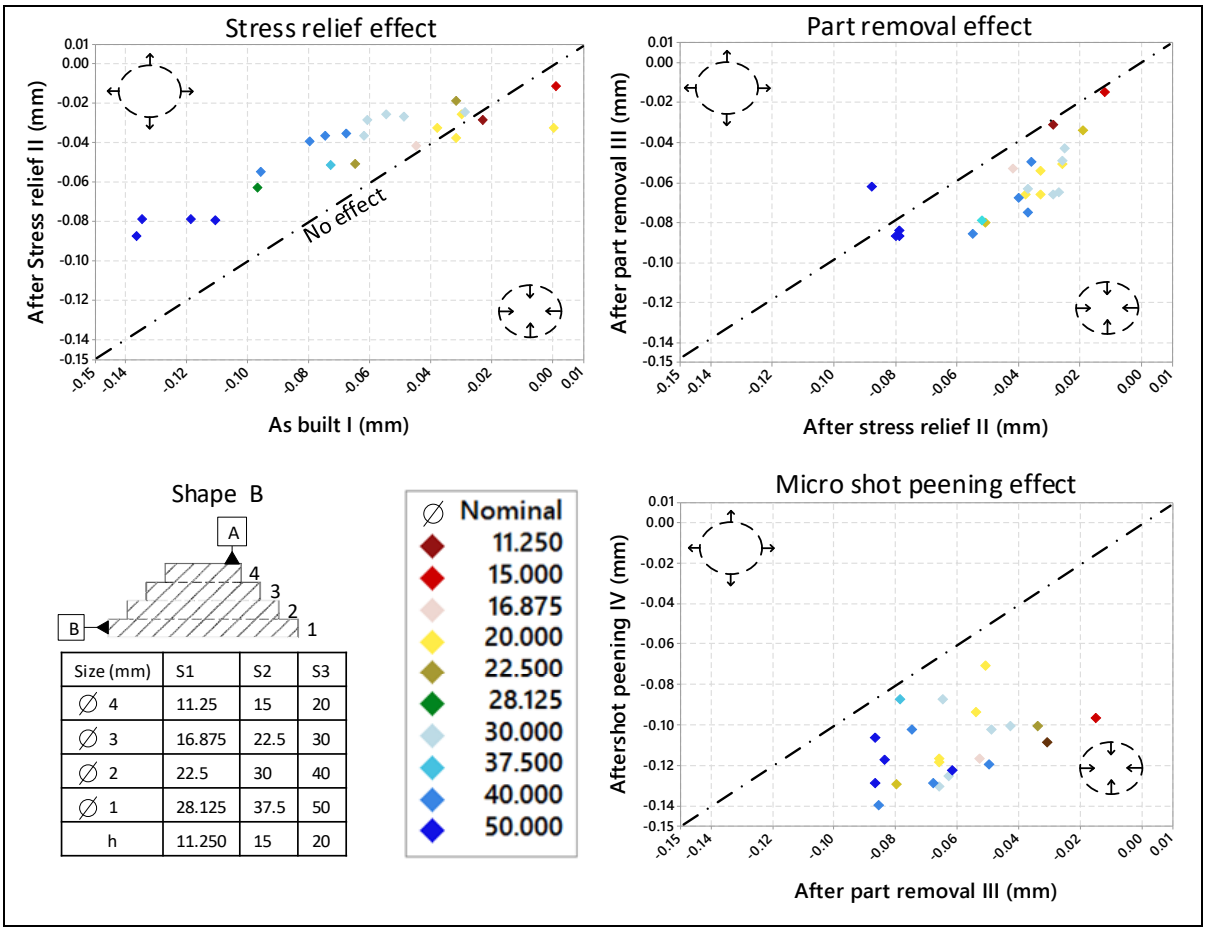

Size (mm)	S1	S2	S3
∅ 4	11.25	15	20
∅ 3	16.875	22.5	30
∅ 2	22.5	30	40
∅ 1	28.125	37.5	50
h	11.250	15	20

Figure 3.13 . Post-processing step effects on the external diameter of 12 Shape B artifacts.

Figure 3.14 presents the 3D profile mean deviation of 4 Shape B artifacts at S3, with two of them having a pocket (P4) and the two others, without pockets (P0). Each column represents the deviation of the 4 parts at one PPS. Each color represents one part. This figure highlights the PPS effect on the overall 3D profile deviation depending on the material concentration.

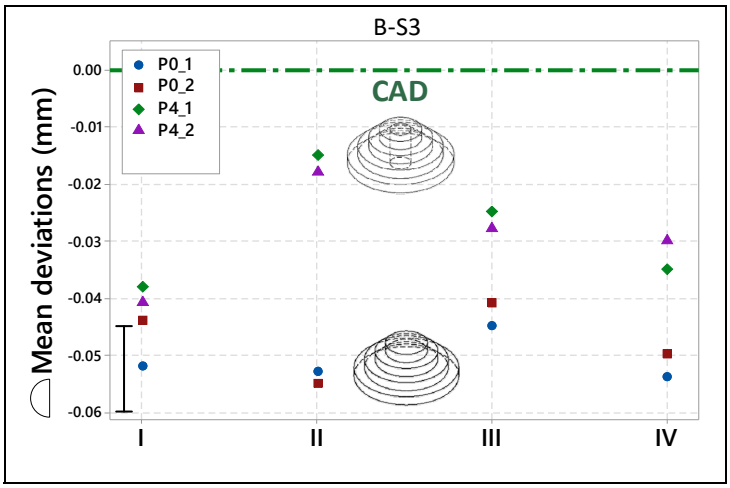

Figure 3.14. 3D profile mean deviations of Shape B artifact having the biggest size S3; P0-P4 designate the absence or the presence of a pocket.

We can observe in Figure 3.13 that the deviations trend depending on the diameter scale are highly affected by the PPSs. As observed earlier with the calibration part (Figure 3.5) and Shape A artifact (Appendix 3A), the stress relief heat treatment affects the dimensions of the artifact by an amplitude depending on their scales. The trend of the colours in Figure 3.13 (I/II) is highly correlated to the scale. Moreover, most of the points are above the no-effect line. That means the diameters have expanded (at an average of +20 µm) after the stress relief. The points of Figure 3.13 (II/III) are under the no effect line. This means that the diameters have decreased after the part removal (at an average of -19 µm). Also, the colour trend demonstrates a less pronounced scale effect. The points of Figure 3.13 (III/IV) are under the no effect line. This means that the part diameters decreased after the shot peening (of an average of -49 µm). The evolution of the diameters mean deviations of Shape B artificat at each PPs can be observed in Figure 3.15.

The part material concentration level seems to have a major effect on the deviation after the SR, as observed in Figure 3.14. For the same shape and scale, at the exception of a pocket, there is a difference in the 3D profile mean deviations of 9 µm as-built, but 38 µm after the SR.

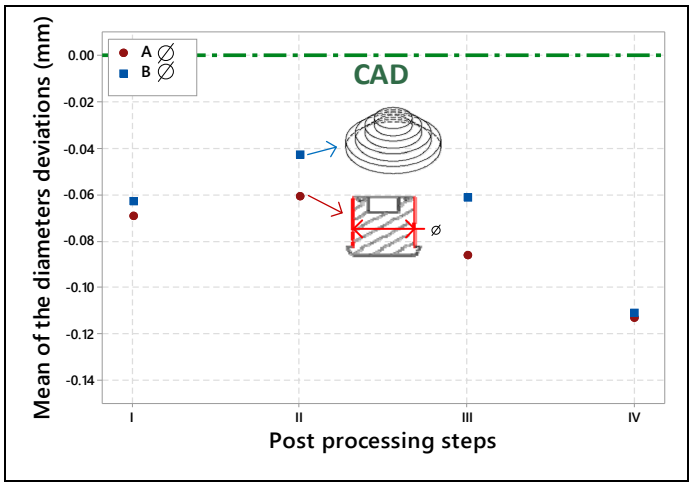

Figure 3.15 Mean of the mean diameter deviation of each shape at each post-processing steps.

3.4 Conclusions

This work is designed to isolate, evaluate and quantify the metrological performances of the laser powder bed fusion of metal powders. It presents and discuss analysis performed on 18 specially designed artifacts printed using AlSi10Mg powder and an EOS M280 LPBF system. The study quantifies the intra- and inter- scale effects, the part material concentration effects, the printing deviations behaviour (I), the stress relief effect (II), the part removal effect (II), and the micro shot peening effect (IV) on the 3D profile deviations of the parts. Based on the results obtained, the following conclusions can be drawn:

- There exists an intra-part scale effect; different features of the same part having different nominal sizes manifest different deviations.
- For the parts of the same size, the less the material concentration, the less the deviations observed.
- Stress relief heat treatment reduces the intra- and inter-part scale effects by expanding (MMC) more the larger features than the smaller features.
- Parts removal operation globally increases the parts deviations.
- Micro shot peening has a positive effect on the surface roughness, but systematically reduces the parts size.

The results of this study will serve as an accessible database of experimental values carried out according to the GD&T ASME Y14.5 (2009) standard. Therefore, they can be used to validate numerical models that aims to predict the geometrical and dimensional deviations of parts manufactured using the same process and machine, with the same powder. Enhancing the efficiency of the design for AM (DFAM) numerical models will have a positive impact on the competitiveness of AM and could boost its adoption by high technology industries where the production cycle would greatly benefit from these technologies.

Author Contributions: The project objectives and methodology were proposed by A.T. and V.B. The specimen fabrication, scanning and data treatment were carried out by F.Z. with the help of A.T. and V.B. The article was written by F.Z. and revised by A.T., and V.B.

Funding: This research received no external funding.

3.5 Acknowledgments

The authors would like to thank École de technologie supérieure (ETS) for their support. The authors are thankful to Joel Grignon, Salah Eddine Brika, Jean-René Poulin, and Ali Aidibe, who assisted in the research.

Conflicts of Interest: The authors declare no conflict of interest.

Appendix 3A

Analysis C - Part material concentration effect

Shape B artifact

Figure 3A.1 presents the 3D profile mean deviation of 4 Shape B artifacts, at the S3, with two of them having a pocket (P4) and the two others not having some pockets (P0). Each column represents the measurements at the 4 PPSs of the same part. This figure highlights the material repartition effect on the overall 3D profile deviation.

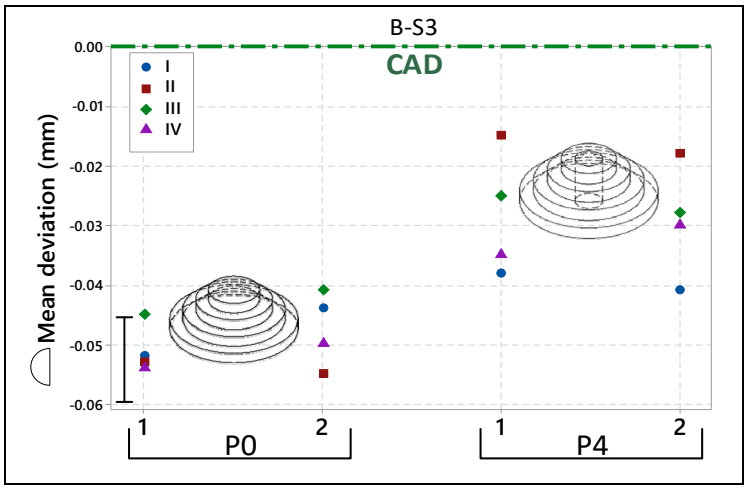

Figure 3A.1 3D profile mean deviations of Shape B artifact having the biggest size S3; Scan I (as-built); Scan II, after stress relief; Scan III, after part removal, and Scan IV, after shot peening.

The 3D profile mean deviation study of 4 Shape B artifacts, with two of them having a P0 and the other two a P4 reveals a clear relationship between the part material concentration and the overall 3D profile deviation. Indeed, for the same shape and scale, at the exception of a pocket, there is a difference in the 3D profile mean deviations of -9 µm as-built, -38 µm after SR, -16 µm after part removal, and -19 µm on the final part (after micro shot peening), for the P0 artifacts, in the Least Material Condition (LMC) direction. With the artifacts with more material concentration (P0 cylinders) always showing more deviations than the artifacts with less material concentration (P4 cylinders), as observed on Shape A artifact (Figure 3.9).

Analysis D – Post-processing effects

Shape A artifact

Figure 3A.2 presents the difference between the overall 3D profile mean deviation of the 12 Shape A artifacts, before (I) and after the stress relief (II). Each point represents the evolution after the SR (after SR - before SR). The graph highlights the SR effects on the overall deviation depending on the part scale.

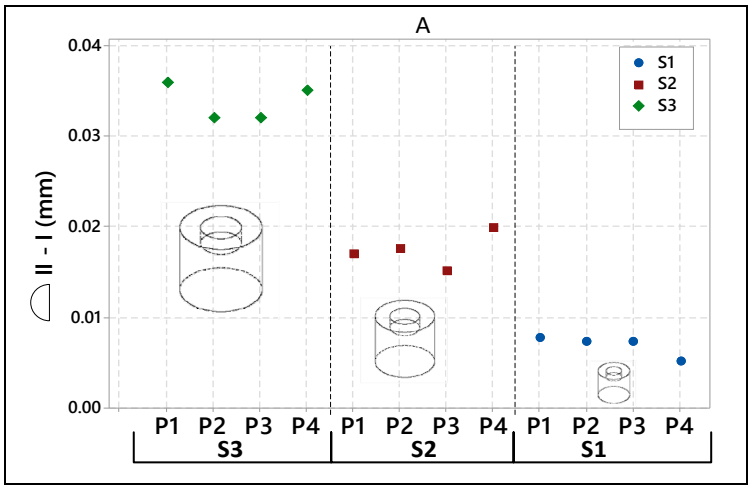

Figure 3A.2 Stress relief effect depending on the feature nominal size for the 12 Shape A artifacts; S1-S3 part size.

The difference between the overall 3D profile mean deviation of the 12 Shape A artifacts before (I) and after stress relief (II) shows that the stress relief effect proportional to the part scale. The S3 part deviations decreased by an average of +34 µm after SR, the S2 parts deviations decrease by +17 µm and the S1 parts deviations, decrease by +7 µm. These results align with the previous observations on the calibration part.

Appendix 3B

Mean values of the overall 3D profile deviation of each part used for this study, including the calibration part, are displayed in Tableau 3A.2, andTableau 3A.4. The deviations are given at each PPS.

Tableau 3A.1 Calibration part inspection results.

CAD (mm)	ID	I		II		II-I	
		(mm)	%	(mm)	%	(mm)	%
70	1	-0.084	-0.12%	0.012	0.02%	0.096	0.14%
30	2	-0.06	-0.20%	-0.033	-0.11%	0.028	0.09%
60	3	-0.071	-0.12%	-0.011	-0.02%	0.059	0.10%
20	4	-0.042	-0.21%	-0.013	-0.07%	0.029	0.15%
50	5	-0.057	-0.11%	0.016	0.03%	0.073	0.15%
50	6	-0.096	-0.19%	-0.022	-0.04%	0.074	0.15%
50	7	-0.063	-0.13%	0.009	0.02%	0.072	0.14%
50	8	-0.075	-0.15%	0.008	0.02%	0.083	0.17%
1.5	9	0.067	4.47%	0.064	4.27%	-0.003	-0.20%

Tableau 3A.2 profile mean deviations of Shape A artifacts at each post-processing steps (as-built I, after stress relief II, after part removal III, and after shot peening IV).

A ⌓ μ (mm)	S3	PPS	P1	P2	P3	P4
		I	-0.088	-0.07	-0.065	-0.065
		II	-0.052	-0.038	-0.033	-0.03
		III	-0.0527	-0.04	-0.048	-0.035
		IV	-0.063	-0.05	-0.058	-0.047
	S2	PPS	P1	P2	P3	P4
		I	-0.045	-0.0355	-0.0411	-0.0459
		II	-0.028	-0.018	-0.0261	-0.0261
		III	-0.047	-0.0311	-0.0337	-0.0409
		IV	-0.05	-0.0399	-0.0415	-0.0462
	S1	PPS	P1	P2	P3	P4
		I	-0.0471	-0.043	-0.0476	-0.03
		II	-0.0394	-0.0357	-0.0403	-0.025
		III	-0.0535	-0.0372	-0.049	-0.0358
		IV	-0.0568	-0.0508	-0.0558	-0.0375

Tableau 3A.3 External diameter deviations of Shape A artifacts at each post-processing steps (as-built I, after stress relief II, after part removal III, and after shot peening IV).

		PPS	P1		P2		P3		P4	
			(mm)	%	(mm)	%	(mm)	%	(mm)	%
A ∅ μ (mm)	S3	I	-0.128	-0.43%	-0.104	-0.35%	-0.106	-0.35%	-0.093	-0.31%
		II	-0.089	-0.30%	-0.083	-0.28%	-0.079	-0.26%	-0.07	-0.23%
		III	-0.092	-0.31%	-0.107	-0.36%	-0.121	-0.40%	-0.079	-0.26%
		IV	-0.123	-0.41%	-0.122	-0.41%	-0.114	-0.38%	-0.109	-0.36%
		PPS	P1		P2		P3		P4	
			(mm)	%	(mm)	%	(mm)	%	(mm)	%
	S2	I	-0.042	-0.21%	-0.062	-0.31%	-0.07	-0.36%	-0.071	-0.36%
		II	-0.052	-0.26%	-0.049	-0.25%	-0.06	-0.30%	-0.062	-0.31%
		III	-0.085	-0.43%	-0.08	-0.40%	-0.06	-0.30%	-0.079	-0.40%
		IV	-0.116	-0.58%	-0.11	-0.55%	-0.11	-0.57%	-0.129	-0.65%
		PPS	P1		P2		P3		P4	
			(mm)	%	(mm)	%	(mm)	%	(mm)	%
	S1	I	-0.027	-0.27%	-0.041	-0.41%	-0.057	-0.57%	-0.033	-0.33%
		II	-0.042	-0.42%	-0.048	-0.48%	-0.057	-0.57%	-0.04	-0.40%
		III	-0.072	-0.72%	-0.089	-0.89%	-0.08	-0.80%	-0.09	-0.90%
		IV	-0.11	-1.10%	-0.111	-1.11%	-0.116	-1.16%	-0.09	-0.90%

Tableau 3A.4 3D profile mean deviations of Shape B artifacts at each post-processing steps (as-built I, after stress relief II, after part removal III, and after shot peening IV).

		PPS	P0-1	P0-2	P4-1	P4-2
B ⌓ μ (mm)	S3	I	-0.052	-0.044	-0.038	-0.041
		II	-0.053	-0.055	-0.015	-0.018
		III	-0.045	-0.041	-0.025	-0.028
		IV	-0.054	-0.05	-0.035	-0.03

	PPS	P4
S2	I	-0.026
	II	-0.002
	III	-0.024
	IV	-0.027

	PPS	P4
S1	I	-0.039
	II	-0.021
	III	-0.016
	IV	-0.032

CHAPITRE 4

GEOMETRIC DEVIATIONS OF LASER POWDER BED FUSED ALSI10MG COMPONENTS: NUMERICAL PREDICTIONS VERSUS EXPERIMENTAL MEASUREMENTS

Floriane Zongo[1], Charles Simoneau[2], Anatolie Timercan[1], Antoine Tahan[1], Vladimir Brailovski[1*]

[1] Department of Mechanical Engineering, École de technologie supérieure, Montreal, QC H3C 1K3 CAN
[2]SimuTech Group, CAN
* corresponding author
Submission: 1 November 2019 to Journal of Advanced Manufacturing Technology

Abstract: Laser Powder Bed Fusion (LPBF) is one of the most potent additive manufacturing processes. One of the constraints for a broader industrial use of this process is the limited knowledge of its dimensional performances and geometrical behavior, as well as the inability to predict them as a function of material, process parameters, part size and geometry. The objective of this study is to enrich knowledge of the geometrical and dimensional tolerancing (GD&T) performances of the LPBF process and to evaluate the distortion prediction capabilities of the ANSYS Additive Print software. To this end, a selected topologically-optimized part with three different support configurations was manufactured using an EOSINT M280 printer and AlSi10Mg powder. After printing, the parts were scanned using a coordinate measuring machine (CMM) and a computed tomography (μ-CT) system. The GD&T calculations were carried out according to the ASME Y14.5 (2009) standard. The distortions measured by the CMM and μ-CT techniques were 0.195 and 0.368 mm, respectively (95% interval). After the software calibration and two numerical sensitivity studies, the same STL files used to print the parts were downloaded into the ANSYS Additive Print software to calculate distortions caused by the process. The differences between the experimentally measured and the ANSYS predicted distortions for a 56 x 58 x 137 mm part fell within a 0.134 mm range at a 95% interval. The fidelity of the numerical predictions, the impact of the support structures and the

differences induced by the CMM and μ-CT measurement uncertainties are presented and discussed.

Keywords: Laser Powder Bed Fusion; Geometrical Deviations; Numerical Predictions; Predictions Capabilities

4.1 Introduction

Additive manufacturing (AM) technologies produce 3D engineered parts from nominal CAD files in an additive manner, generally layer by layer. The general principles of AM are described in ISO/ASTM52901-16 [1] and AM terminology is provided in ISO/ASTM 52900:2015 [2]. One of these technologies, laser powder bed fusion (LPBF), has become a key AM process, currently adopted by high technology industries, such as aerospace and automotive. However, the high cooling speed and temperature heterogeneity inherent to the process generate residual stresses responsible for distortions of LPBF parts, making their geometrical and dimensional tolerancing (GD&T) difficult to predict, which hinders a broader industrial use of LPBF parts.

Over the last decade, the simulation of the LPBF process has attracted a great deal of interest [91] as it can be used to address many of the challenges inherent to this technology. These challenges include the need to compensate for part distortions and shrinkage [92], dealing with residual stresses [93], avoiding building failures and blade crashes [94], selecting adequate printing directions [95], and generating support structures [96].

Simulation of the LPBF process is, however, a demanding task since it involves transient and multiphysics phenomena occurring at different scale lengths. The resulting models are highly complex, and require a massive amount of computing resources in order to be solved within a reasonable computing time. For these simulations to be practically feasible, some assumptions and simplifications are required, and the validity of their application depends on the simulation objectives (prediction of part distortions, melt pool dimensions, material microstructure, etc.) [97].

For example, the Project Pan finite element modeling software was used by Dunbar et al [98] to predict distortions of two Inconel 718 LPBF parts with only 12% difference between the results of post-build distortion simulations and the experimental measurements. Next, Mukherjee et al. [66] calculated transient temperature fields in LPBF parts and successfully compared the experimentally measured distortions of Ti-6Al-4V and Inconel 718 parts with their numerical predictions. Mercelis and Kruth [99] used a thermomechanical model to investigate the evolution of residual stresses in stainless steel (316L) LPBF parts and concluded that the most important parameters determining the magnitude and distribution of residual stresses are the material properties, the part and substrate heights, the laser scanning strategy, and the heating conditions. Denlinger et Al. [100] used a non-linear thermoelastoplastic finite element model, combined with an element coarsening strategy, in order to simulate the thermal and mechanical responses of a significant volume of deposited material. After testing the model with the in situ-measured distortions of Inconel 718 parts, they quantified the error of numerical prediction to only 5%.

Despite the great progress in LPBF process modeling achieved in the last few years, the tools that have been developed are still not accessible to the majority of LPBF users. Fortunately, a few commercial LPBF simulation platforms are emerging with the objective of helping LPBF users strengthen their understanding of the process and assisting them in the design of AM components. Among such commercially available simulation tools, ANSYS has recently come up with Additive Print, a tool which François, Segonds et al. [101] already used to assess the printability of their part by predicting the potential distortions that would occur during printing. However, to the best of our knowledge, no experimental validation studies, especially following the ASME Y14.5 [67] standard, have yet been published. To start filling this gap, the present study aims to experimentally validate the distortion prediction capability of ANSYS Additive Print, according to the ISO 22514-4 [102] standard. In this context, the methodological approach is presented in Section 2 along with a brief description of the software and details of the modeling and metrological measurements' strategies. Then, Sections 3, 4 and 5 present the results of this study and provide their interpretation.

4.2 Methodology

The methodological approach used in this project is divided into three steps: ANSYS Additive Print (AP) software calibration, a sensitivity study of the AP software, and a case study of the AP distortion prediction capabilities.

4.2.1 ANSYS Additive Print Software

By simulating the LPBF process, the ANSYS Additive Print software (ANSYS, Canonsburg, PA, USA) allows prediction of layer-by-layer distortions and residual stresses in a part. Additional features available in the software include the auto-generation of stress-based supports structures, the detection of potential recoater blade crash events, the identification of high-strain areas, and the auto-generation of distortion-compensated geometries. While a summarized description of Additive Print (AP) is presented here, more details can be found in the user's guide (ANSYS Additive User Guide, 2018 [103]).

The modeling approach used in this software is based on the inherent strain method, which originates from the welding process simulations, where the residual plastic strains (or inherent strains) are predicted in a structure that undergoes the welding thermal cycle[104, 105]. Three types of simulation (called strain modes) are available in the software (Assumed Uniform Strain, Scan Pattern and Thermal Strain), with three different approaches to calculate inherent strains. Figure 4.1-1 presents the differences between each strain mode with a schematic representation of the voxel inherent strain amplitude using a color scale.

In the Assumed Uniform Strain mode, a strain value is uniformly applied to every voxel of the same layer, and to each layer of the part. In the Scan Pattern strain mode, an anisotropic strain value based on the actual scan orientation of the machine is uniformly applied to every voxel of the same layer. Finally, in the Thermal Strain mode, thermal simulation first predicts the strain at each point of the part, based on the actual scanning strategy of the machine. These location-specific strain values are next applied to each voxel as anisotropic strain values values [103].

The Assumed Strain mode is the fastest option available, which makes it suitable for an initial insight, while the Scan Pattern and Thermal Strain modes require longer computing times and

more data input, but generally lead to more accurate predictions. Two stress modes (Linear Elastic and Elastoplastic) are also available, with similar trade-offs (i.e., simulation accuracy vs solving time).

On the geometry side, the part to simulate must be oriented along the desired printing direction (Z-axis) and converted into an STL format. The meshing method is based on voxelization, where the size of a voxel should be at least one-fourth (¼) the minimum feature dimension and/or determined through a mesh sensitivity study. Therefore, it is assumed that multiple physical layers are embedded within one voxel layer. Figure 4.1-2 depicts the meshing workflow.

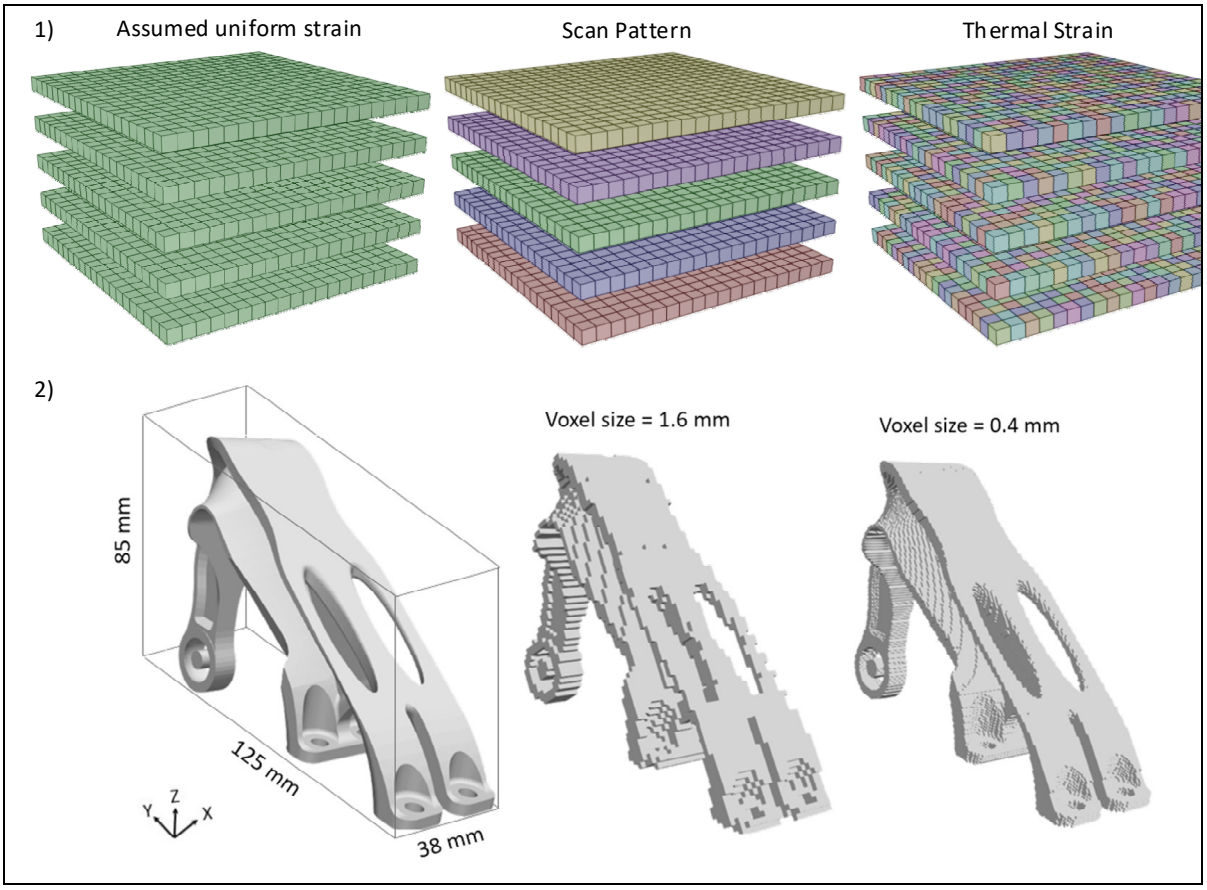

Figure 4.1 Different inherent strain calculation modes; 2 (a) Triangulated surface representation of the part (STL) with the Z-axis corresponding to the build direction (adapted from ANSYS [103]); (b, c) voxel-based mesh with different voxel sizes

To provide representative results, inputs about the scanning strategy of a given LPBF system (layer thickness, starting layer angle, layer rotation angle, etc.), the mechanical properties of the material to be processed (Young's modulus E, Poisson's ratio ν, yield strength YS, etc.), and the support structures features (minimum overhang angle and support yield strength ratio) are required. Details of all the requested inputs for each strain mode are summarized in Table A (Appendix 4A). Finally, calibration is required to improve accuracy of the inherent strain prediction for any material, system, and a strain-stress mode combination.

4.2.2 Software calibration

The calibration process consists in finding optimal values of some numerical coefficients, namely, the strain scaling factor (SSF) and the anisotropic strain coefficients (ASCs). The values of these coefficients need to be modified iteratively until the predicted distortions match those of the 3D-printed calibration artifacts (refer to the ANSYS Additive Print Calibration Guide (2018) [106] for detailed calibration procedure). As per the ANSYS Additive User Guide, SSF is a direct multiplier of the predicted inherent strain, which is given by the YS/E ratio. SSF values greater than 1 amplify displacements and stresses, while those that are less than 1 reduce them. ASCs correspond to three direct multipliers of the inherent strain, which are applied along the local longitudinal, transverse and depth scan directions to reflect the fact that more strain develops along the longitudinal scanning direction than in the transverse direction. A positive ASC results in compressive strains (contraction), whereas a negative ASC results in tensile strains (expansion). Note that the SSF coefficient needs to be calibrated for all strain modes, while the ASC coefficients are only required for the Scan Pattern and Thermal strain modes.

In this study, calibration was carried out by printing three geometrically identical cross-shaped artifacts using three different scan patterns (Figure 4.2). Calibration artifact #1 was printed using a bi-directional scan pattern along the X-axis, with a 0° starting angle and a 0° layer rotation angle. Calibration artifact #2 was printed using a rotating stripe scan pattern with a 57° starting angle and a 67° rotation angle. As recommended by the AP user's guide, Calibration artifacts #1 and #2 were printed without contouring, up-skin and down-skin.

Finally, Calibration artifact #3 was printed using the scanning strategy of a specific LPBF system (in the present work, this corresponds to the scanning strategy of an EOSINT M280/290 LPBF system). The in-plane distortions of the calibration artifacts were measured at locations where they are deemed to be maximum (Z = 22 mm, Figure 4.2-1). Tableau 4.1 summarizes the process parameters used for the Scan Pattern strain mode simulations with all three calibration artifacts.

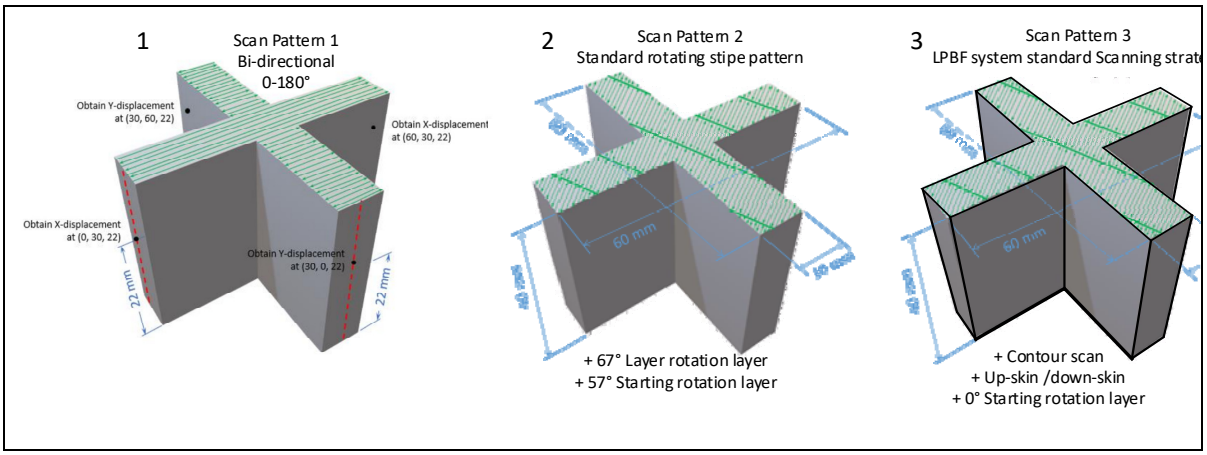

Figure 4.2 Calibration artifacts: #1 with a bi-directional scan pattern and distortion measurement locations; #2 with the standard rotating stripe pattern and part dimensions; #3 with the rotating stripe pattern and contouring (LPBF standard scanning strategy); adapted from ANSYS [106]

Tableau 4.1 LPBF process parameters required for the Scan Pattern strain mode

Process parameters	Calibration artifacts		
	#1	#2	#3*
Layer thickness	30 µm	30 µm	30 µm
Starting rotation layer	0°	57°	0°
Layer rotation layer	0°	67°	67°
Contour scan	no	no	yes
Up-skin /down-skin	no	no	yes
* Specific to EOSINT M280/290			

The following three-step procedure was used to calibrate the ASCs and SSF values:

1. A first series of simulations were carried out on Calibration artifact #1. Due to its bi-directional scanning strategy, anisotropic distortions along the X- and Y-axes are expected. These unequal distortions were used to determine the longitudinal and transverse ASCs. A value of 1 was assumed for the depth ASC (the ASC between each layer in the Z direction) as recommended by (ANSYS Additive User Guide, 2018 [103]). An initial value for the SSF was also found.
2. A second series of simulations were carried out on Calibration artifact #2. Due to its layer-by-layer rotating scanning strategy, isotropic distortions along the X and Y axes were expected. The quasi-equal distortions were used to determine the final value of SSF. The ASC values remain unchanged.
3. A third series of simulations were carried out on Calibration artifact #3. Since this artifact was manufactured using the real process parameters with contouring, upskin and downskin, the obtained distortions were used to fine tune the SSF value for the next sensitivity study.

In this work, only the Assumed Strain and Scan Pattern modes were calibrated because the Thermal Strain mode was not yet available for the material used in this study. The calibration was made on the 2019 R2 1.5.3 version.

4.2.3 Software sensitivity study

After the calibration, a software sensitivity study was conducted to test the different modeling assumptions of the software and to gain a preliminary understanding of the process-induced distortions due to the material concentration effect. In topology optimization, the material concentration or “pseudo-density” factor describes the layout of the material in a part within a given design space [107].

The sensitivity study was carried out in two steps. The first step consisted in the comparison of distortions for two simple part geometries (artifacts): a stepped cylinder (Shape A) and a hollowed cylinder (Shape B-P2), presented in the first row of Figure 4.3 using different combinations of the strain and stress modes (the software needs to be calibrated for each mode

combination). The STL files of these artifacts were loaded in ANSYS Additive Print, and four simulations were carried out for each of the two parts (AS LE, AS J2P, SP LE and SP J2P) as in Figure 4.3, where:

(1) AS LE corresponds to Assumed Strain simulation with Linear Elastic stress mode;

(2) AS J2P, to Assumed Strain simulation with Elastoplastic stress mode;

(3) SP LE, to Scan Pattern simulation with Linear Elastic stress mode;

(4) SP J2P, to Scan Pattern simulation with Elastoplastic stress mode.

A specific combination of the strain and stress modes, which most closely approximates the simulated results to the experimentally measured distortions, can now be identified and used in the next simulations. Note that all simulations were realized with a 0.25 mm voxel size determined during a distortion-based mesh sensitivity study using a convergence criterion of 2%.

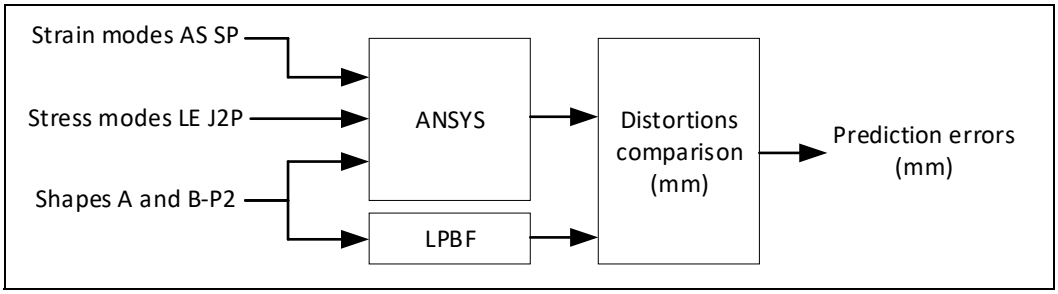

Figure 4.3 First step of the sensitivity study

The second step consisted in the comparison of distortions of four artifacts using the best combination of the strain and stress modes identified from the previous study (Section 2.3.1) was used here to predict the as-built part distortions. The artifacts' geometries are illustrated in the second row of Figure 4.4 and are referred to as the Shape B artifacts with a coaxial cylindrical pocket having a diameter of a half of a full cylinder. The variable between different Shape B artifacts is the pocket depth, ranging from one-fourth of the artifact height (P1) to a completely hollow cylinder (P4).

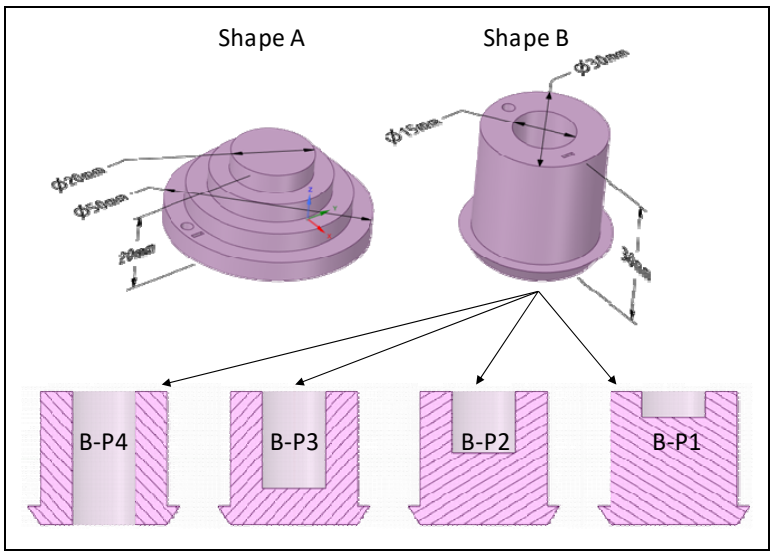

Figure 4.4 Sensitivity study artifacts. On top: strain and stress modes artifacts (Shape A – stepped cylinder); below: material concentration effect artifacts (Shape B – hollowed cylinder)

4.2.4 Case study

After the software calibration and sensitivity studies, a case study of the AP distortion prediction capabilities is conducted using a complex part, whose geometry was selected and designed according to the following recommendations:

- Avoid geometries which could be produced using conventional subtractive or formative manufacturing techniques;
- Include geometrical features which would amplify part distortions, such as sudden cross-section variations along the printing direction;
- Avoid internal cavities that cannot be measured using a coordinate measurement machine (CMM);
- Avoid small geometrical features that would require a very detailed/fine mesh, and thus increase the computing time;
- Present geometries that have the potential to be used in mechanical systems.

The part used for this case study is the control arm link designed for a solar powered vehicle Eclipse X, a scientific club at École de technologie supérieure (Montreal, Canada). To design this part, a topological optimization was carried out first, after which the part was prepared for printing using a specialized software application (Magics v.17.02, Materialise, Leuven, Belgium). The part was printed with three different support structure configurations. The first configuration was limited to supports at the base of the part and inside two holes at its top (Artifact 1), the second configuration included support structures for all overhang areas having an angle below 45° in respect to the build plate (block, gusset and line support structures were used in the latter case), while the third configuration was identical to the first, aside a full-density disk as pedestal at the base (Figure 4.5).

Note that the main objective of using Artifacts 1 and 2 was to assess the impact of the different support structure configurations on calculated and experimentally measured distortions. The objective of printing Artifact 3, which differs from Artifact 1 only by the presence of a disk at its base, was to decrease the risk of part distortions when removed from the building plate. This removal was necessary for micro-computed tomography observations (see Section 2.6.6.2 for explanations).

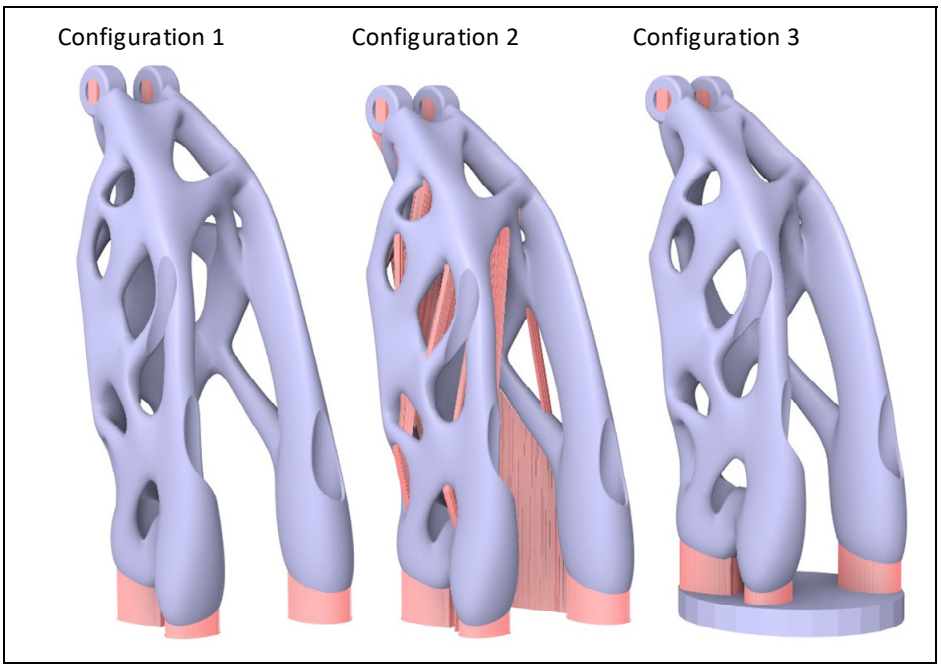

Figure 4.5 Case study part with different support structure configurations: Artifacts 1, 2 and 3

Distortions of the case study parts were computed for the 1st and 2nd support configurations using the best combination of the strain and stress modes identified from the previous study (Section 2.3.1). The case study analysis was realized with a 0.75 mm voxel size determined during a distortion-based mesh sensitivity study using a convergence criterion of 2%. An additional parameter, called the Support Yield Strength Ratio (SYSR), was used in the simulations to modify both the yield strength and the elastic modulus of the support material. The default SYSR value suggested by ANSYS is 0.4375. This value was determined in studies in which the strength of the default supports built on an EOS M270 machine was tested and compared to that of a dense material built on the same machine [103].

The results of simulations allowing the calculations of numerical distortions are referred to as AP-predicted distortions in the next sections.

4.2.5 3D-printing: Material and system

In the framework of this study, all parts were produced using an EOSINT M 280 400 W Ytterbium fiber laser system (EOS GmbH, Munich, Germany) and EOS AlSi10Mg powder with a particle size distribution of D10 = 12.8 µm, D50 = 27.7 µm and D90 = 51.3 µm; a tap density of 1.358 g/cm^3; an apparent density of 1.081 g/cm^3, and a Hausner ratio of 1.256 [22]. The parts were manufactured using the AlSi10Mg_Speed 103 process parameter set: a laser power of 370 W; a scanning speed of 1300 mm/s; a hatching space of 0.19 mm, and a layer thickness of 30 µm. No stress relief heat treatment was carried out on the parts, since this study focuses on the assessment of as-built distortions only.

For simulations, the following properties were either directly taken or calculated from the material data sheet provided by EOS [68] (EOS AlSi10Mg powder): the as-built in-plane Young's modulus, Yield Strength, Ultimate Strength and Elongation at Break, and Strain Hardening Factor (Tableau 4.2). The Poisson's ratio was taken from Matweb site [108].

Tableau 4.2 As-built in-plane mechanical properties of AlSi10Mg alloy processed by an EOSINT M280

Material properties	Value
Young's modulus, E	75 GPa
Poisson's ratio, ν	0.33
Yield Strength, YS	270 MPa
Ultimate Strength, UTS	460 MPa
Elongation at break, EB	9 %
Strain Hardening Factor, k	0.0285

The Strain Hardening Factor k was calculated as follows: $= \frac{Ep}{E+Ep}$, where $Ep = \frac{UTS-YS}{EB}$ is the plastic modulus.

4.2.6 Processing-induced deviations: numerical predictions versus experimental measurements

4.2.6.1 Calibration and sensitivity study

After the parts were printed, a thin layer of talcum powder was used to reduce part surface reflection. In doing so, the potential point cloud density was increased to ensure the best measurement. CMM scans of the entire build plate (with no post-processing treatment of the parts) were then carried out. In-plane distortions were measured on each of the calibration artifacts. Figure 4.6-a presents the calibration and the sensitivity study artifacts lying on the build plate, and Figure 4.6-b presents an example of the CMM-measured distortions. Point clouds of all the printed parts were obtained using a Metris LC50 laser scan mounted on a Mitutoyo CMM (accuracy $\leq \pm 7.5$ µm at 95% confidence level). Distortion measurements were carried out using a metrological software certified by the National Metrology Institute of Germany (PTB) PolyWorks® v.11 (Innovmetric, Quebec, Canada), and point cloud post-processing, using statistical analysis software Matlab® 2017b (MathWorks, Natick, MA, USA) and Minitab® v.17 (statistical software of Minitab Inc., State College, PA, USA).

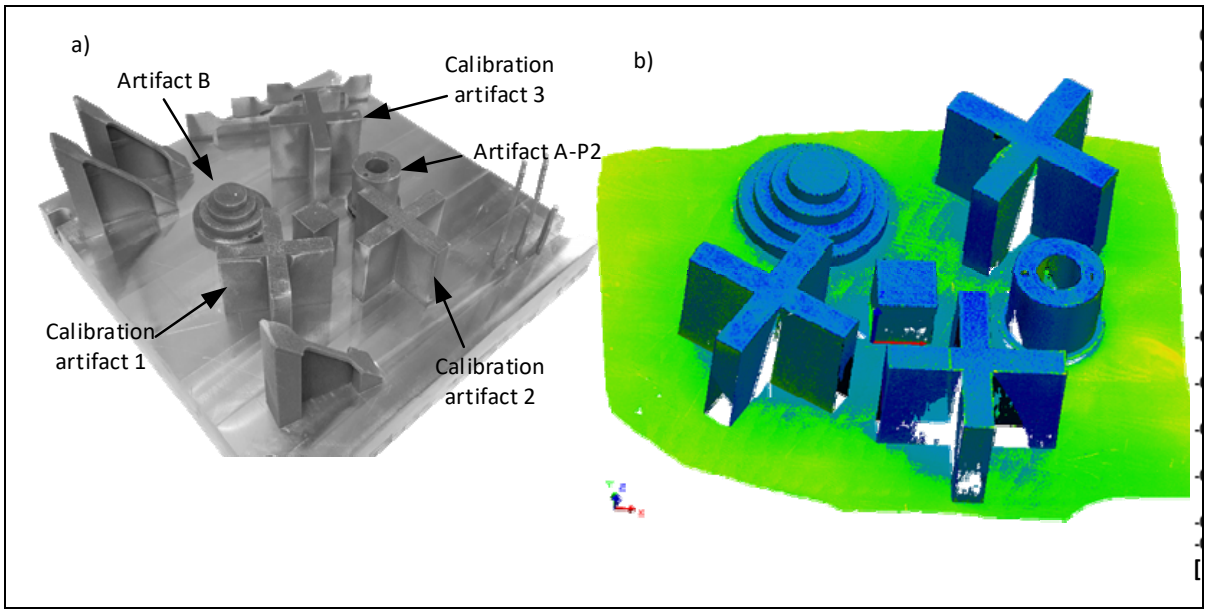

Figure 4.6 Calibration and sensitivity study artifacts: a) printed plate and b) example of the CMM-measured distortions (mm)

After the CMM measurements, the point clouds were post-treated using PolyWorks® v.11 and the numerical-experimental comparisons were carried out on distortions measured along the X- and Y-axes at multiple height locations on the calibration artifacts. For the sensitivity studies, the external diameters' deviations were extracted from the experimental point clouds and compared to the AP predictions. The Root Mean Squared Error was used to quantify the difference between the software predictions and the experimental results as in equation (4.1):

$$\mathrm{RMSE} = \sqrt{\frac{1}{N}\sum_{i=1}^{N}(AP_i - Exp_i)^2} \tag{4.1}$$

with N being the number of measured features (diameters in this case), AP_i, the ANSYS Additive Print distortion prediction at a location i, and Exp_i, the experimental distortion at the same location.

4.2.6.2 Case study

1) CMM analysis of the prediction accuracy (configurations 1 and 2)

After the parts were printed, CMM scans were carried out on the entire plate using the same scanning protocol as described in Section 2.6.1. The overall 3D profile deviation study was carried out on the cleaned CMM-obtained point clouds. For this study, the experimental point clouds were compared to the original STL files using the least squares best-fit technique. This analysis allowed observing the distortions on the manufactured parts. The results of this study are referred to as experimental distortions in the next sections. Figure 4.7-a presents the case study artifacts lying on the build plate, while Figure 4.7-b gives an example of the experimental point cloud best-fitted to the CAD of the plate.

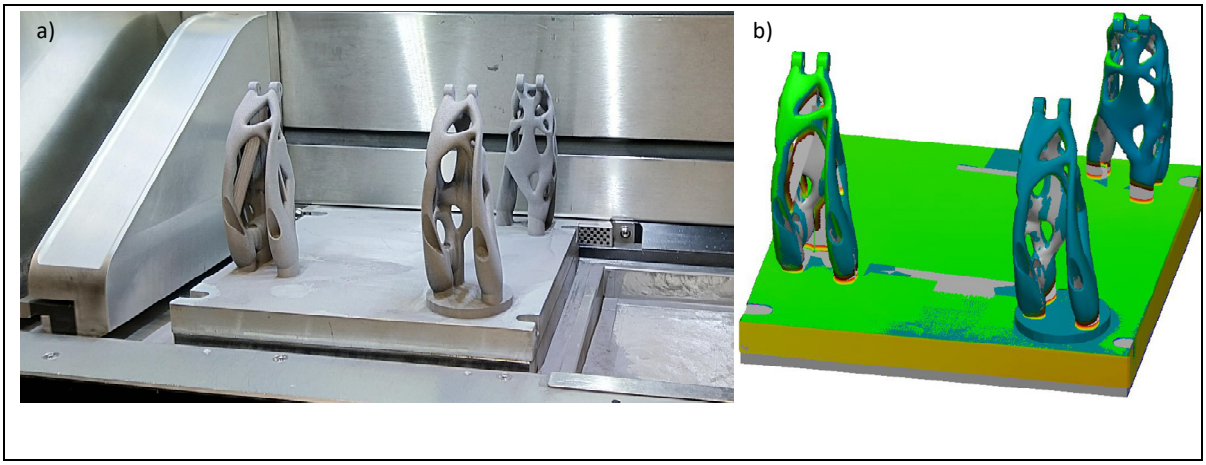

Figure 4.7 Case study: a) printed plate with the case study Artifacts 1, 2, 3, and b) example of the CMM-measured distortions

For a better appreciation of the differences between the experimental distortions and the AP predictions, a least squares best-fit operation were performed between the scanned point cloud and the AP predicted distorted STL files. These results are referred to as experimental vs predicted distortions comparison in the next sections.

2) µ-CT distortion analysis and comparison with the CMM-measured equivalent (configuration 3)

In order to select a digitization system on the basis of its suitability and versatility for experimental distortion measurements, distortions of the case study Artifact 3 were also measured using a Nikon XT H 225 X-ray µ-CT (computed tomography) system (Nikon, Brighton, MI, USA), once it was detached from the building plate and compared to their CMM-detected equivalents (for consistency, the latter measurements were also performed on Artifact 3 removed from the build plate).

The CT scan was performed with a reflection target configured with a 205 kV tube voltage and 50 µA current. The volume was then reconstructed using the CT Pro 3D software (Nikon, Brighton, MI, USA). Due to its height, the part was scanned in two acquisition windows and assembled after the reconstruction to get the entire part. Note that despite the segmentation quality and the software accuracy, there are some limitations in the default detection, inherent to the voxel size. Since a voxel has only one intensity, the 52x52x52 µm volume contains only one piece of information. When the voxel is at a void/material border, there is an error induced

by its size (Figure 4.8). An STL was reconstructed using the segmented part and compared to the CAD, in order to extract the overall 3D profile deviation detected by the µ-CT.

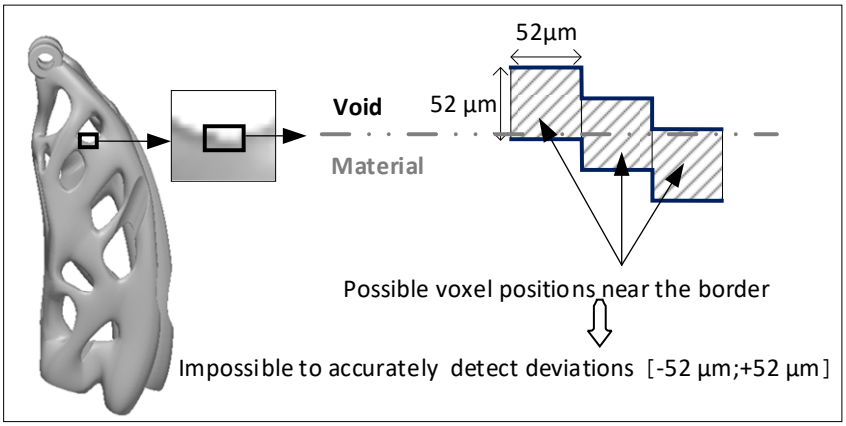

Figure 4.8 Void/material border position error inherent to the voxel size

Figure 4.9 presents a setup used to scan the case study part, along with a scan 3D rendering. The obtained scan is presented as a series of voxels having different grayscales. A threshold is applied in the Dragonfly V2 software (Object Research Systems, Montreal, Canada) environment to separate the region of interest (ROI) which is the part here, from the void. The voxels whose intensity values are greater than the threshold, are classified as being the part, and their intensity is changed to a value of 1, while the rest of the voxels are classified as voids, and their intensity changed to a value of 0. The scan segmentation was carried out using the CMM measured local thickness as calibrating values to choose the best grayscale for the material/void threshold. Note that this specific measurement was performed using the CMM mounted by a PH10 / TP20 probe (uncertainty ≈6 µm), unlike the rest of the CMM measurements that were performed using the CMM mounted by a Metris LC50 laser scan (uncertainty ±7.5 µm). The next step after segmentation was the segmented ROI analysis using Polyworks.

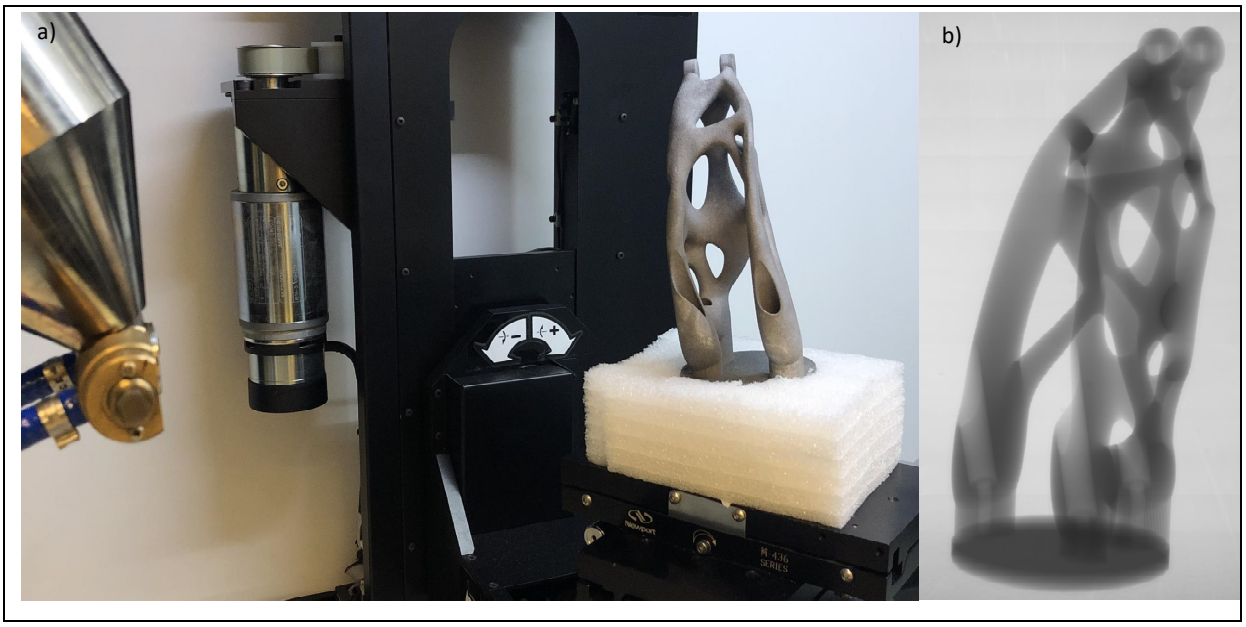

Figure 4.9 Case study Artifact 3: a) setup on a Nikon XT H 225 X-ray µ-CT system and b) 3D rendering

4.3 Results

As per ASME Y14. 5.1 [67], profile deviations can extend in two directions: material withdrawal (shrinkage), when the feature is smaller than the nominal size in the direction of the least material condition (LMC), and material addition (growth), when the feature is bigger than the nominal size in the direction of the maximum material condition (MMC).

4.3.1 Software calibration

While the lowest shrinkage (LMC direction) was obtained at extremum Z coordinates, the highest shrinkage was obtained at a 22 mm height, as shown in Figure 4.10 for Calibration artifact #3. The calibration process relies exclusively on measurements taken at a single height location of the calibration artifacts (Z = 22 mm), as recommended in the ANSYS Additive Print Calibration Guide (2018).

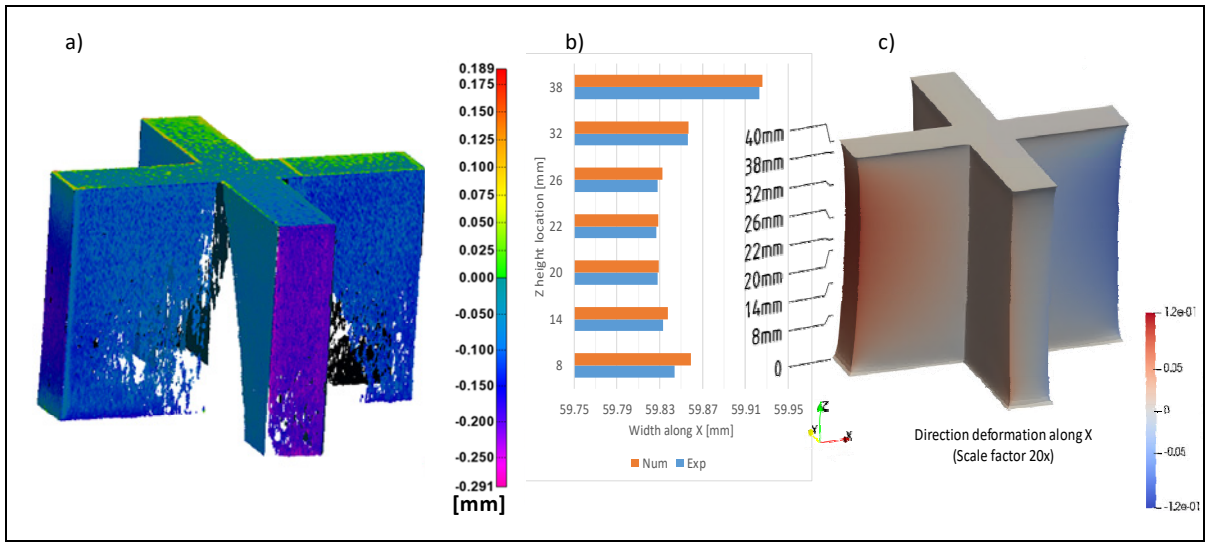

Figure 4.10 Calibration artifact#3 (EOS AlSi10Mg Performance scanning strategy) analysis: a) CMM measurements, b) numerical predictions-experimental measurements comparison, c) numerical simulations (mm)

Calibration results are summarized in Tableau 4.3 and Tableau 4.4 Following the first series of simulations (i.e., Calibration artifact #1 with the bi-directional scan pattern), appropriate values for the anisotropic strain coefficients (ASCs) and strain scaling factor (SSF) were found (Tableau 4.3). These values resulted in less than 1% deviations between the predicted and the measured distortions. The second series of simulations (i.e., Calibration artifact #2 with the rotating scan pattern) allowed the determination of a more accurate value for the SSF by keeping the same value of the ASCs. The third series of simulations (i.e., Calibration artifact #3) allowed the determination of final values for the SSF (Tableau 4.4) by keeping the same values of ASCs.

Tableau 4.3 Calibration results: anisotropic strain coefficients (ASCs)

Longitudinal ASC	Transverse ASC	Depth ASC
1.17	0.83	1

Tableau 4.4 Calibration results: strain scaling factor (SSF)

Strain mode	Stress mode	Strain scaling factor	Numerical/Experimental Error (%)
Assumed Strain	Linear Elastic	0.79	0.4
	Elastoplastic	0.7163	0.01
Scan Pattern	Linear Elastic	0.79	0.3
	Elastoplastic	0.7165	0.02

4.3.2 Software sensitivity study

4.3.2.1 Comparison of the strain and stress modes

Figure 4.11 presents distortions of the outer diameters of Artifact A taken at different Z-locations. The experimental deviations (blue) are compared to those obtained numerically using different simulations modes. The difference is quantified using the RMSE. It can be observed that the experimental deviations are directly proportional to the measured diameter, and the larger the nominal diameter, the greater the deviations. The AP, however, predicts a significantly different trend: as we go from the top of the part to the build plate, shrinkage increases and reaches its maximum at a distance of 7 mm from the build plate, and then starts decreasing. Globally, the Elastoplasticity (J2P) stress mode predicts greater shrinkage, and better approximates the experimental deviations. Concerning the RSME, there is a clear separation between the LE stress mode (AS LE and SP LE), which both present a 34 µm error, and the J2P stress mode (AS J2P and SP J2P), which both present a 28 µm error. These results will be interpreted further (see discussion section).

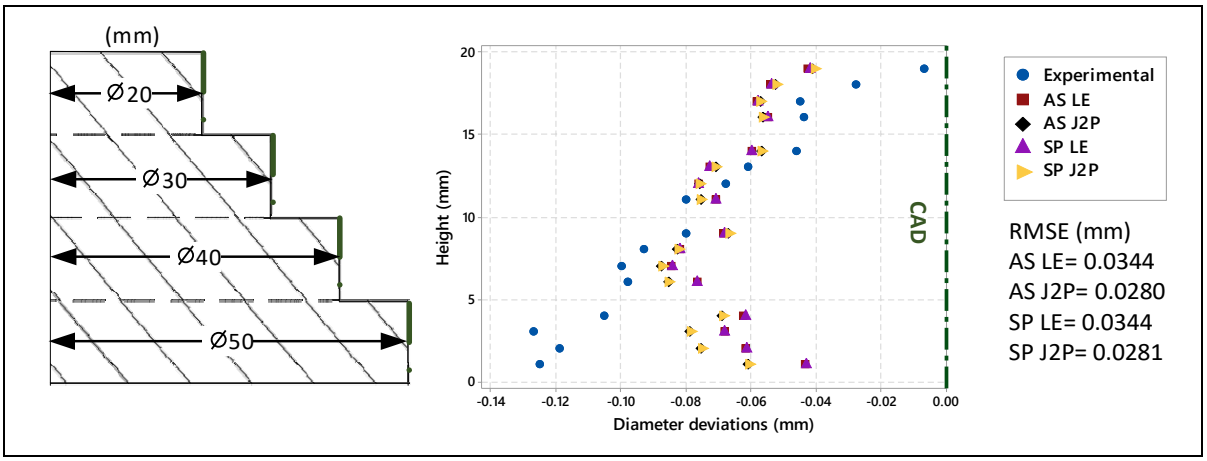

Figure 4.11 Application of the different combinations of stress-strain simulation modes on stepped cylinder (Shape A artifact)

Figure 4.12 presents distortion measurements of the outer diameter of the Shape B-P2 artifact taken at different Z-locations. The color code is the same as in Figure 4.11 The measured diameters (blue) are compared to those obtained numerically. Globally, the pocket (blind hole) creates a step in the outer diameter distortion, and this trend is predicted by each of the numerical results. Despite a slight underestimation, the predicted results are in line with the measurements. At 30-15 cm of height, the prediction error is uniform, which means there is almost no difference between the results provided by the AS and SP strain and LE and J2P stress modes. As observed in the measurements of the previous artifact, when we get closer to the build plate, there appears to be a stress mode separation. The Elastoplasticity (J2P) stress mode predicts greater shrinkage, and better approximates the experimental deviations. It is almost the same with the RMSE, with 16 µm for all the strain and stress modes, except for the AS strain mode-J2P stress mode combination, which corresponds to 15 µm RMSE and represents a 0.05% error.

Based on the above observations, the combination of the Assumed Strain mode (AS) with the-Elastoplastic stress mode (J2P) could be identified as approach presenting the smallest dissimilarity with the experimental distortions, and this strain-stress mode combination was used in the next simulations.

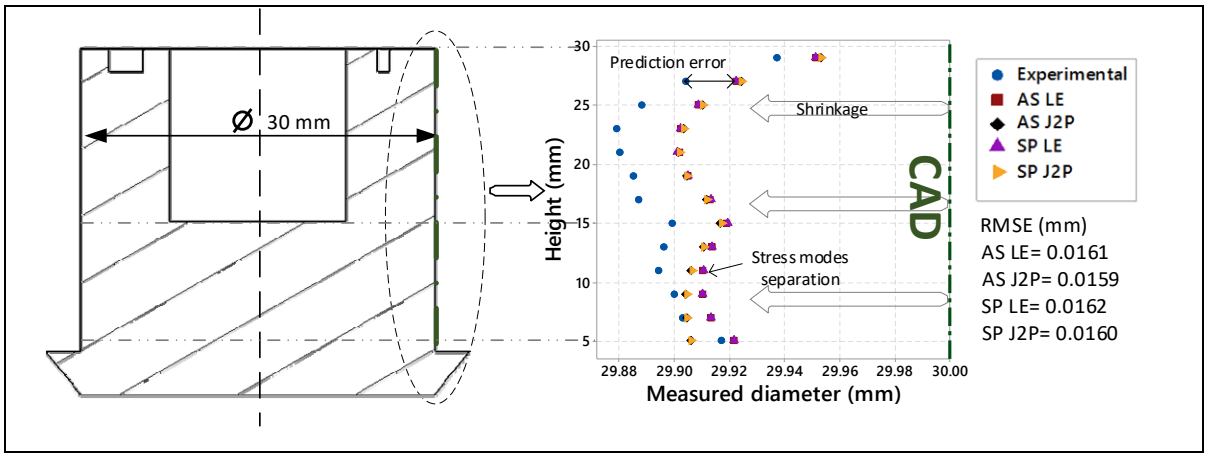

Figure 4.12 Simulation stress and strain modes difference study on hollowed cylinder (Shape B-P2 artifact)

4.3.2.2 Comparison of part geometries (material concentration effect)

The material concentration effect was investigated on the outer diameters of the Shapes B-P1 to P4 artifacts. Figure 4.13 presents the experimental (blue) and the AP predicted distortions (red) for each of the parts. The influence of the pocket (blind hole) depth is clearly observable on the outer diameter, as it gives a different trend to each of the graphs. AP simulations take into account this influence, and predict very similar trends in all situations (i.e. deviations are in the order of less than a fraction of a percentage). However, predicted deviations are larger in parts having a higher material concentration, illustrated here by a more shallow pocket (0.12% error for B-P1 artifact), than those having less material concentration (0.05% error for B-P2 artifact, 0.06% µm error for the B-P3 artifact, and only 0.01% error for the B-P4 artifact).

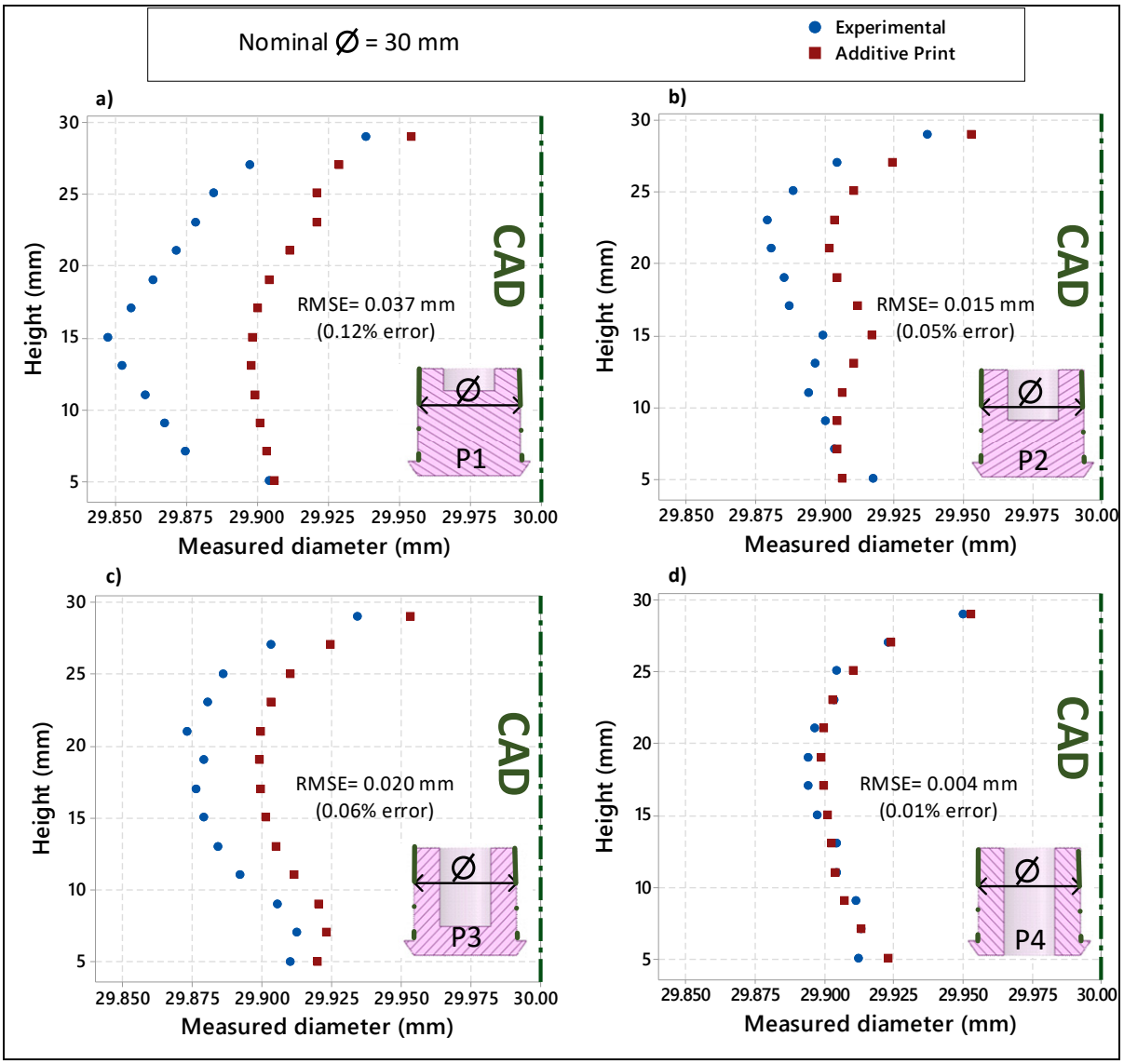

Figure 4.13 AP sensitivity investigation on different pocket depths: a) B-P1, b) B-P2, c) B-P3 and d) B-P4 artifacts experimental (blue) and predicted (red) distortions along Z axis.

4.3.3 Case study

4.3.3.1 Configurations 1 and 2 prediction accuracy analysis

The results of the case study allow several visual comparisons. Colors are used to distinguish the material withdrawals (LMC direction) from the material additions (MMC direction). Figure 4.14 and Figure 4.15 present the results of the case study Artifact 1 and 2 analyses respectively.

The experimental (1) and AP predicted distortions (2) are presented, along with the experimental point clouds and the AP distorted part best fits (3). The analysis of the predicted and experimental histograms highlights the fact that the predicted distortions appear to underestimate the effective values for both artifacts, but to different extents: for Artifact 1, in the -110 to -50 µm segment (Figure 4.14), while for Artifact 2, in the -150 to -60 µm segment (Figure 4.15). That means that the first configuration (Artifact 1, fewer support structures) was more accurately predicted by AP in the highly stressed areas than the second configuration (Artifact 2, more support structures). The non-parametric cumulative distribution function (NPCDF) graphs confirm this assertion. Note that the CMM used in this study has a 15 µm uncertainty interval at a 95% confidence level and this interval is plotted in the NPCDF of both parts (Figure 4.14 and Figure 4.15). As far as Artifact 1 is concerned, the AP predictions stay within the CMM uncertainty interval all along the NPCDF, while Artifact 2 predictions break out of the uncertainty interval in the -100 to -40 µm segment.

For complementarity, the AP prediction accuracies (experimental - prediction) for the case study Artifacts 1 and 2 are compared in Figure 4C.1 (Appendix 4C), the experimentally measured distortions, in Figure 4C.2 (Appendix 4C), and their numerical predictions, in Figure 4C. 3 (Appendix 4C).

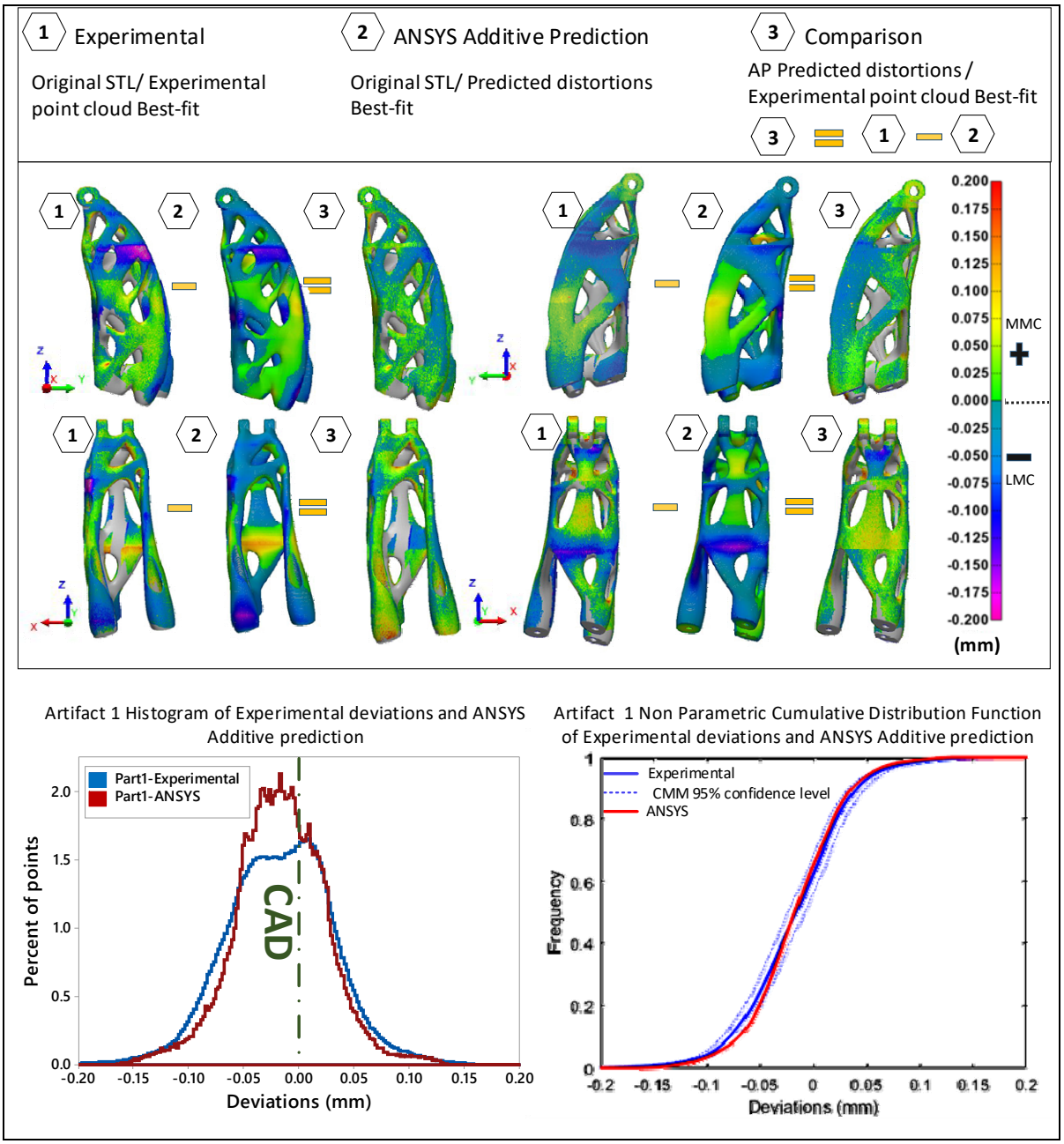

Figure 4.14 Complete analysis of the case study Artifact 1 (Support structure configuration I). Top: visual comparison with four different views of distortions; bottom left: Histogram, and bottom right: NPCDF of distortions

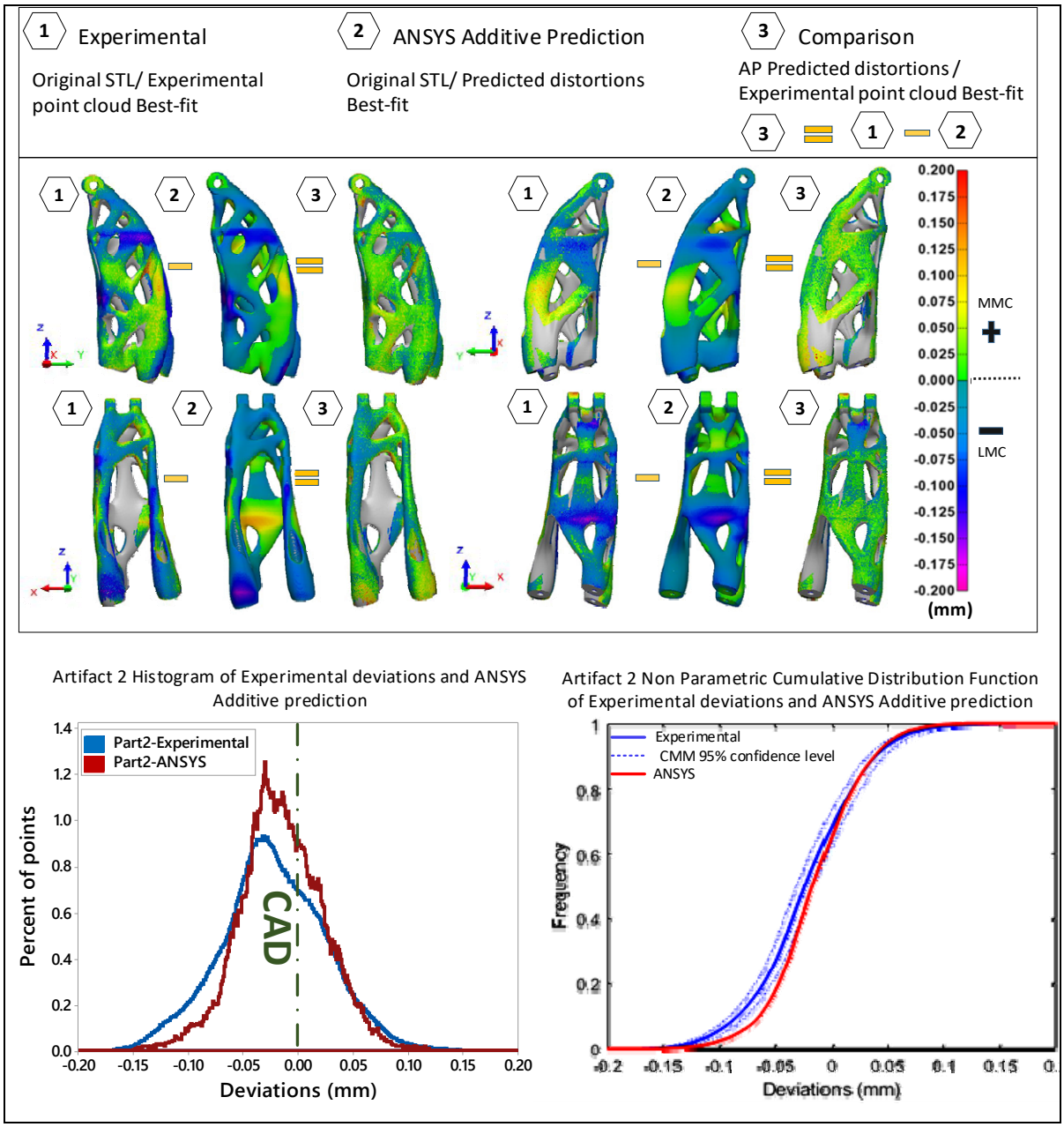

Figure 4.15 Complete analysis of the case study Artifact 2 (Support structure configuration II). Top: visual comparison with four different views of distortions; bottom left: Histogram, and bottom right: NPCDF of distortions

4.3.3.2 Comparison of the CMM and μ-CT distortion measurements

Figure 4.16 compares the CMM- and μ-CT- measured distortions (Artifact 3). As expected, the μ-CT detected distortion repartition presents a much larger spectrum, which means the detected deviations are higher in both the LMC and MMC directions.

Note that the deviations were measured after the part was removed from the build plate. An investigation was conducted on the part removal effect, and the results are presented in Appendix 4E.

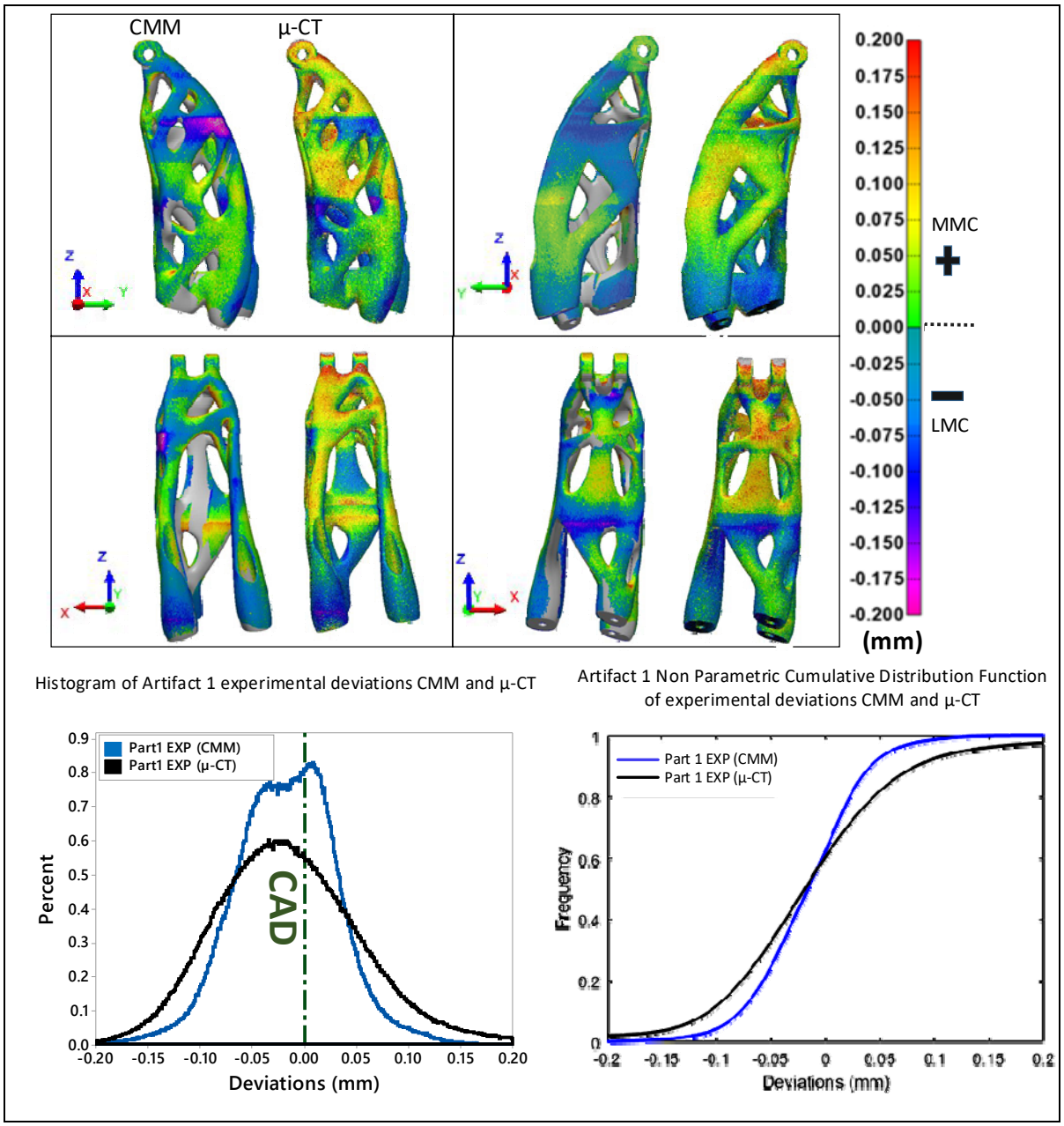

Figure 4.16 CMM vs µ-CT distortions of the case study Artifact 3. Top: visual comparison with four different views of distortions; bottom left: Histogram, and bottom right: NPCDF of distortions

4.4 Discussion

4.4.1 Software calibration

Calibration was used to configure the software for a given LPBF system and powder (i.e., an EOSINT M 280 400-Watt Ytterbium fiber laser system and EOS Aluminum AlSi10Mg powder).

In terms of input, when compared to the Scan Pattern strain mode, the Assumed Strain mode does not require any anisotropic strain coefficients (ASCs) and, therefore, any LPBF process parameters. Since the EOS scanning strategy is based on a 67° rotating scan pattern between each layer, part distortions are uniform and direction-independent. Therefore, for simple prismatic geometries, the contribution of the scanning strategy during the simulation using the Scan Pattern strain mode is almost negligible in terms of distortion prediction accuracy.

The two-step calibration process aims to determine the ASCs at the first step and then fine-tune the SSF at the second step. While it was shown that the ASC values have only a small impact on the results of this study, the key to accurately predicting part distortions is the SSF calibration. Therefore, if isotropic distortions are expected (due to the scanning strategy), one could simply use the Assumed Strain mode and calibrate the SSF using Calibration artifact 2 or 3.

4.4.2 Sensitivity study

4.4.2.1 Comparison of the strain and stress modes

The first sensitivity study was carried out to evaluate the impact of the selection of different combinations of the strain-stress modes.

A clear difference between the Linear Elastic and Elastoplastic stress modes can be observed. Indeed, as we get closer to the build plate, we can see a stress mode separation in both Shape A and Shape B-P2 artifacts, with the Elastoplastic mode predicting more shrinkage, and thus showing less error when compared with the experimental deviations than the Linear Elastic mode (Figure 4.11 andFigure 4.12). This discrepancy can be explained by the fact that in the

case of the LE stress mode, the distortions will be accurately predicted only for the voxels that are subjected to a stress lower than the yield strength, in the elastic zone of the material. The distortion of the voxels experiencing a local stress greater than the yield strength may be overestimated. Therefore, to gain a better accuracy of simulations, it is recommended to use the elastoplastic stress mode, despite a higher computation time.

On the other hand, neither mode takes into account element failure. Consequently, the voxels subjected to a local strain exceeding the elongation at break will be less accurately predicted. However, an investigation conducted on the stress distribution of Shape A and B-P2 artifacts for all four simulations types showed that only few elements reach a stress level higher than the ultimate strength with the Elastoplastic stress mode. The results are presented in Appendix 4B.

It can be noted in Figure 4.11 that while experimental deviations continually increase as we move from the top of the printed part to the build plate (with larger nominal diameters and greater experimental deviations), their predicted values increase, exceed their maximum (at a 7 mm height), and then decrease. This discrepancy can be attributed to one of the modeling assumptions used in AP software: to reduce the model complexity and save computation time, the build plate (and the associated degrees of freedom) was not included during the simulation. To circumvent the absence of the build plate, all degrees of freedom of the part and/or supports at Z = 0 mm were fixed (i.e. UX=UY=UZ=0 mm). In other words, the build plate compliance was not taken into account, thus affecting the distortion predictions near Z=0.

4.4.2.2 Material concentration effect

In this study, the Assumed Strain and the Elastoplastic stress modes were used to investigate the material concentration effect. A high material concentration was experimentally proven to be responsible for high thermal stresses and, therefore, for a greater part shrinkage. Indeed, the greater the material concentration (B-P1), the larger the zone with higher thermal stresses, and therefore, the greater the distortions. This study was carried out in a 30x30x30 mm design space, and a 30 mm diameter feature was investigated (Figure 4.13). Depending on the material concentration, we calculated a 0.12% error on the part having the highest material

concentration (B-P1), and 0.01% on the part having the smallest material concentration (B-P4). This study was carried out in a 30x30x30 mm design space, and a 30 mm diameter feature was investigated (Figure 4.12). Depending on the material concentration, we calculated a 0.12% error on the part having the highest material concentration (B-P1), and 0.01% on the part having the smallest material concentration (B-P4). Although, the predicted distortions seem to be influenced by the material concentration, the RMSEs calculated are similar to Shape A artifact RMSE (28 µm)

4.4.3 Case study

4.4.3.1 Configurations I and II prediction accuracy analysis

The statistical description of this study presented in Tableau 4.5 reveals an interesting fact. When we look at the experimental point cloud and the AP distorted part best fit (ANSYS-EXP variables), the prediction capability interval 99.73% as per ISO 22514-4 standard (which is q99.865- q0.135) is larger for the case study Artifact 2 (223 µm) than for the case study Artifact 1 (244 µm). Figure 4.17 and Appendix 4C show the prediction accuracy for the case study Artifacts 1 and 2. Note that since we are observing differences between the experimental and predicted distortion, the better the quality of prediction, the closer the histogram to zero (0.00) deviation. The statistical terms are explained in this introduction to statistical analysis textbook [109].

Tableau 4.5 Artifact 1 and 2 analysis statistical description (mm); $q_{x\%}$= quantile to $x\%$ probability

Artifact #	Variable	Mean	St Dev	$q_{25\%}$	$q_{50\%}$	$q_{75\%}$	95% interval	99.73% interval
1	EXP	-0.011	0.049	-0.043	-0.01	0.021	0.198	0.336
	ANSYS	-0.016	0.045	-0.043	-0.016	0.013	0.181	0.279
	ANSYS-EXP	0.002	0.033	-0.019	-0.0001	0.022	0.134	0.244
2	EXP	-0.022	0.048	-0.052	-0.023	0.010	0.194	0.3
	ANSYS	-0.014	0.042	-0.040	-0.016	0.011	0.166	0.264
	ANSYS-EXP	0.002	0.029	-0.016	0.001	0.018	0.118	0.223

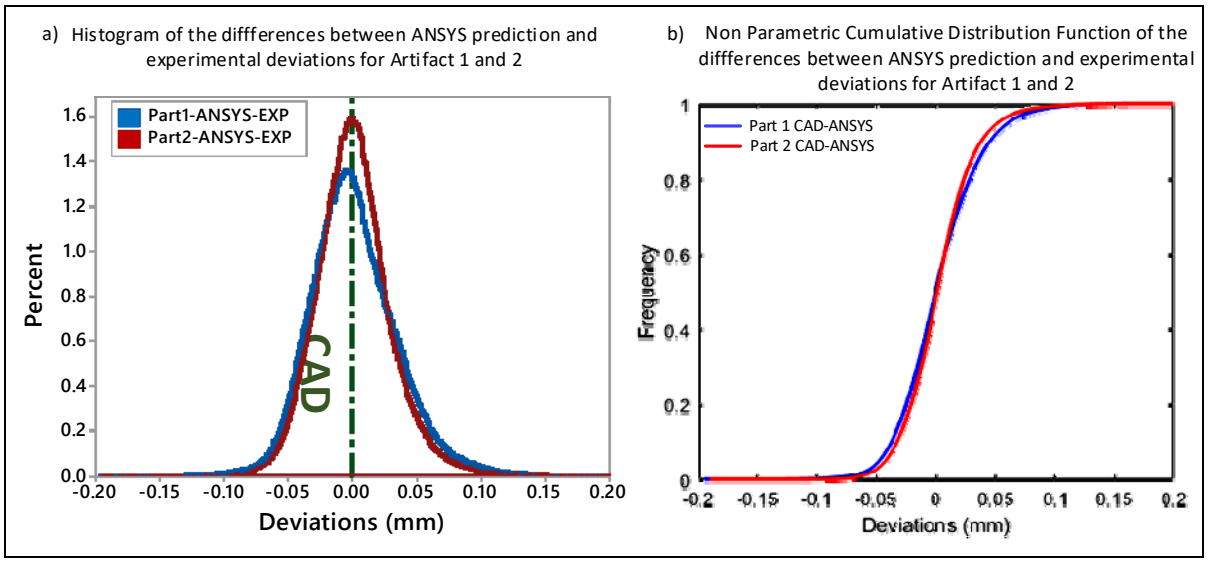

Figure 4.17 AP prediction accuracy for Artifacts 1 and 2: a) Histogram, b) NPCDF of distortions

4.4.3.2 Support structure effect analysis

A visual comparison of the support structure effect shows less shrinkage (LMC direction) in the highly distorted areas of the part with a larger quantity of support structures, Artifact 2 (Figure 4.18-a, Appendix 4C). This fact was fully taken into account by AP (Figure 4.18-b, Appendix 44C).

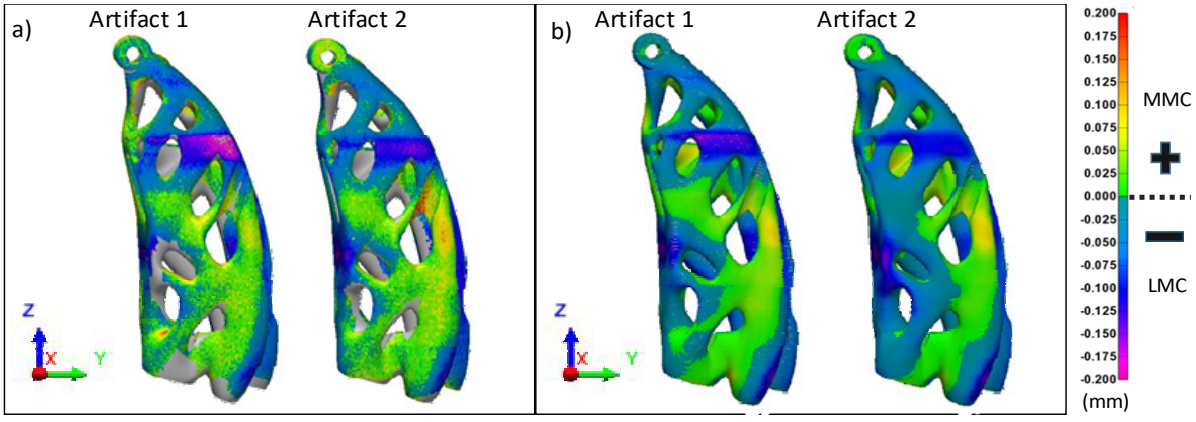

Figure 4.18 Visual comparison of one of the highly distorted areas for the case study Artifacts 1 and 2: a) CMM measurements, b) AP predictions

The experimental deviation histogram, however, shows that the case study Artifact 2 has more deviations in the -150 µm to -100 µm segment than the case study Artifact 1, which is confirmed by their NPCDFs (Figure 4.19, Appendix 4C). The statistical description shows a 11 µm difference in the two parts mean deviations, with Artifact 2 showing more shrinkage than Artifact 1.

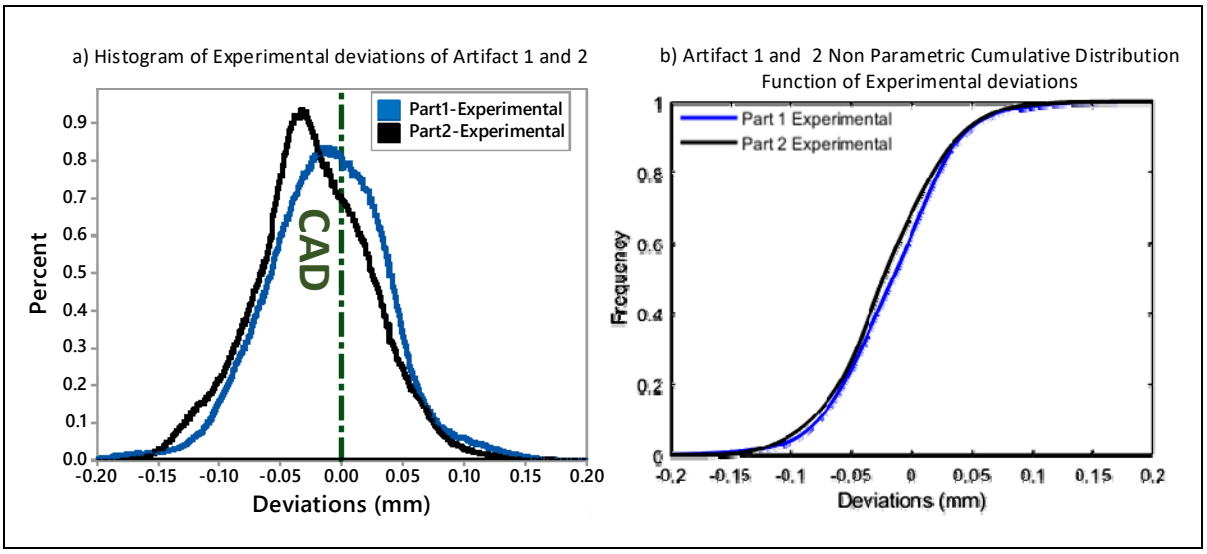

Figure 4.19 Configuration I and II CMM detected distortions: a) Histogram, b) NPCDF of the distortions

The pedestal effect was also investigated by comparing the case study Artifacts 1 and 3 experimental deviations (Appendix 4D). The differences detected lie in the CMM uncertainty interval (see Appendix 4D).

To sum-up the observations of the above case study, it appears that having a larger quantity of support structures reduces shrinkage in some highly-distorted areas of the part, while globally inducing more deviations. Note however that, as mentioned above, a default Support Yield Strength Ratio value suggested by ANSYS was used in the simulations to modify both the yield strength and the elastic modulus of the support material. It can be hypothesised that printing and testing the strength of supports structures with our specific LPBF system and powder would make our support-related distortion predictions more trustworthy.

4.4.3.3 µ-CT detected distortions analysis

A visual comparison of the CMM vs µ-CT distortion analyses (Figure 4.16) shows greater level of deviations in both the LMC and MMC directions for the latter technique, which is statistically manifested by a larger spectrum of the µ-CT deviation histogram. Indeed, CMM detected deviations 95% interval is 200 µm, while µ-CT detected deviations 95% interval is 368 µm (Tableau 4.6).

Tableau 4.6 CMM and µ-CT detected deviations statistical description (mm)

Artifact #	Variable	Mean	StDev	$q_{25\%}$	$q_{50\%}$	$q_{75\%}$	95% interval
3	CMM	-0.030	0.047	-0.058	-0.030	-0.001	0.200
	µ-CT	-0.023	0.326	-0.065	-0.018	0.031	0.368

This difference is caused by a systematic error directly induced by the voxel size. The same observation was made by Barbero and Ureta [110]. After comparing five digitization techniques, they concluded the µ-CT tomography technique provides an adequate accuracy for small pieces and low thicknesses (less than 60 mm, dependent upon the material), but their dimensional errors are much greater than with the optical such as the CMM systems. Indeed, as explained in Section 2), the CMM detects locations (precise XYZ position) while the µ-CT gives only one piece of information about the voxel size in a 52x52x52 µm volume (grey scale). Moreover, due to their different acquisition principles, the measured part surface roughness produce significant deviation between and µ-CT measurements results, as observed by [27]. These factors in turn limits the void-material edge detection accuracy by the µ-CT, while CMM acquisition system has only a 15 µm uncertainty at 95% confidence level. This explains the large differences in their detected deviations 95% intervals. 200 µm for the CMM, and 0.368 µm for the µ-CT, while their mean deviations are almost the same, -30 µm for the CMM and -23 µm for the µ-CT.

Furthermore, the µ-CT scan lasted 4 hours and 52 minutes for ±98 µm uncertainty, compared to the CMM acquisition, which lasted five days, but for only ±7.5 µm uncertainty.

The CMM measurements uncertainty is provided on its calibration reports, while the µ-CT uncertainty was estimated as per ISO/BIPM-GUM [111], by taking in account the calibrating method which is the CMM mounted by a PH10 / TP20 probe (uncertainty ≈6 µm), the uncertainty induced by the voxel size and the µ-CT uncertainty which is 17 µm. This last value was communicated to us by the µ-CT manufacturer as the measurement uncertainty on complex forms when the equipment is calibrated using known forms. However, in our case we calibrated the scan segmentation rather than the equipment.

However, the µ-CT gives information about the entire part, the outside (skin) and the inside, while CMM point cloud only gives partial information about the skin. The µ-CT entire post treatment lasted five hours, compared to CMM point cloud cleaning which lasted four hours, alignment and distortion detection which lasted two hours, and graphics generation which lasted two hours, for a total of eight hours.

4.5 Study limitations

As described, the thermal strain mode predicts strain at each point of the part, based on the actual scanning strategy of the machine. To predict more accurately the part distortions, these location-specific strain values must be applied to each voxel as anisotropic strain values. Unfortunately, at the moment of this study, this simulation mode was not yet available for aluminum alloys of this study.

In addition, as previously noted, we did not take into account the build plate and the associated degrees of freedom, thus affecting the behavior of simulated components at their connection with the build plate. While the case study artifacts with support structures were less disturbed by this effect, the sensitivity study artifacts built directly on the build plate were more strongly influenced.

Finally, the repeatability of the LPBF system has been demonstrated to be an important factor to be taken in account [84]. Printing and testing a larger number of the case study Artifacts would have allowed us to quantify the LPBF system repeatability error in this specific case.

4.6 Conclusion

This work was designed to study, quantify and validate the distortion prediction capabilities of the ANSYS Additive Print software. It presents and discusses the differences between the experimental 3D profile deviations of 10 AlSi10Mg printed parts and their AP predictions. Investigations are realized to quantify the software prediction accuracy, the effect of support structures on printed part distortions, and the differences between the experimental distortions detected on the same part by two measurement techniques, CMM and µ-CT. Based on the results obtained, the following conclusions can be drawn:

(1) Despite the longer acquisition and post treatment time, the CMM acquisition system is best suited for this study because of its high accuracy ($\leq \pm 7$ µm at 95% confidence level);
(2) In most of the cases, AP predicts a very similar trend in the distortion repartition as that observed experimentally;
(3) The assumed strain mode and the elastoplastic stress mode is the best combination to get accurate results without uselessly increasing computing time;
(4) For the case study artifacts with overall dimensions of 56 x 58 x 137 mm, AP globally underestimates the effective distortions up to a maximum of approximately 150 µm;
(5) Increasing the amount of support structures could globally induce more deviations, but reduce local deviations in high-strained areas of the part;
(6) The deviation repartition spectrums measured by the µ-CT and CMM techniques are not the same: they are larger for the former than for the latter, given its greater measurement uncertainty.

Acknowledgments: The authors would like to thank Natural Sciences and Engineering Research Council of Canada and École de technologie supérieure (ETS) for the financial support. The authors are thankful to Joel Grignon and Morgan Letenneur who assisted in the research.

Authors' Contributions: The project objectives and methodology were proposed by A.T. and V.B. The specimen fabrication, scanning and data treatment were carried out by F.Z. The numerical simulations were carried out by A.Ti. and C.S. The article was written by F.Z. and revised by C.S., A.Ti., A.T. and V.B.

Conflicts of Interest: The authors declare no conflicts of interest.

APPENDIX 4A

Tableau 4A.1 Summary of the inputs needed for each strain mode calculation (adapted from ANSYS Additive software)

Input type	Input parameter name	Units	Value used	Assumed uniform strain	Scan Pattern strain	Thermal Strain
Machine Configuration	Baseplate Temperature	°C	N/A	No	No	Yes
	Layer Thickness	µm	Tableau 4.1	No	Yes	Yes
	Starting Layer Angle	°		No	Yes	Yes
	Layer Rotation Angle	°		No	Yes	Yes
	Hatch Spacing	µm	N/A	No	No	Yes
	Slicing Stripe Width	mm	N/A	No	No	Yes
	Laser Power	W	N/A	No	No	Yes
	Scan Speed	mm/s	N/A	No	No	Yes
Material Configuration	Hardening factor	µ	0.0285	Yes	Yes	Yes
	Elastic Modulus	GPa	Tableau 4.2	Yes	Yes	Yes
	Poisson Ratio	N/A		Yes	Yes	Yes
	Yield Strength	MPa		Yes	Yes	Yes
	Strain Scaling Factor	N/A	Tableau 4.4	Yes	Yes	Yes
	Anisotropic Strain Coefficients	N/A	Tableau 4.3	No	Yes	Yes
Support structures	Support Yield Strength Ratio	N/A	0.4375	Yes	Yes	Yes

Hardening factor is asked in each strain mode, only when the J2P stress mode is selected.

APPENDIX 4B

Figure 4B.1 illustrates stress distributions within the Shape A artifact for all four simulations. It can be seen that for LE stress mode, local stresses surpass the Ultimate Strength (US) of the material (460 MPa), while it is not the case of the elastoplastic stress mode (J2P). The same effect can be observed for Shape B-P2 in Figure 4B.2.

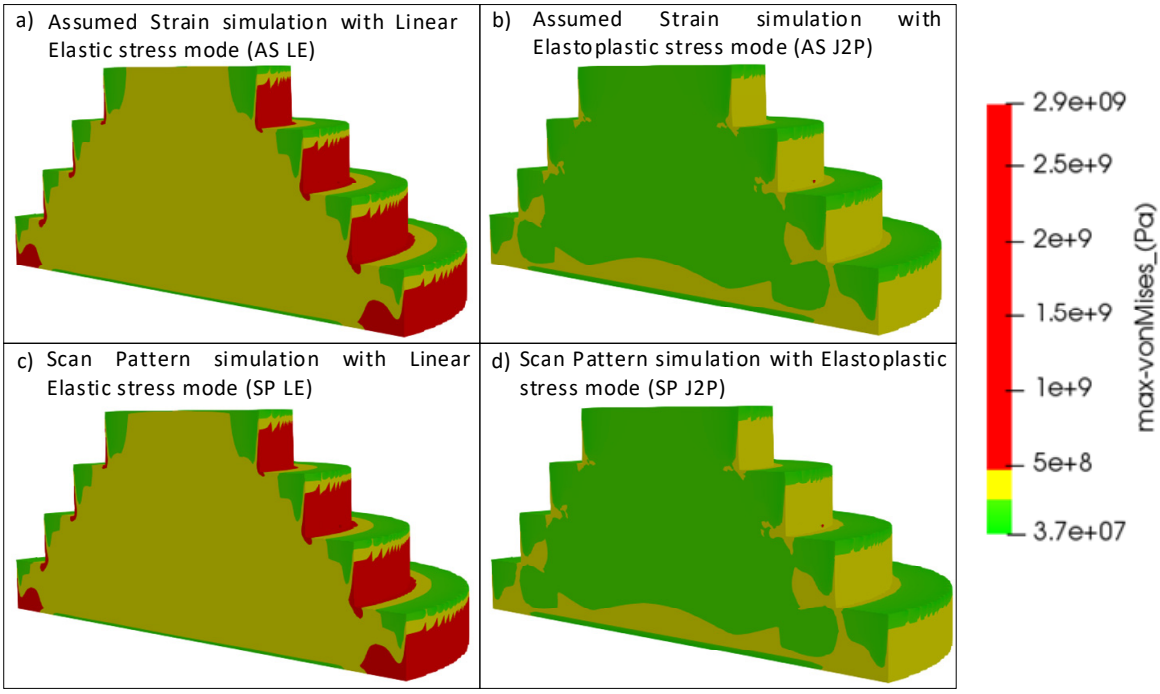

Figure 4B.1 Stress distribution of Shape A artifact for the four simulations modes. Stresses below YS in green, between YS and US in yellow, and above US in red.

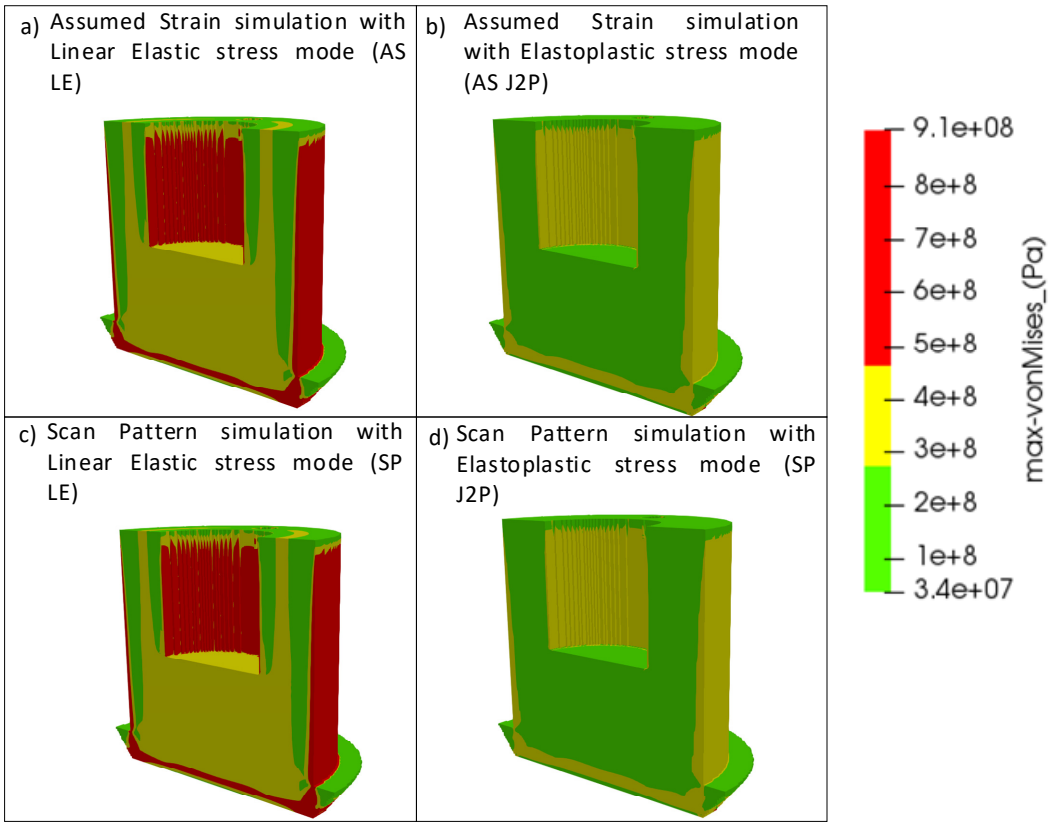

Figure 4B.2 Stress distribution of Shape B-P2 for the four simulations modes. Stresses below YS in green, between YS and US in yellow, and above US, in red.

APPENDIX 4C

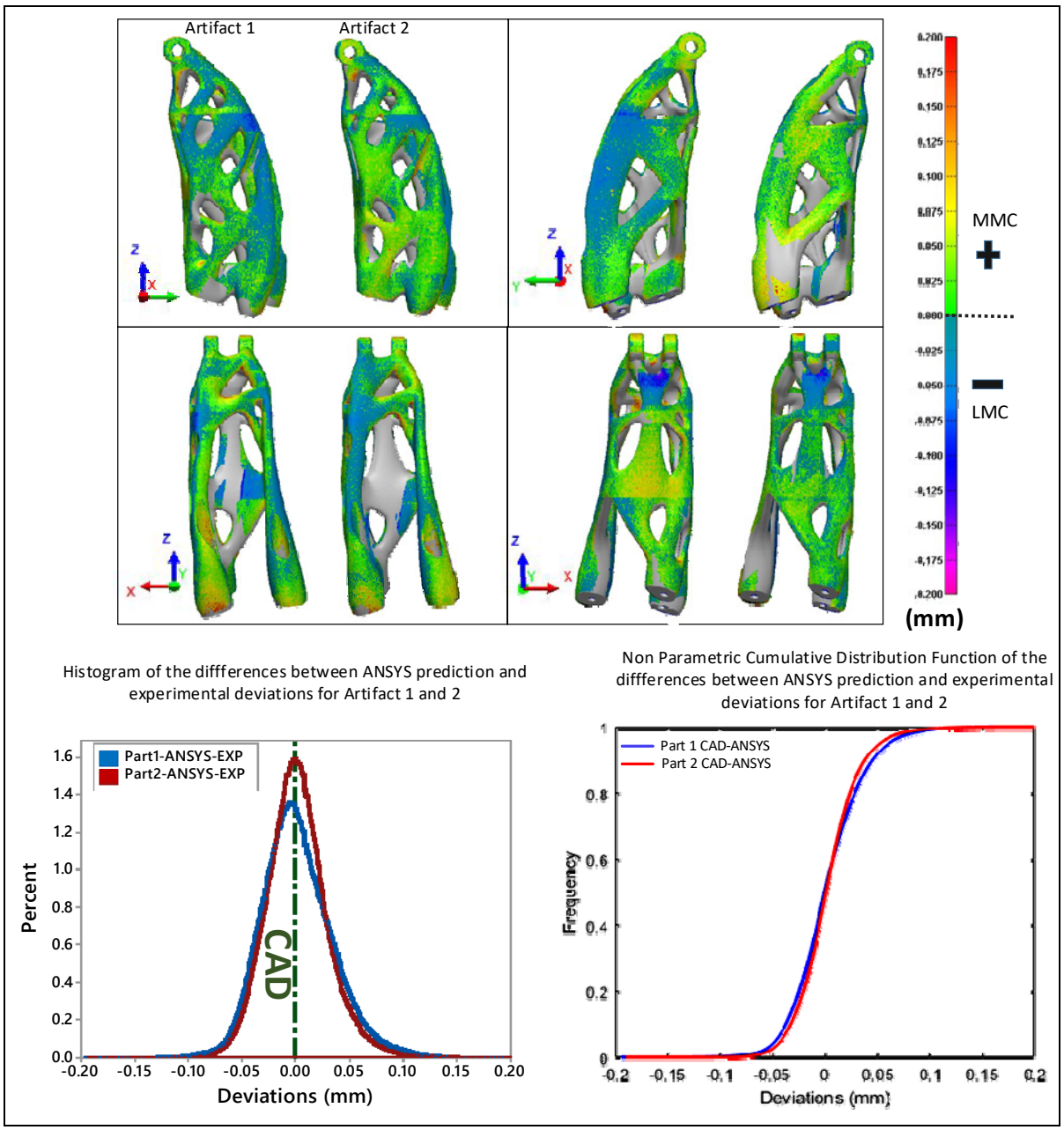

Figure 4C.1 Ansys Additive predictions accuracy for artifacts 1 and 2 comparison. Top: visual comparison with four different views of the predicted distortions. Bottom left: Histogram, and bottom right: NPCDF of the distortions

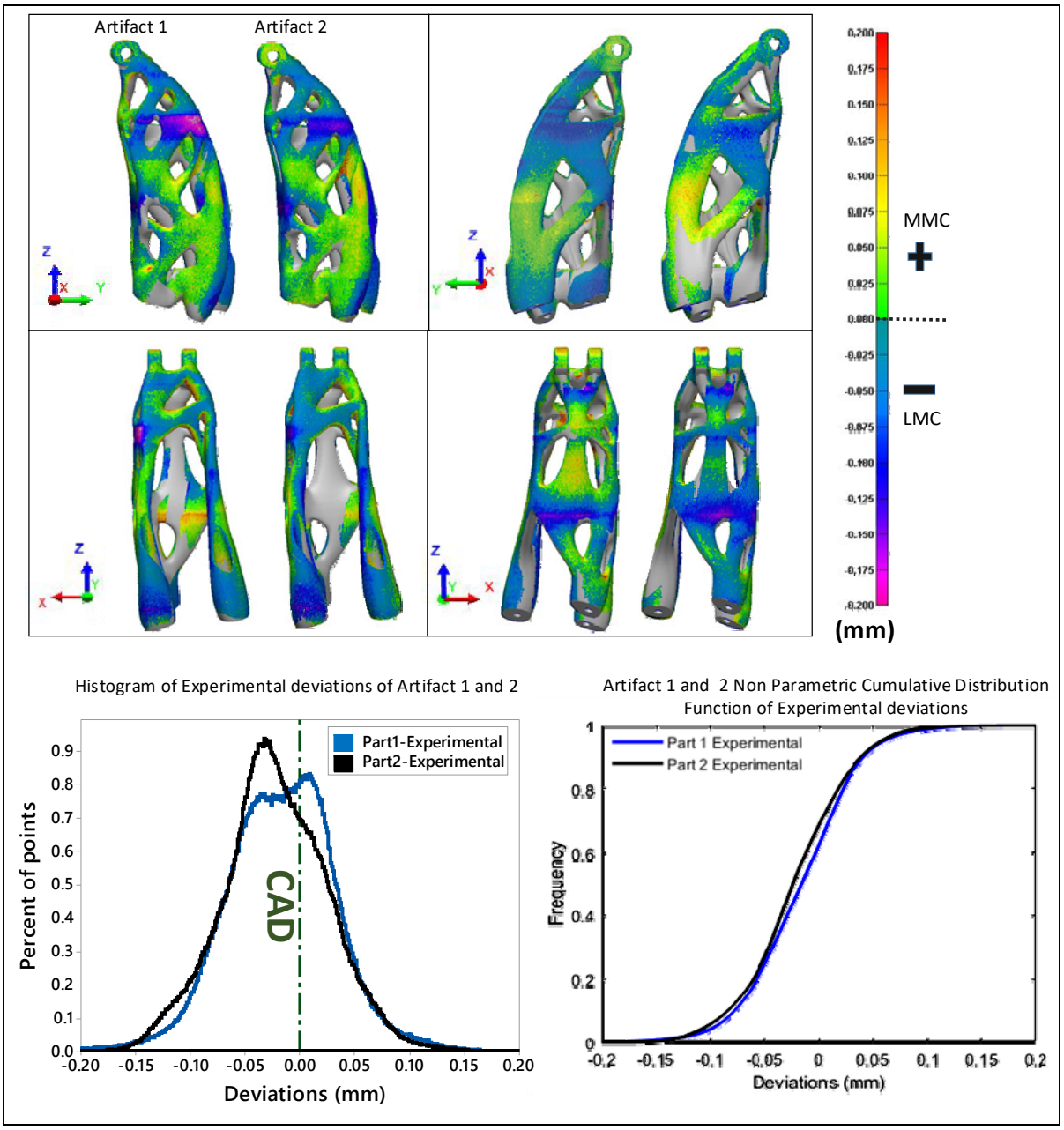

Figure 4C.2 Configuration I and II CMM detected distortion comparison. Top: visual comparison with four different views of the distortions. Bottom left: Histogram, and bottom right: NPCDF of the distortions

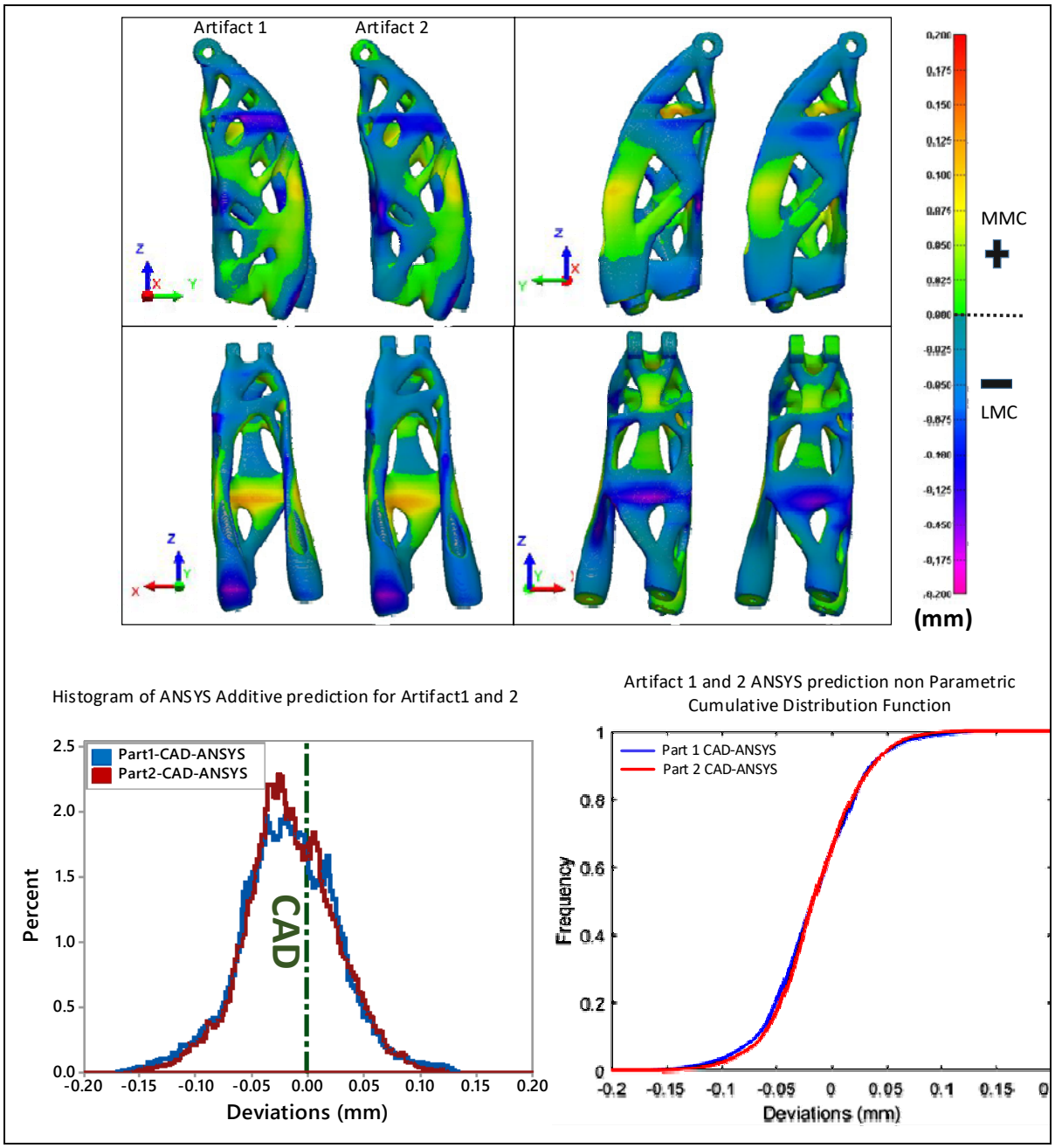

Figure 4C. 3 Ansys Additive predictions for artifacts 1 and 2 comparison. Top: visual comparison with four different views of the predicted distortions. Bottom left: Histogram, and bottom right: NPCDF of the distortions

APPENDIX 4D

The pedestal effect was investigated through artifacts 1 (no pedestal) and artifact 3 (having a pedestal) experimental deviations. The results are presented in Tableau 4D.1 and Figure 4D.1.

Tableau 4D.1 Artifacts 1 and 3 statistical description (mm)

Artifact#	Variable	Mean	StDev	$q_{25\%}$	$q_{50\%}$	$q_{75\%}$	95% interval	99.73% interval
1	EXP	-0.011	0.050	-0.043	-0.01	0.022	0.198	0.336
3		-0.017	0.049	-0.049	-0.016	0.016	0.195	0.342

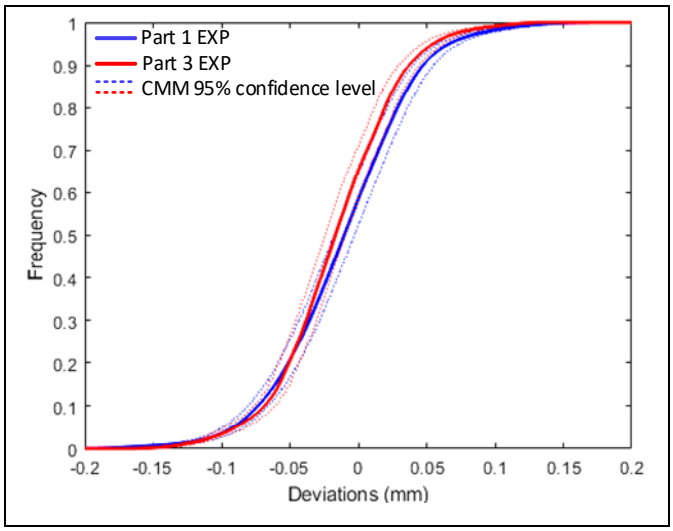

Figure 4D.1Artifacts 1 and 3 deviations histogram

APPENDIX 4E

The part removal effect was investigated through artifacts 3 experimental deviations measured before and after being removed from the build plate. The results are presented in Tableau 4E.1 and Figure 4E.1.

Tableau 4E.1Artifact 3 experimental deviations before and after part removal statistical description (mm)

Artifact #	Variable	Mean	StDev	$q_{25\%}$	$q_{50\%}$	$q_{75\%}$	95% interval	99.73% interval
3 before part removal	EXP	-0.017	0.049	-0.049	-0.016	0.016	0.195	0.342
3 after part removal		-0.030	0.047	-0.058	-0.030	-0.001	0.200	-0.030

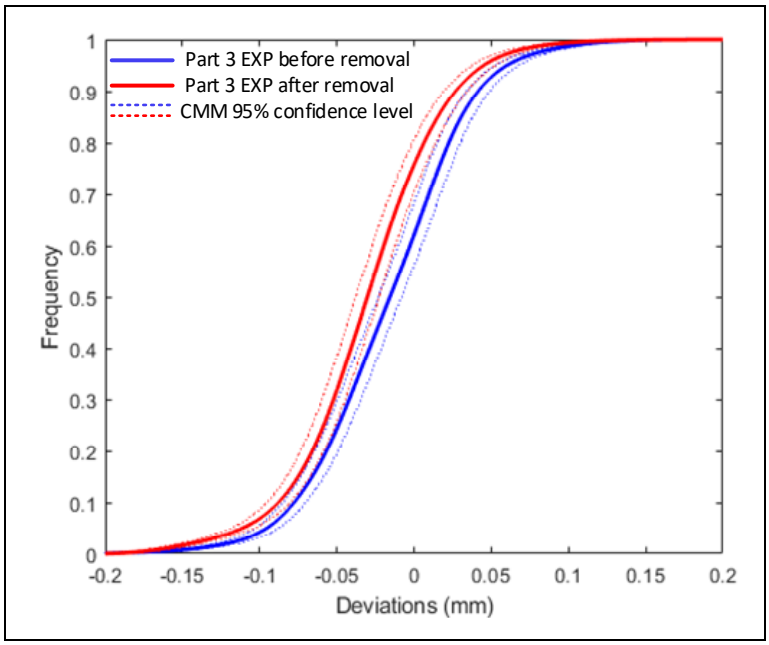

Figure 4E.1 Artifact 3 experimental deviations before and after part removal histogram

CHAPITRE 5

DIMENSIONAL DEVIATION PREDICTION MODEL BASED ON SCALE AND MATERIAL CONCENTRATION EFFECTS FOR LPBF PROCESS

This chapter describes our contribution to LPBF parts dimensional deviation prediction. Image analysis model, we implemented all investigated effects during this project. Specifically the effects that concern the parts as built, which are the *scale effect* and the *material concentration effect*. The model does not use Finite Element's analysis, takes less time to compute and provide reasonable prediction accuracy (≈4µm error in the median deviation, but ≈100µm error in the 95% deviation interval). The model is at its early stages, and will be transferred to a Ph.D. student for further investigations.

5.1 Model description

The model was developed in Matlab® 2017b (*MathWorks, Natick, MA, USA*). It is a series of morphological transformers aligned in order to slice the part in voxels and specify a value corresponding to the predicted deviation at each location of the part. The transformers are sequenced as follows:

- Import the STL mesh; Define the bonding box (Figure 5.1-1).
- Turn the STL in voxels: The resolution can be chosen using the "Alpha factor", which is the number of voxels/mm in one axis (Figure 5.1-2). The bounding box is then transformed to a binary file, in which the voxels of the part contain one and the voxel of the void contain zero.
- The first morphological operation is performed to find the "skeleton" of the shape. To do so, it thins objects to lines. It removes voxels so that an object without holes shrinks to a minimally connected stroke, and an object with holes shrinks to a connected ring halfway between each hole and the outer boundary (Figure 5.1-3).
- Then the Euclidean distance is calculated for each voxel, from the 'skeleton' to the entire bounding box (Figure 5.1-4). For each voxel, the operation assigns a number that is the distance between that voxel and the nearest nonzero voxel (which is the

"skeleton" here). The Euclidean distance between voxel A(x_A, y_A, z_A) and nearest nonzero voxel B(x_B, y_B, z_B) is given by equation 5.1:

$$d(A,B) = \sqrt{(x_B - x_A)^2 + (y_B - y_A)^2 + (z_B - z_A)^2} \quad (5.1)$$

Doing so, the voxels near the skeleton contains a lower value d than the farther ones.

- A multiplication of the 3D binary file (Figure 5.1-2) × the Euclidean computed distance (Figure 5.1-4) is performed to delete the voxels which are not representing the part (Figure 5.1-5).

The following example has been computed using a cylinder having a diameter of 20 mm and 10 mm height. The alpha value chosen is 1. Which means that the voxel size is 1×1×1 mm.
From this point, each voxel contains a different information, except the voxels in the void zone. The resulting file is treated twice, for each axes X and Y. The same deviation coefficients are applied on the X and Y axes (Figure 5.1-6). The coefficients are applied at the stage 5 (Figure 5.1-5).

On the X and Y axes, the coefficient applied is a constant. Which means that each voxel is multiplied by the chosen constant. Given that the voxels contain different numbers depending on their distances with the nearest nonzero voxel, this multiplication will modify the information in the voxels, to assimilate them to the experimental results.
Other deviation coefficients are applied on the Z axis (Figure 5.1-7). On the Z axis, the coefficient used is a third-degree equation calculated based on experimental deviations. Those coefficients are applied to the initial binary file (Figure 5.1-2).
After the coefficient applications, the predicted deviation is given by equation 5.2:

$$Deviation(X,Y,Z) = \sqrt{(Dev_X)^2 + (Dev_Y)^2 + (Dev_Z)^2} \quad (5.2)$$

Note that the predicted deviations are in the Least Material Condition (LMC).

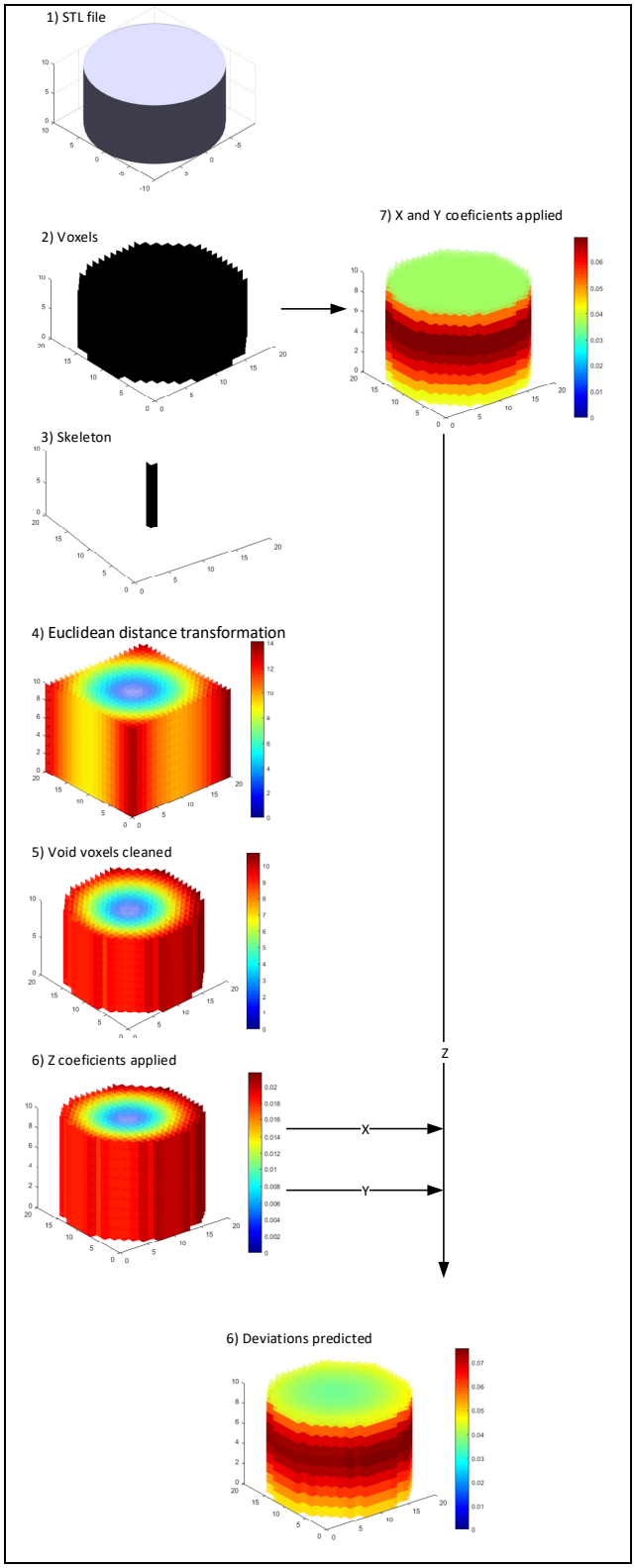

Figure 5.1 Morphological transformations and deviation coefficient application

5.2 Methodology

The model calibration consists in aligning a selected part experimental deviation with the model prediction by changing the deviations coefficients through iterations. More specifically, the alignment is made using specific features experimental deviation. As demonstrated by an investigation made using 147 parts in the first published article (CHAPITRE 2), the inspection result of part feature gives an accurate approximation of the part overall 3D profile deviation. The model calibration and the calibration results will be shown in the preliminary results section.

After the model calibration, several parts were used to investigate on the model ability to take into account the scale and material concentration effect in the deviations predictions. The parts were also printed and scanned to evaluate the model predictions capability.

The part was manufactured using the LPBF system EOSINT M280 system and AlSi10Mg powder with the AlSi10Mg_Speed 103 process parameter set (laser power 370 W, scanning speed 1300 mm/s, hatching space 0.19 mm and layer thickness 30 µm) and scanned. The point cloud of the printed parts was obtained by means of a Metris LC50 laser scan mounted on a CMM (≈±7 µm accuracy at a 95% confidence level). The experimental deviations were then compared to the model predictions. The parts used are the same as those used in the CHAPITRE 3 investigations, which contains a specific description for each of them.

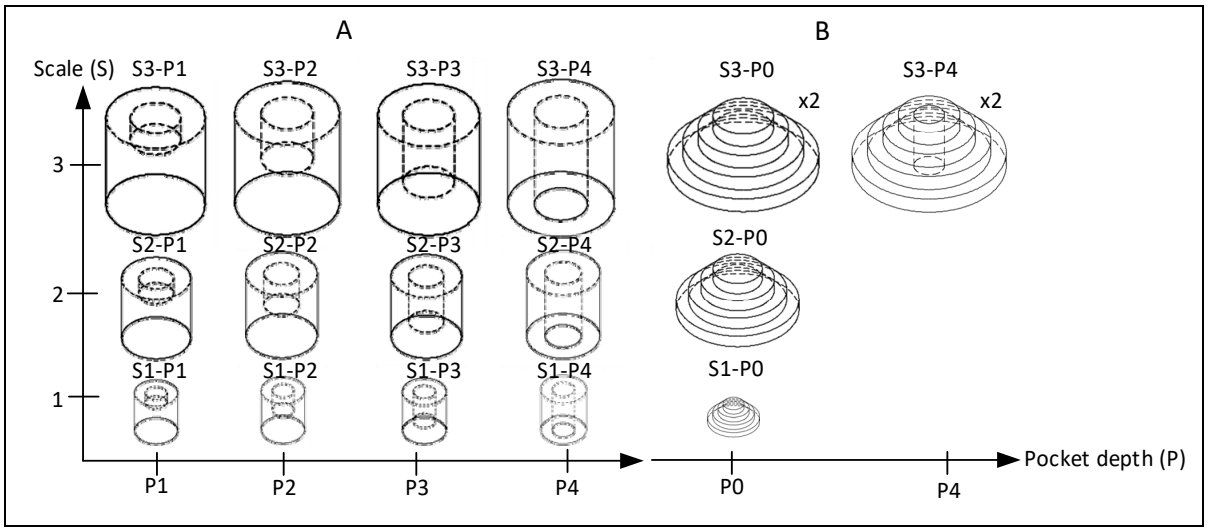

Figure 5.2 Map of the artefacts used

5.3 Preliminary results

5.3.1 Model calibration

The model was calibrated in the X and Yaxes using artifacts B diameters experimental deviations (Figure 5.3) to approximate a deviation coefficient in mm/mm.

In the Z axis, the model was calibrated using the part A-S3-P4 a $35 \times 35 \times 30mm$ height artifact external diameter extracted at different heights. The calibration consisted in aligning the model prediction with the experimental deviations.

A convergence study was conducted to investigate on the model sensibility to the voxel size. The results are presented in Tableau 5.1 and a visual comparison in Figure 5.5. The model was calibrated using alpha =10, which means that the voxel size was $100 \times 100 \times 100\mu m$. Each iteration took approximately 150s to compute. Figure 5.4 presents the alignment after the calibration. The final deviation coefficients applied are presented in Tableau 5.2.

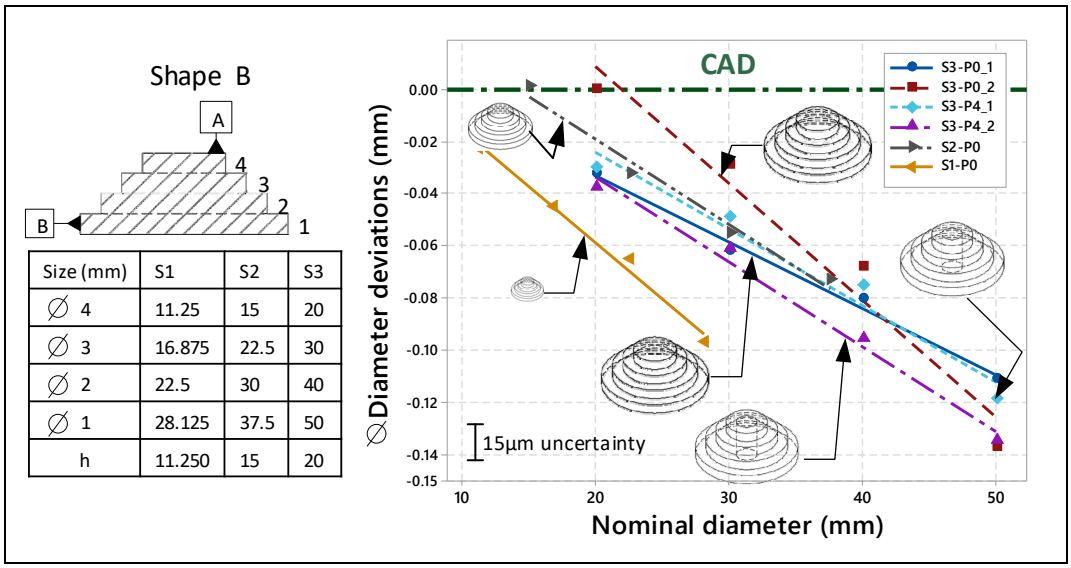

Size (mm)	S1	S2	S3
∅ 4	11.25	15	20
∅ 3	16.875	22.5	30
∅ 2	22.5	30	40
∅ 1	28.125	37.5	50
h	11.250	15	20

Figure 5.3 Shape B artifacts diameter deviations

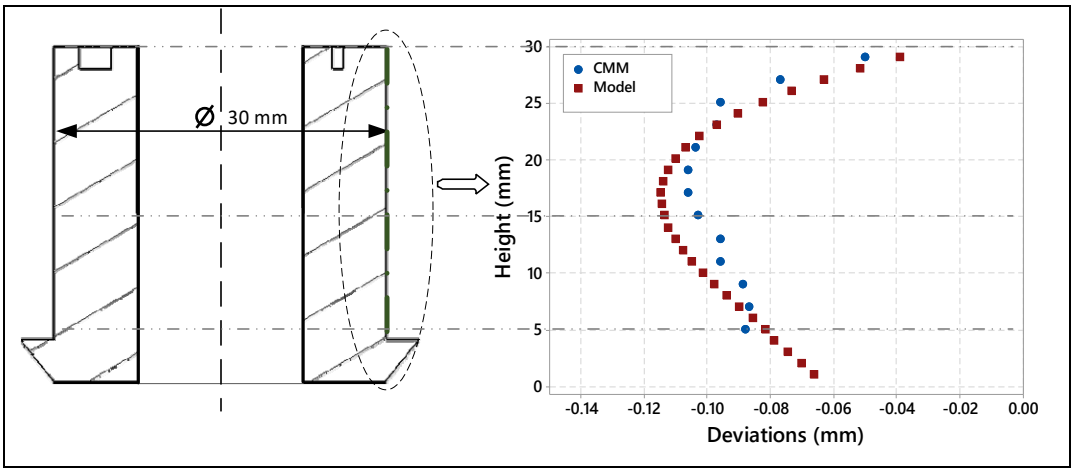

Figure 5.4 Experimental deviations vs model prediction
at the last calibration iteration

Tableau 5.1 Model sensibility to the voxel size

α	Voxel size (mm)	Number of voxels	Computation time (s)	Deviation at Z=21 mm
1	1	14885	3	-0.107
2	0.5	126044	5	-0.107
3	0.33	431471	9	-0.106
4	0.25	1030688	15	-0.106
5	0.2	2022055	19	-0.106
6	0.16	3505843	31	-0.106
7	0.14	5580774	47	-0.106
10	0.1	16332205	150	-0.106
15	0.066	55299538	662	-0.106
20	0.05	1.31E+08	3087	-0.106

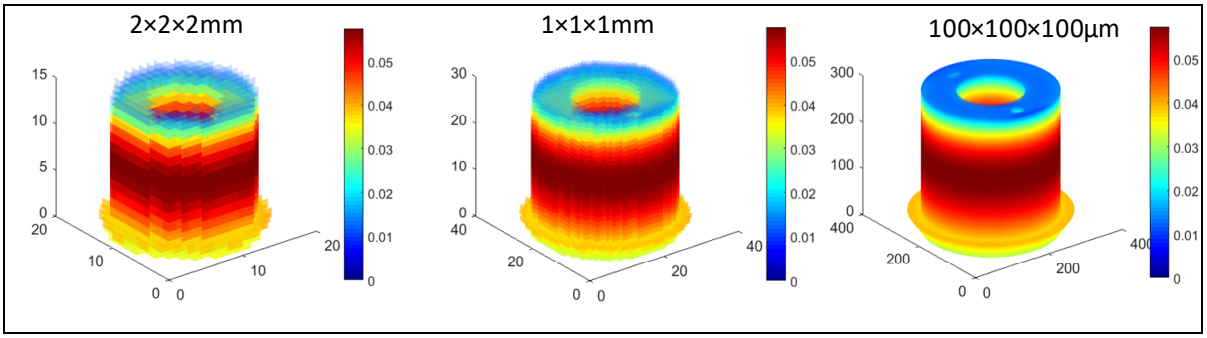

Figure 5.5 Visual comparison of the voxel size effect in the deviation prediction

Tableau 5.2 Deviation coefficients applied for each axis

Axis	Coefficient mm/mm
X	0.0015
Y	
Z	$-0.03 - 0.05x - 0.08x^2 + 0.15x^3$

With x the relative height, (considered height/total height)

5.3.2 Scale effect

After the calibration, artifacts A-P2 (Figure 5.6) and B-P0 (Figure 5.7) were computed at three different scales, S1, S2 and S3 to test the model ability to take into account the scale effect. The first line presents the visual result of the model concerning each part, along with their color scales. Note that the predicted deviations are in the LMC direction (negative deviation or shrinkage). Figure 5.6-b and Figure 5.7-b present the non-parametric cumulative distribution function of the parts deviations predicted by the model.

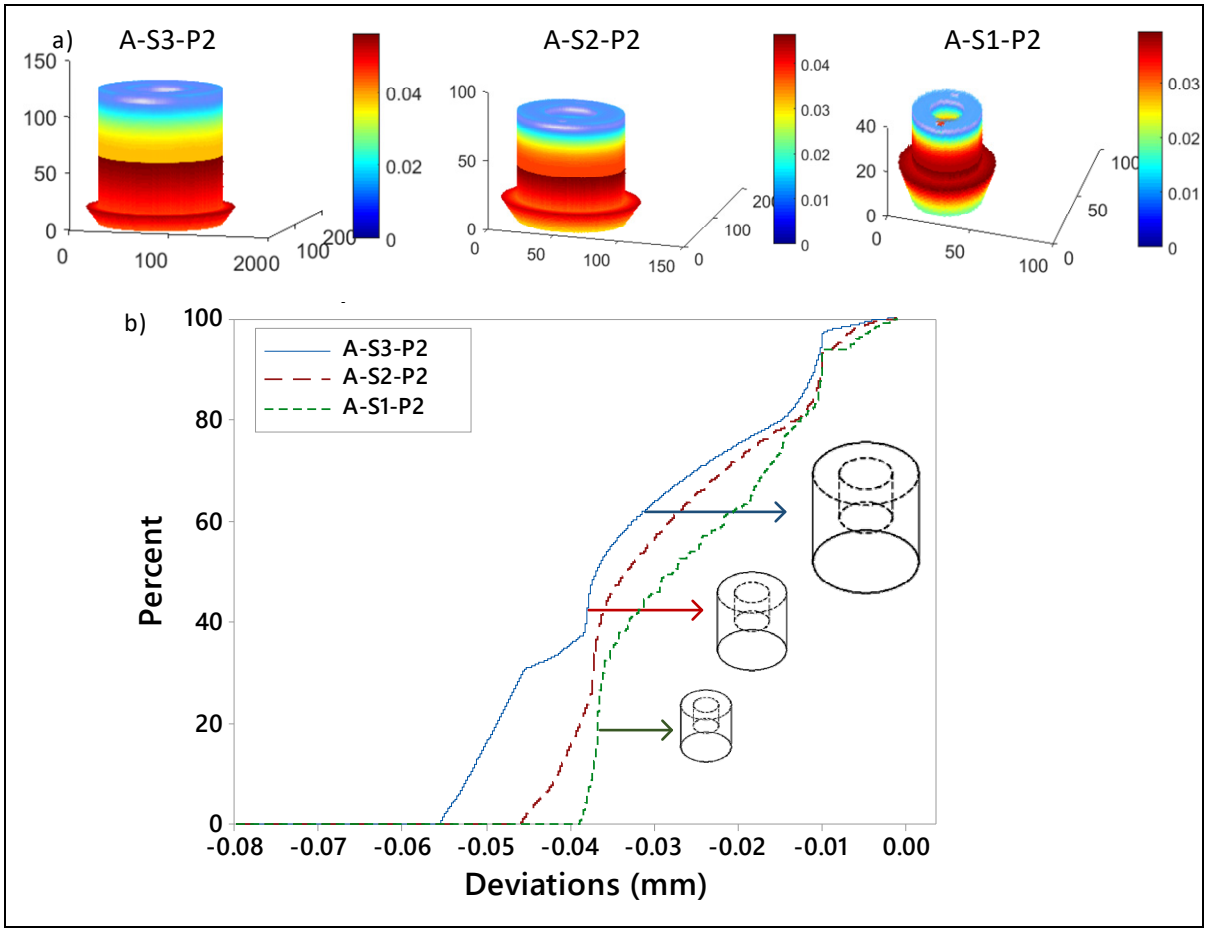

Figure 5.6 Scale effect observed using the Model on A-P2 artifacts at scale S1 to S3

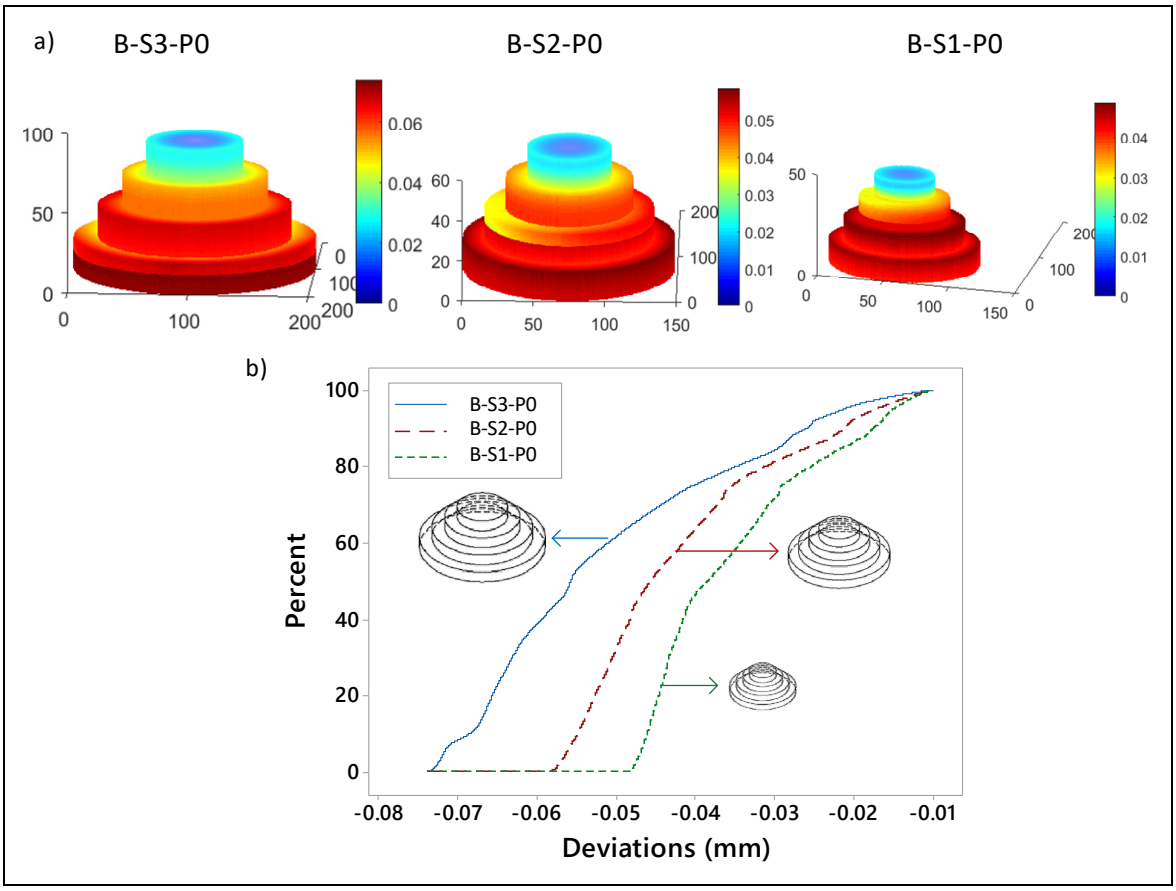

Figure 5.7 Scale effect observed using the Model on B-P0 artifacts at scale S1 to S3

This investigation confirmed the model ability to take into account the scale effect on the deviations prediction.

5.3.3 Material concentration effect

Artifacts A-S3-P1 and 4 (Figure 5.8) and B-S3-P0 and 4 (Figure 5.9) were used to test the model ability to take into account the material concentration effect. The first line presents the visual result of the model concerning each part, along with their color scales. Note that the predicted deviations are in the LMC direction (negative deviation or shrinkage). Figure 5.8-b and Figure 5.9-b present the non-parametric cumulative distribution function of the parts deviations predicted by the model.

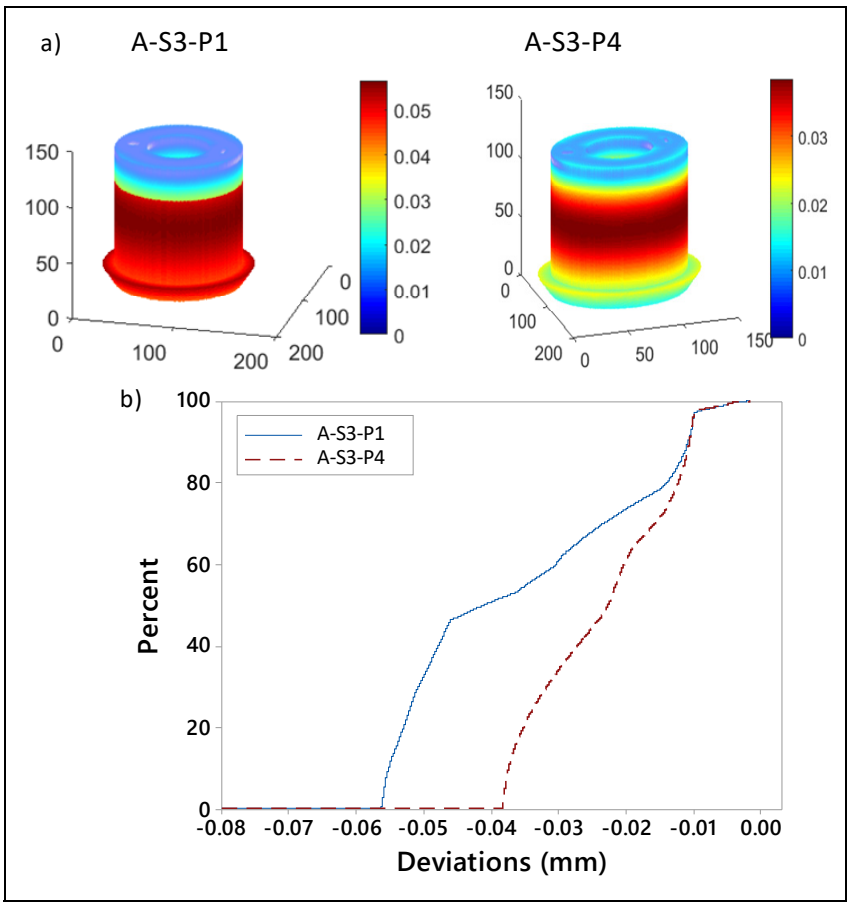

Figure 5.8 Material concentration observed using the Model on A-S3-P1 and A-S3-P4 artifacts

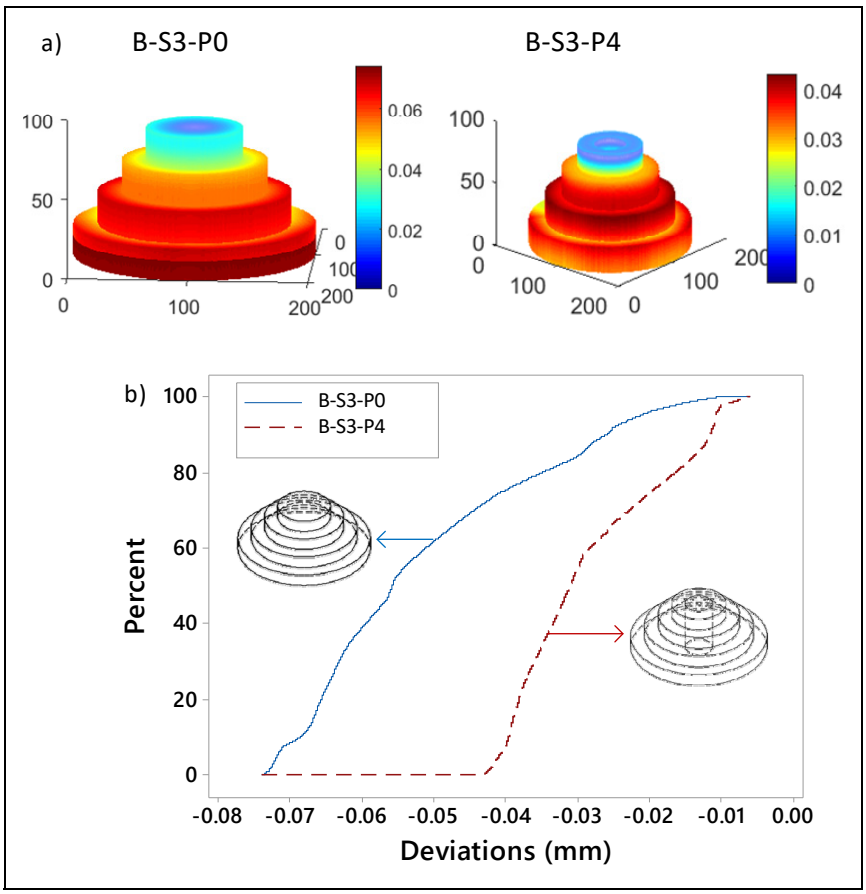

Figure 5.9 Material concentration observed using the Model on B-S3-P0 and B-S3-P4 artifacts

This investigation confirmed the model ability to take into account the material concentration effect on the deviations prediction.

5.3.4 Prediction capabilities

The model prediction capabilities was investigated using parts A-S1-P2 (Figure 5.10), B-S3-P0 (Figure 5.11) and a more complex part, a control arm link (Figure 5.12). The experimental deviations (CMM) were compared to the prediction of our model and to ANSYS Additive deviation predictions Figure 5.12. Tableau 5.3 present the statistical description of the experimental and predicted deviations.

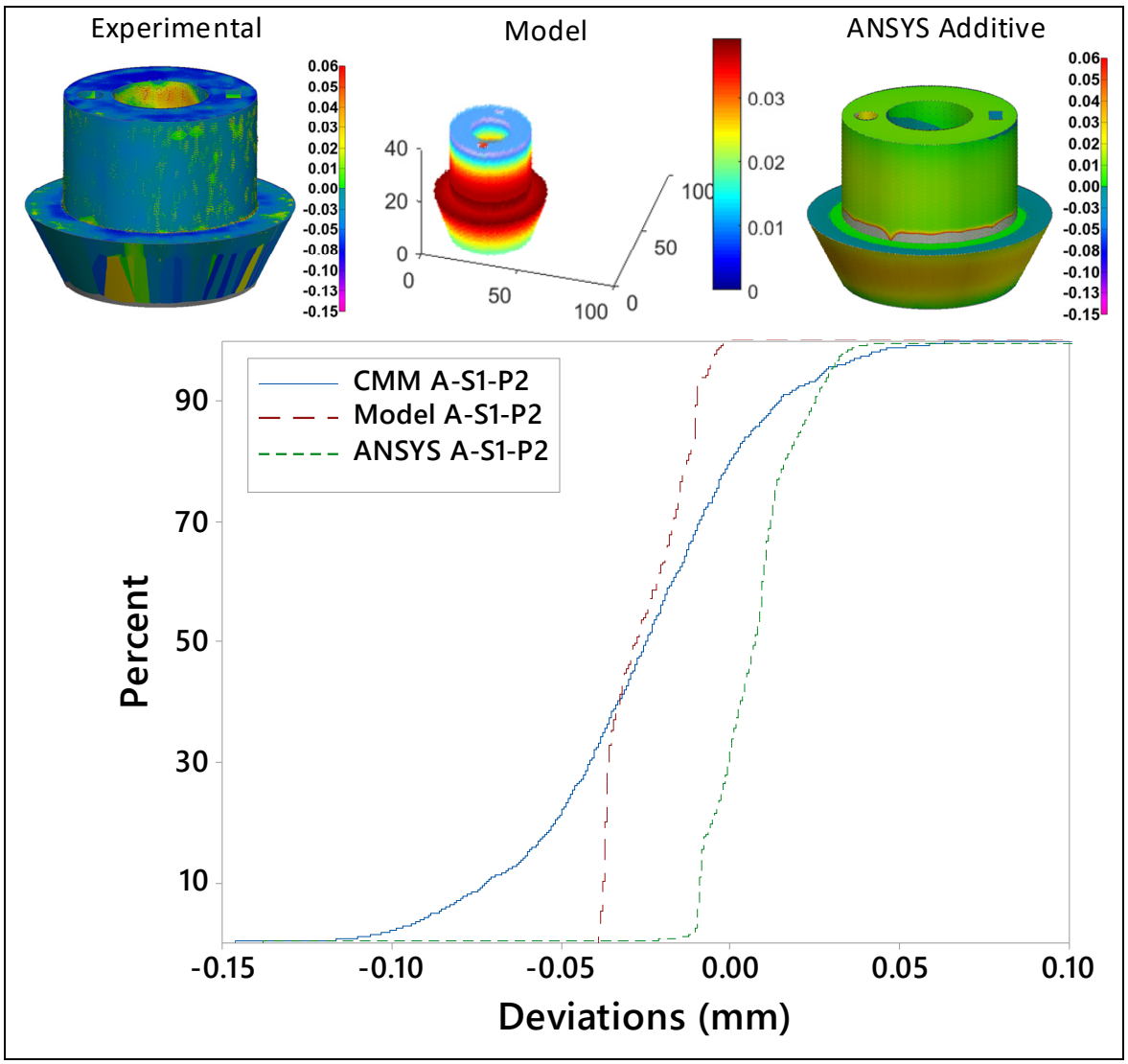

Figure 5.10 Experimental deviations (blue) vs Model predication (red) and ANSYS (green) non parametric cumulative deviation function for artifact A-S1-P2

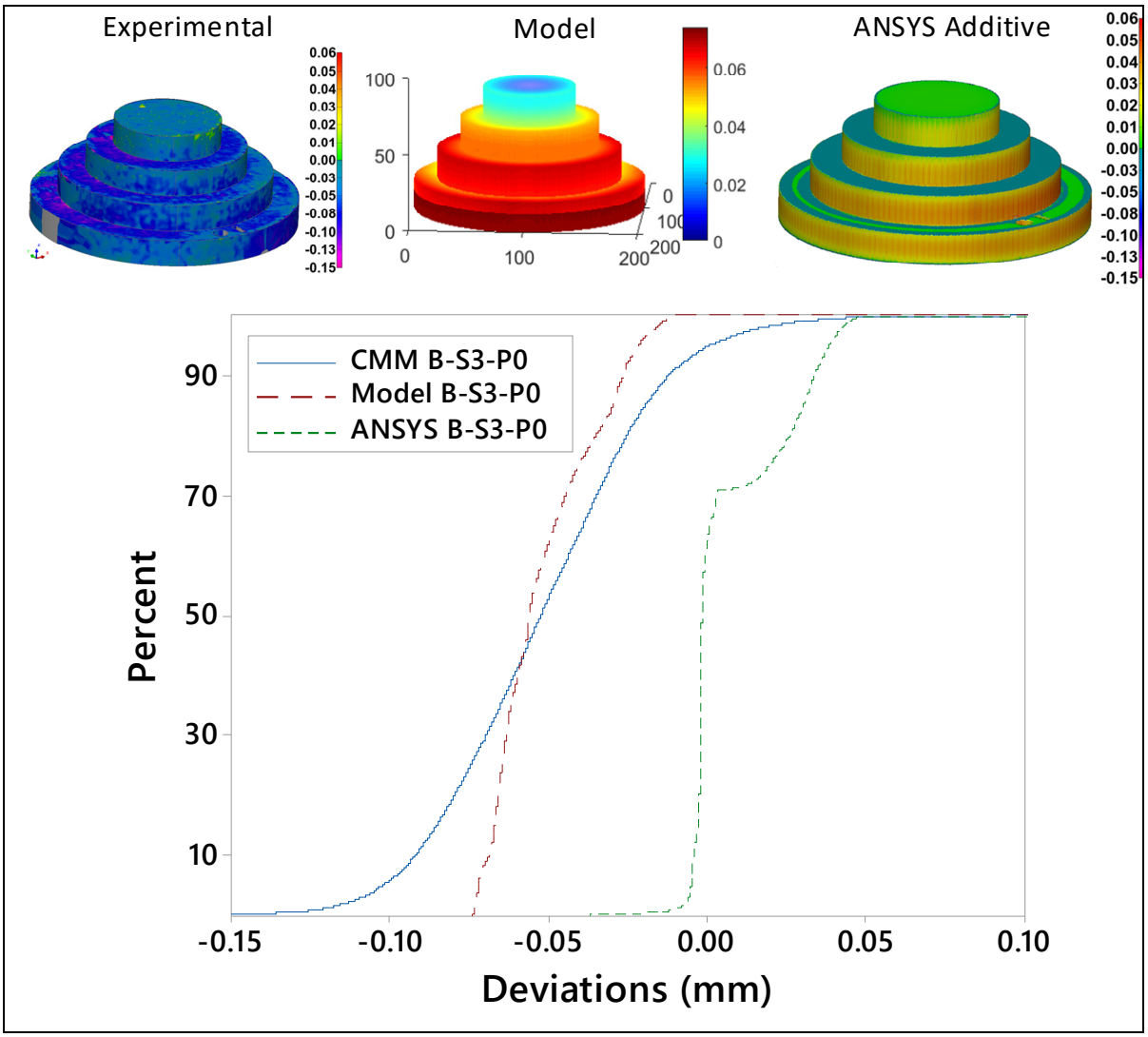

Figure 5.11 Experimental deviations (blue) vs Model predication (red) and ANSYS (green) non parametric cumulative deviation function for artifact B-S3-P0

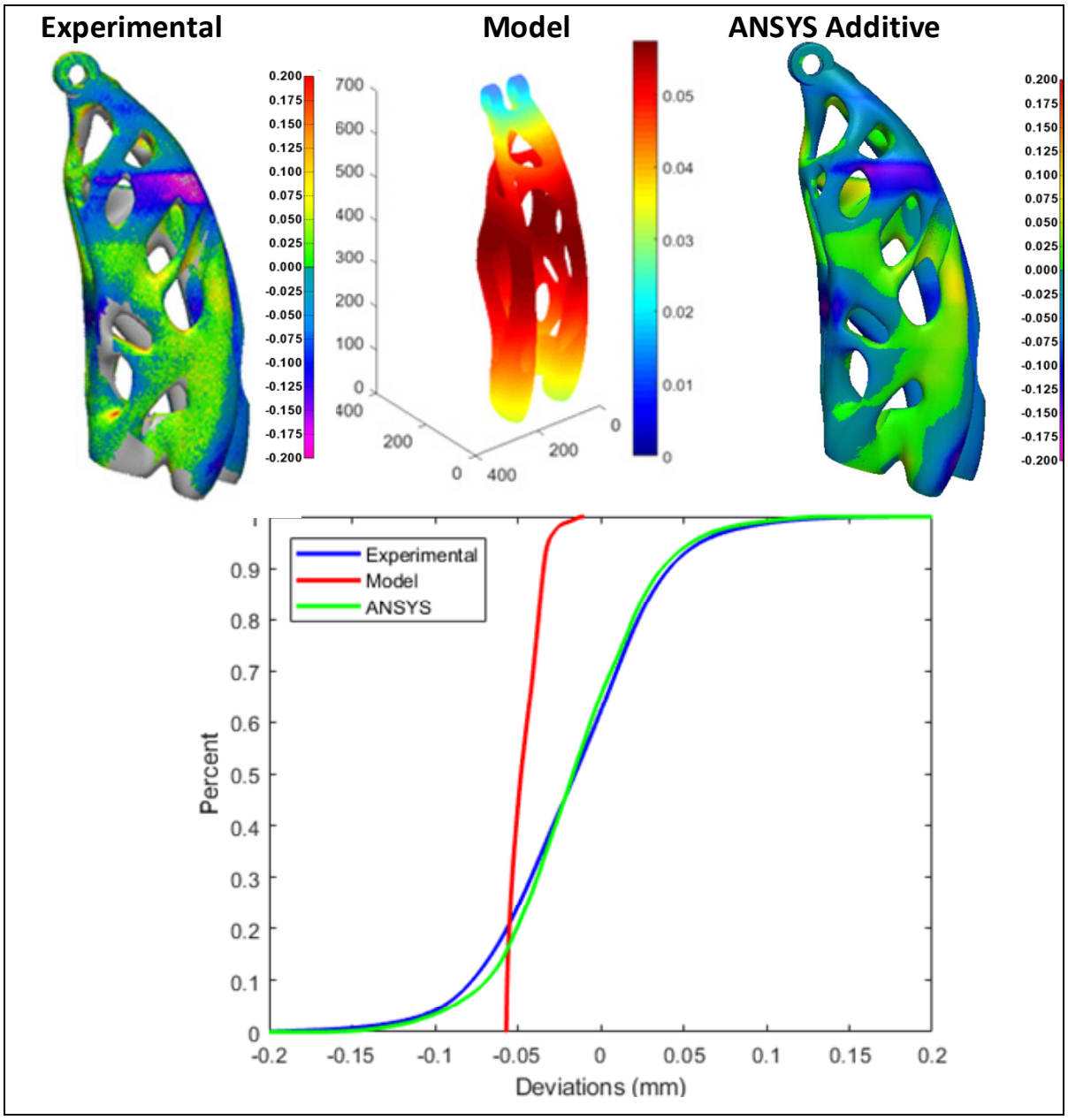

Figure 5.12 Experimental deviations (blue) vs Model predication (red) and ANSYS (green) non parametric cumulative deviation function for the control arm link

Tableau 5.3 CMM detected deviations vs Model prediction statistical description (in mm)

Part	Variable	Mean	StDev	Q1	Median	Q3
A-S1-C2	CMM	-0.026	0.034	-0.046	-0.025	-0.004
	Model	-0.025	0.011	-0.037	-0.028	-0.015
	ANSYS	0.019	0.161	-0.002	0.007	0.013
B-S3-C0	CMM	-0.052	0.032	-0.074	-0.052	-0.030
	Model	-0.051	0.016	-0.064	-0.056	-0.040
	ANSYS	0.007	0.021	-0.002	-0.001	0.020
Control arm link	CMM	-0.017	0.049	-0.049	-0.016	0.016
	Model	-0.046	0.009	-0.054	-0.048	-0.039
	ANSYS	-0.016	0.045	-0.044	-0.017	0.013

The model was calibrated using a simple part features deviations, which explains the good alignment with the experimental mean and median deviation of simple parts A-S1-C2 and B-S3-C0. However, the model deviation spectrum is thin compared to the experimental deviation spectrum. This can be explained by the coefficients deviations applied in the Z direction. They are determined using a specific feature deviation behaviour over the Z axis, which is a good indicator of the overall 3D profile deviation, but doesn't represent the overall 3D profile deviation spectrum.

The model limits are revealed when he is tested using more complex parts because these parts have more variations in their sections material concentration in the height axis.

5.4 Conclusion

This chapter presents a model, which is still under development, and will be transferred for further investigations. Our recommendations concerning this model is to dedicate it to simple parts, and improve its calibration process mostly in the Z direction by automating the coefficients choice.

CONCLUSION

Les travaux présentés dans ce document traitent d'une problématique majeure de l'impression 3D métallique : prédire l'amplitude des défauts dimensionnels et géométriques des pièces fabriquées.

Dans le Chapitre 1, nous avons présenté une revue succincte de la littérature scientifique et de l'état de l'art du domaine. Nous y avons aussi présenté la méthodologie proposée pour tenter de répondre aux questions de recherche telles que formulées et nous avons conclu par une présentation de la structure de la thèse (sous forme de trois articles). Plus spécifiquement, après avoir listé les règles de conceptions d'un benchmark géométrique et expliqué leur utilité, la revue de littérature a présenté une partie des benchmarks géométriques fabriqués depuis 1991. Ensuite nous avons expliqué la différence entre deux caractéristiques investiguées avec les benchmarks géométriques que sont la capabilité (terme encadré par ISO 22514) et la faisabilité. Enfin, nous avons exposé les conclusions constructives des investigations réalisées avec ces artéfacts et quelques essais de prédiction des défauts.

Notre point de départ a été de se questionner. *Quel est l'intervalle probabiliste correspondant à 99,73% (équivalent à 6σ) des déviations géométriques d'une pièce imprimée? Les données d'inspection d'une forme géométrique simple (ex. cylindre, épaisseur, etc.) peuvent-elles être exploitées pour prédire les déviations du profil d'une pièce plus complexe? Dans une chambre d'impression, le choix de l'emplacement de la pièce influence-t-il systématiquement les défauts qu'elle aura? À quel point le procédé est-il répétable à l'intérieur de la même impression? Est-ce que cette répétabilité est constante d'une impression à une autre (avec les mêmes paramètres)?*

Autant de questions auxquelles nous avons tenté d'apporter une contribution dans le Chapitre 2, à l'aide de 49 échantillons identiques imprimés sur toute la surface utilisable de la plaque d'impression. En répétant cette opération sur trois impressions avec les mêmes paramètres, nous avons réalisé une étude expérimentale. Cette investigation, réalisée sur 147 pièces, nous

a permis de conclure qu'il n'y a pas une différence significative sur le niveau des déviations géométriques pour chaque lot de 49 échantillons imprimés dans la chambre d'impression, et que la répartition des déviations en fonction de l'emplacement d'impression n'est pas répétable d'une impression à une autre. Il n'y a donc pas d'influence systématique des défauts en fonction du choix d'emplacement des pièces dans la chambre d'impression. Aucune tendance n'a été détectée d'une impression à une autre. Les variations étaient de l'ordre de 230 µm dans l'intervalle de 99.73% (6σ) pour les 147 pièces.

Les résultats de l'inspection du diamètre d'un élément cylindrique présent sur la pièce ont montré une corrélation directe avec les déviations du profil de la pièce entière sur les 147 pièces. Ce qui confirme que les données d'inspection d'une forme géométrique simple peuvent être exploitées pour prédire les déviations du profil de la pièce considérée. Cette étude a fait l'objet de notre première publication dans un journal avec comité de lecture.

Le deuxième jalon de notre recherche a été d'investiguer l'effet d'échelle. *En émettant l'hypothèse qu'une même géométrie fabriquée à plusieurs échelles possède un comportement différent (amplitudes des déviations), Cette loi est-elle linéaire? Est-ce qu'elle est reproductible sur une autre géométrie?* Et comme corollaire à ce questionnement, *en concevant dans le même espace de travail (même échelle), des pièces ayant des répartitions de matière différentes (différentes concentrations de matière), est-ce que le niveau des déviations géométriques demeure constant? Ou alors, serait-il plus prononcé sur les pièces les plus denses?*

Finalement, quelle est l'influence dimensionnelle du traitement thermique de relaxation des contraintes (étape recommandée par les fabricants de systèmes d'impression métallique)? Quel est l'effet de ce traitement sur l'évolution des déviations géométriques des pièces imprimées? Est-ce que son effet est influencé par les dimensions (échelle) de la pièce ou de la répartition de matière sur la pièce?

Une étape obligatoire pour les pièces imprimées par le procédé LPBF est l'enlèvement (l'extraction) des pièces de la plaque d'impression. Cette opération qui est souvent réalisée avec une lame chauffée ou une scie a un effet sur les déviations géométriques des pièces.

Cependant, son effet est-il différent en fonction de la taille de la pièce concernée? En fonction de la répartition de matière de la pièce?

Une des limitations inhérentes au procédé LPBF est la qualité toute relative du fini de surface (rugosité) des pièces. L'opération de polissage par jet abrasif d'un mélange d'air et de sable (*Sand Blast*) ou par projection de particules est un moyen de remédier à cette carence. Cette opération affecte directement des données externes, uniformément si elle est réalisée en respectant le temps de soufflage, la pression appliquée et la distance avec la pièce. *Dans des conditions d'exécution idéales, quel est son impact réel sur les pièces?*

Dans le Chapitre 3, qui a fait l'objet de notre deuxième publication dans un journal avec comité de lecture, nous avons entrepris de répondre aux questions précédentes. Après avoir quantifié l'effet d'échelle, nous nous sommes rendu compte que la loi de comportement est linéaire lorsque les inspections sont réalisées sur des formes avec plusieurs échelles, mais présentes sur la même pièce imprimée (effet d'échelle intra-pièce) et que cet effet est répétable. Aussi, nous avons démontré que la concentration de matière a un effet direct sur l'amplitude des défauts de la pièce. Conçues dans le même espace de travail, les pièces les plus denses ont affiché de plus grands défauts. De façon générale, le traitement thermique a considérablement diminué l'amplitude des défauts dimensionnels des pièces. Aussi, nous avons démontré via notre étude expérimentale qu'à géométrie identique et échelle différente, l'effet du traitement thermique est plus grand sur les pièces de plus grande taille. Et qu'à échelle identique et quantité de matière différentes, son effet est plus grand sur les pièces contenant le plus de matière. L'enlèvement des pièces de la plaque a négativement impacté l'amplitude de leurs défauts, en affectant plus les pièces les plus grandes et qui contiennent plus de matière.

La majeure partie des déviations de la pièce finale (après la relaxation des contraintes, l'enlèvement de la plaque et le nettoyage) survient au moment de l'impression. La modification du fichier CAO (ou CAD) en prévision de ses déviations à cette étape est donc un moyen robuste de diminuer les défauts des pièces finales. Cependant, pour corriger le modèle CAO original, il faut d'abord être capable de prédire les déviations systématiques des pièces « *as-built* ». Cette dernière problématique a fait l'objet de nombreux travaux durant la dernière décennie, qui ont, pour certains, abouti à la mise sur le marché des logiciels dédiés à cette

tâche, plus ou moins performants. L'un d'entre eux ANSYS Additive Print® (ANSYS, Canonsburg, PA, USA) a particulièrement attiré notre attention par les performances affichées. Nous nous sommes intéressés à la qualité de prédiction des déviations dimensionnelles, sur lesquelles nous avons investigué, et qui a fait l'objet de trois présentations de conférence et de notre troisième publication dans un journal avec comité de lecture. Sur presque toutes les pièces qui ont fait l'objet d'investigations, le logiciel a bien prédit les tendances de défauts observées expérimentalement. Cependant, nous avons remarqué que le logiciel sous-estime des défauts, et prédit avec beaucoup moins de précision les défauts des pièces qui ont une plus grande concentration de matière, relativement à celles qui sont relativement creuses. Également, nous avons mis en évidence que le logiciel prédit moins précisément les défauts intervenant dans la partie basse des pièces, près de la plaque.

Le Chapitre 5 présente une idée d'un modèle original qui a pour vocation de prédire (sans recours à des simulations par éléments finis) les déviations dimensionnelles des pièces en tenant compte, et en pondérant, les différents facteurs qui ont un effet sur le comportement dimensionnel des pièces « *as-built* » et sur lesquels nous avons déjà investigué, à savoir de l'effet d'échelle, et l'effet de la concentration de matière. Dans le Chapitre 5, nous avons démontré, à travers quatre exemples de validation, la capabilité du modèle à prendre en compte ces différents effets. Une étude a également été menée sur deux pièces différentes en termes d'échelle et de concentration de matière, en comparant les prédictions du modèle avec des mesures expérimentales pour quantifier la fiabilité de ses prédictions. Cette étude préliminaire fera l'objet d'une passation de connaissances et sera améliorée dans le cadre d'un autre projet de doctorat. Nous espérons que notre étude a apporté un éclairage supplémentaire sur le comportement dimensionnel des pièces imprimées par le procédé LPBF.

Dans ce même ordre d'idées, des propositions pour de futures recherches reliées à ce domaine sont présentées dans la partie suivante « Recommandations ».

RECOMMANDATIONS

L'un des objectifs de cette thèse était d'investiguer sur le comportement dimensionnel des pièces issues du procédé LPBF, à savoir l'effet d'échelle et l'effet de la concentration de la matière, et de les intégrer dans un outil de prédiction. Le but étant d'apporter aux concepteurs de nouvelles informations sur le procédé, pour qu'ils soient pris en compte pendant la conception des pièces.

Dans le cadre de cette thèse, nous avons mis en lumière des effets qui n'avaient pas encore été répertoriés dans la littérature. Et nous avons tenté d'implémenter ces réponses dans un outil de prédiction. Nous espérons que notre contribution aidera à apporter une meilleure connaissance et compréhension du procédé. Cependant, plusieurs opportunités d'amélioration subsistent.

De manière générale, pour une plus grande confiance d'un point de vue statistique, nous recommandons que les futures investigations soient faites avec un plus grand nombre de pièces sur les effets à étudier. Plus spécifiquement, dans l'article #2 déjà publié, nous avons investigué et quantifié de nombreux effets intrinsèques au procédé, dont il faut tenir compte pour prédire les déviations des pièces fabriquées. Nous avons utilisé 18 échantillons pour l'ensemble de nos investigations. Pour certains effets comme l'amplitude de l'effet d'échelle intra-pièce, nous ne disposions que de 4 échantillons. Augmenter la quantité de données collectées à ce sujet apportera une confirmation statistique supplémentaire.

Dans l'article #3, nous avons étudié la qualité de prédiction des déviations dimensionnelles du logiciel ANSYS Additive®. Dans cette analyse, nous n'avons cependant pas vérifié que le logiciel prend bien en compte tous les effets intrinsèques au procédé (effets investigués et ceux répertoriés par la littérature). Dans de futurs travaux reliés à ce logiciel, il serait opportun de vérifier sa capacité à prendre en compte l'effet d'échelle, et surtout, sa capacité à prédire cet effet avec exactitude. Il serait aussi très avantageux d'investiguer sur sa prédiction les contraintes résiduelles des pièces « *as-built* ».

Par ailleurs, toutes ces études ont été réalisées avec une EOS M280, un alliage d'aluminium AlSi10Mg, et le set de paramètres recommandés par le fabricant de la machine. Élargir les hypothèses en incluant un nouveau matériau et une nouvelle machine pourrait permettre d'isoler les effets intrinsèques à la machine utilisée ou au matériau imprimé.

Nous avons développé un modèle, qui peut être qualifié de préliminaire, dans lequel nous avons implémenté les effets observés en tentant de prédire les déviations des pièces. Nous recommandons d'investiguer sur le coefficient dans l'axe Z qui est celui qui influence le plus les déviations, et de le dédier aux pièces simples, ou tenter de le généraliser le plus possible à toutes les formes en reformulant l'influence des déviations de l'axe Z sur la prédiction. Pour la suite, nous recommandons vivement de travailler à calibrer automatiquement le modèle, ce qui permettra un grand gain de temps. Pour ce faire, à la lumière de récentes publications [112], nous recommandons fortement la piste de l'utilisation de l'intelligence artificielle pour les défis à venir concernant l'outil développé, et la prédiction des déviations dimensionnelles de pièces issues de la fabrication additive en général.

Finalement, nous ne pourrons émettre des recommandations pour de futurs travaux visant à encourager l'adoption du procédé LPBF et de l'impression 3D métallique en général, sans proposer d'investiguer sur les autres problématiques majeures associées au procédé, à savoir, l'adaptation de nouvelles poudres métalliques, l'investigation sur les problématiques qui entourent la génération de supports adéquats, leur impact sur les pièces, ou encore l'impact des directions de fabrication.

Nous espérons avoir répondu en grande partie au cahier de charges imposé lors du début du projet. Certes, il existe encore plusieurs questions en suspens, *mais une recherche est-elle vraiment terminée?*

ANNEXE I

BENCHMARKS GÉOMÉTRIQUES DE 1991 À 2019

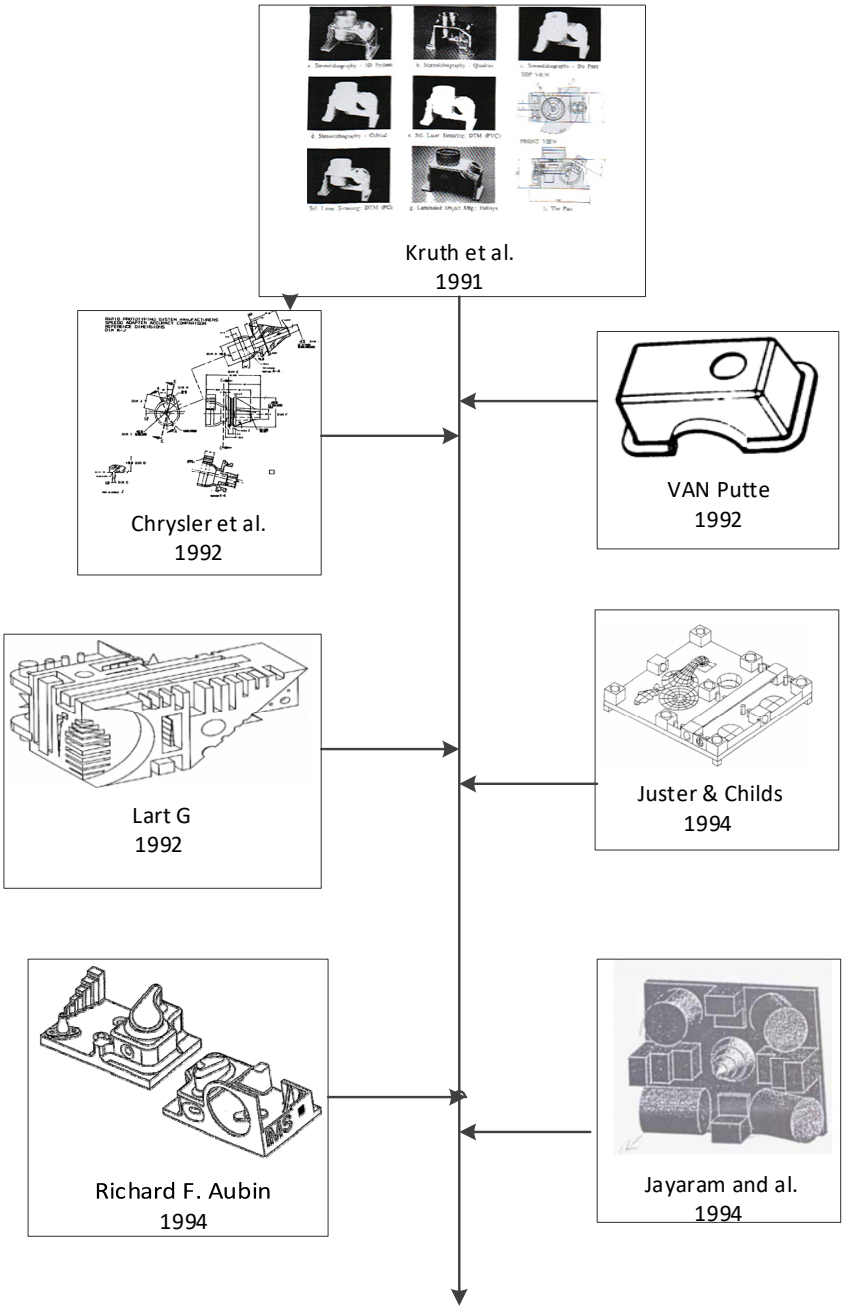

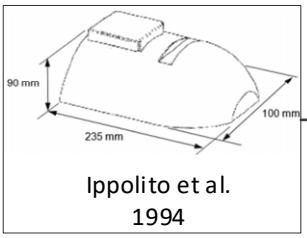

Ippolito et al.
1994

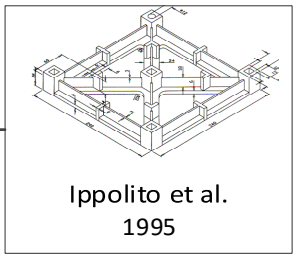

Ippolito et al.
1995

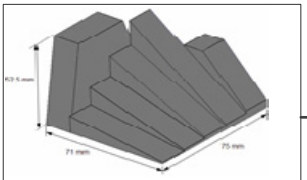

Reeves & Cobb
1995

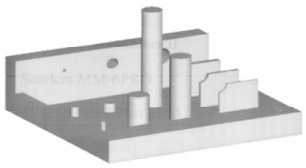

Loose K, Nakagawa T
1998

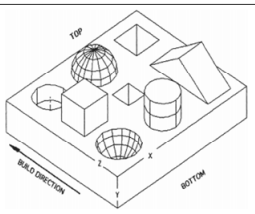

Zhou & al.
2000

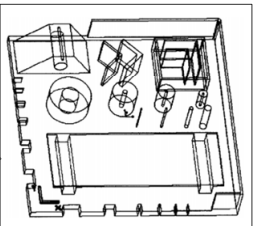

Xu F& al.
2001

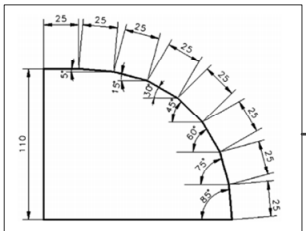

Perez CL
2002

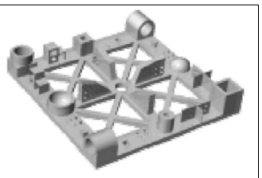

Byun & Lee
2003

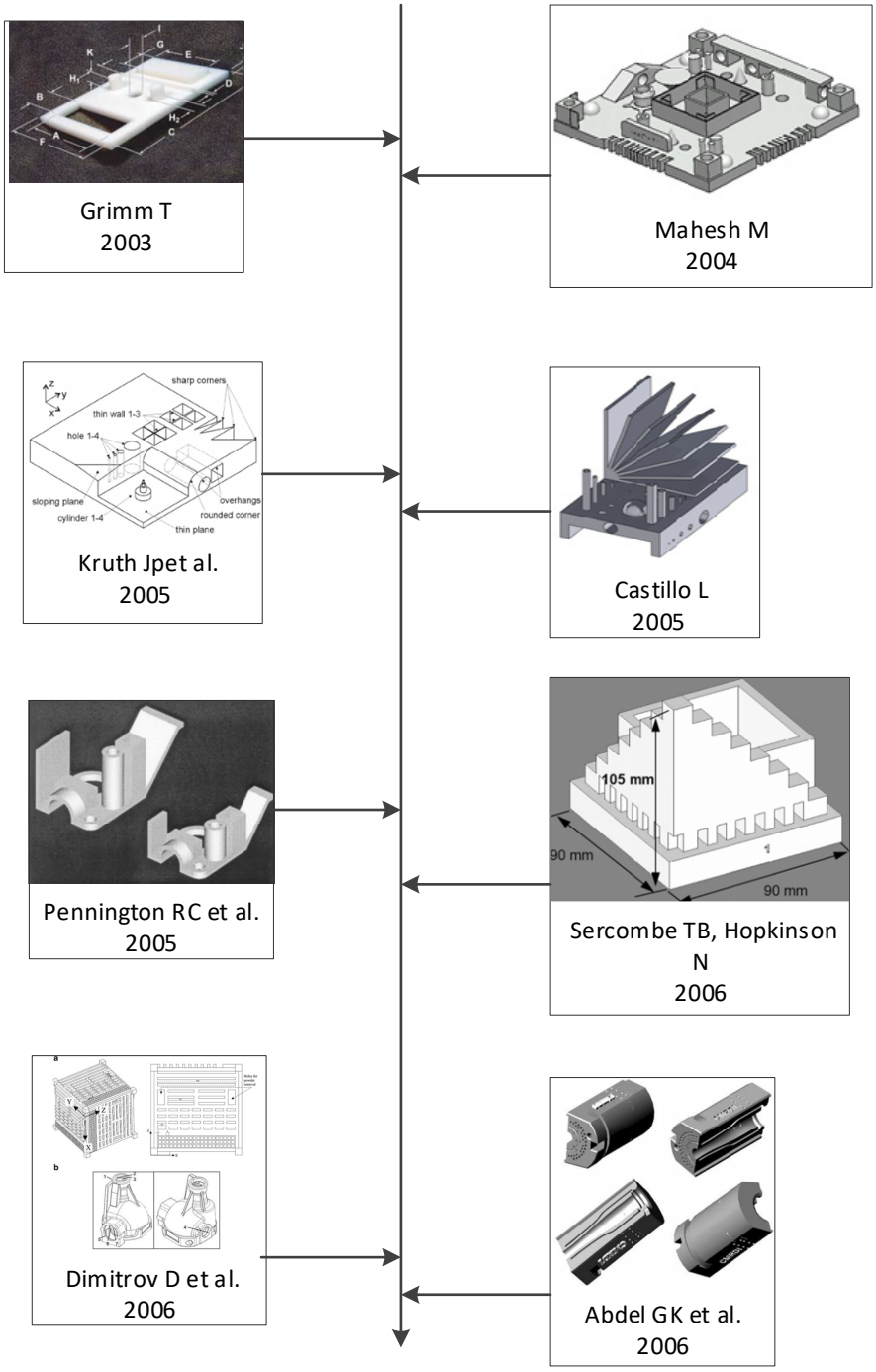
Grimm T
2003
Mahesh M
2004
sharp corners
thin wall 1-3
hole 1-4
sloping plane
cylinder 1-4
overhangs
rounded corner
thin plane
Kruth Jpet al.
2005
Castillo L
2005
Pennington RC et al.
2005
105 mm
90 mm
90 mm
Sercombe TB, Hopkinson N
2006
Dimitrov D et al.
2006
Abdel GK et al.
2006

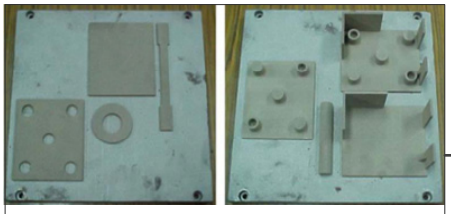

Hanumaiah N, Ravi B
2007

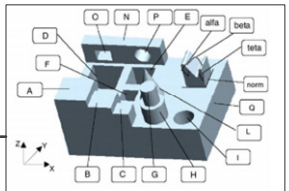

Campanelli SL et al.
2007

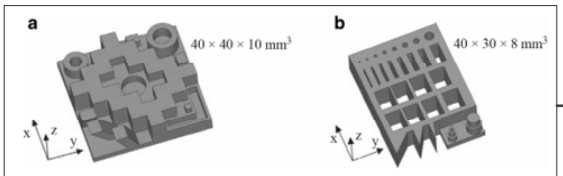

Vandenbroucke B, Kruth JP 2007

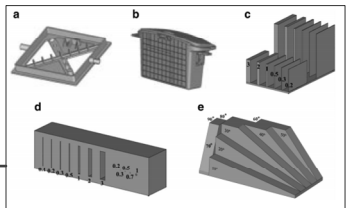

Kim GD, Oh YT 2008

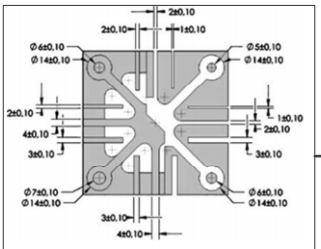

Pessard E et al.
2008

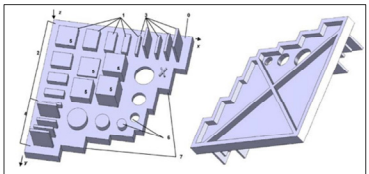

Scaravetti D, Dubois P,
Duchamp R
2008

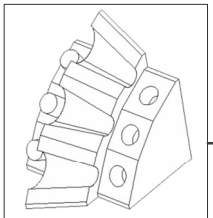

Kotlinski J et al.
2009

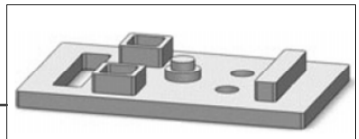

Espalin D & al.
2009

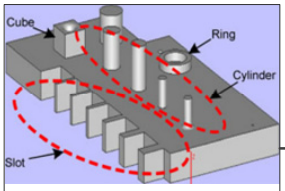

Bakar NSA and al.
2010

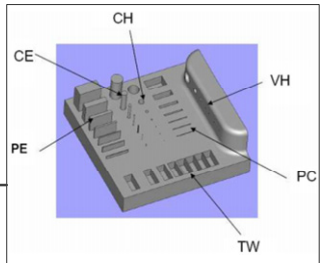

Campanelli SL and al.
2010

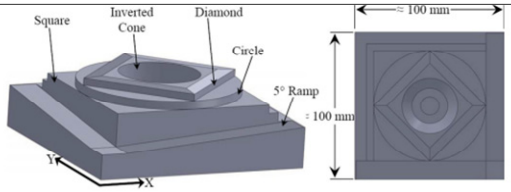

Cooke AL, Soons JA
2010

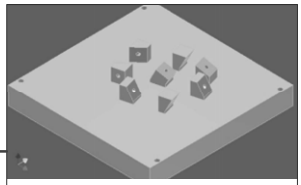

Delgado J, Ciurana J,
Reguant C, Cavallini B
2010

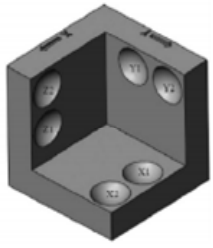

Brajlih T at al.
2011

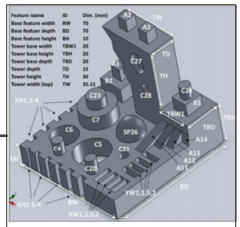

Johnson WM et al.
2011

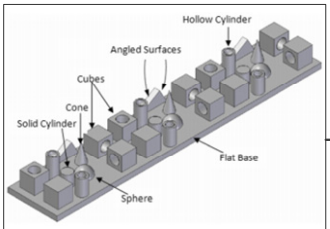

Fahad M, Hopkinson N
2012

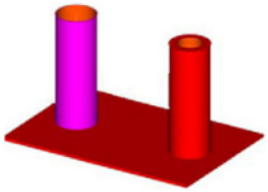

Saqib S, Urbanic J (2012)

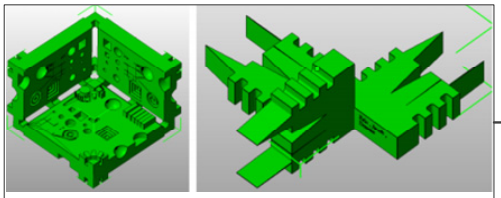

Williams CB, Seepersad CC (2012)

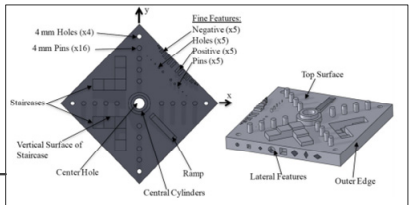

Moylan S,et al.
2012

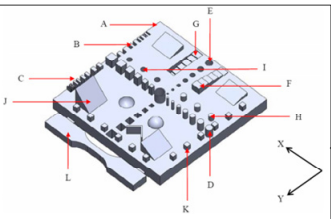

Perez MA, et al.
2013

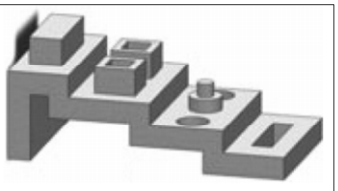

Roberson DA, et al.
2013

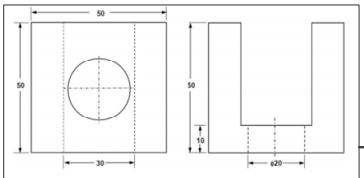

Islam MN, Boswell B, Pramanik A
(2013)

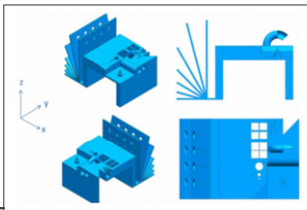

Yasa E, et al.
2014

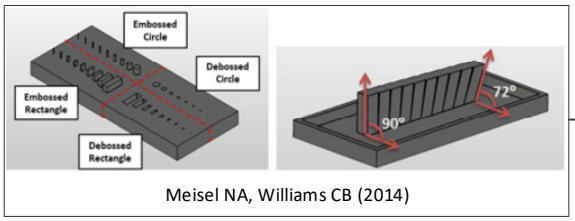

Meisel NA, Williams CB (2014)

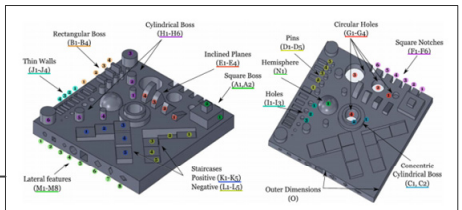

Cruz Sanchez FA, Boudaoud H, Muller L, Camargo M (2014)

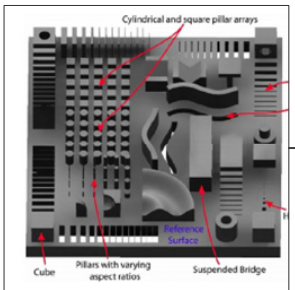

Hao B et al. 2014

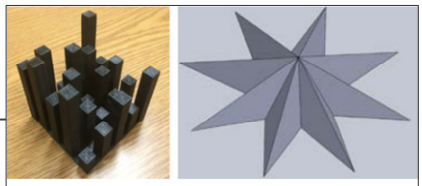

Jared BH, Tran HD, Saiz D, Boucher CL, Dinardo JE (2014)

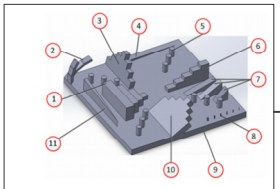

Yang L, Anam MA (2014)

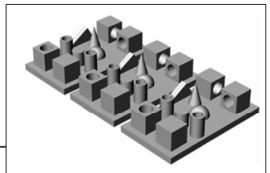

Lanzotti A, et al. (2015)

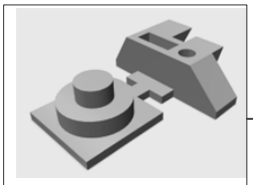

Decker N, Yee A (2015)

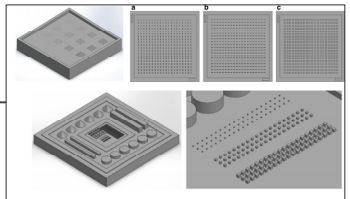

Thompson MK, Mischkot M (2015)

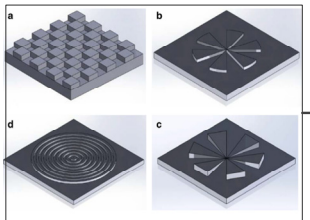

Chang S, Li H, Ostrout N, Jhuria M (2015)

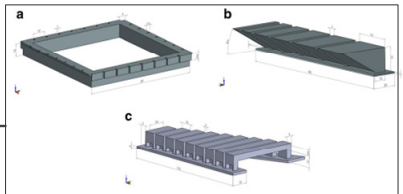

Fernandez-Vicente M et al. (2015)

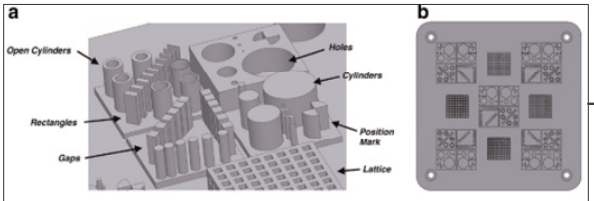

Teeter MG, Kopacz AJ, Nikolov HN, Holdsworth DW (2015)

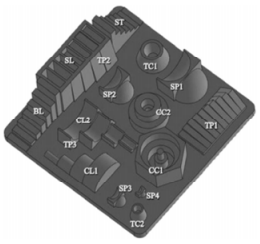

Minetola P, Iuliano L, Marchiandi G (2016)

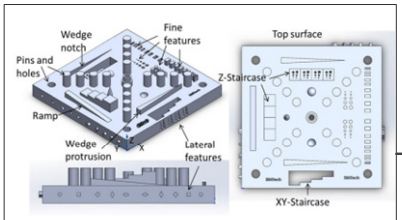

Yang H, et al. (2016)

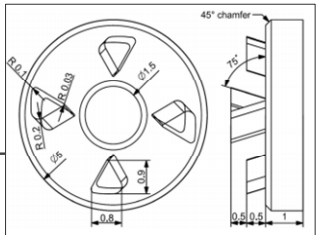

Kniepkamp M, Fischer J, Abele E (2016)

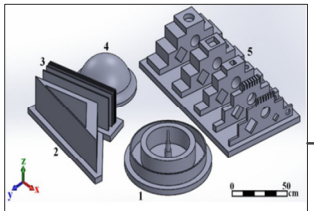

Berger A, Sharon Y, Ashkenazi D, Stern A (2016)

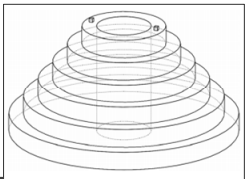

Islam MN, Sacks S (2016)

Calignano F, et al. 2017

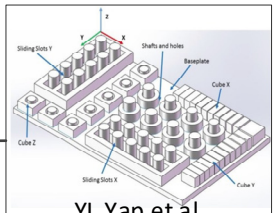

YL Yap et al. (2017)

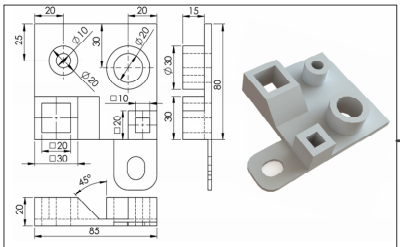

J Kacmarcik et al. (2018)

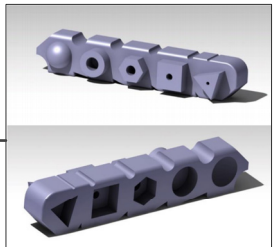

Gulanova et al. (2018)

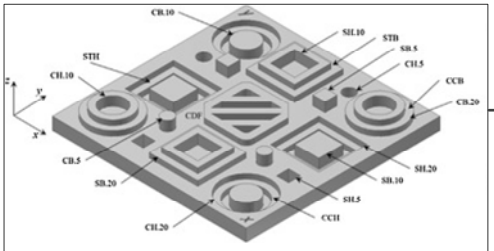

Shahrain et al. 2018

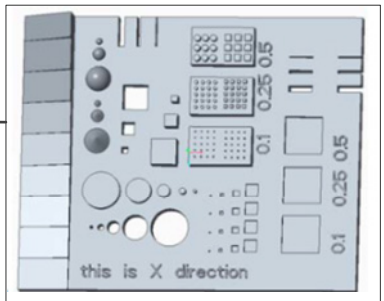

Dotchev et Dotcheva (2019)

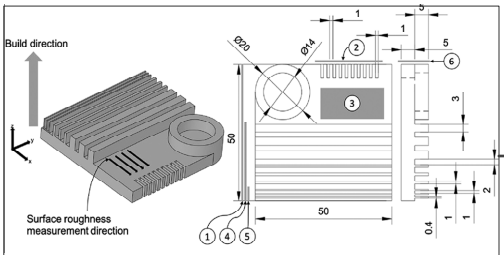

Mou et Koc (2019)

LISTE DE RÉFÉRENCES BIBLIOGRAPHIQUES

1. ASTM, I., *ASTM52901-16 Standard Guide for Additive Manufacturing–General Principles–Requirements for Purchased AM Parts.* ASTM International, West Conshohocken, PA, 2016.
2. DIN, E., *ISO/ASTM 52900: 2017-06 Additive manufacturing—General principles—Terminology (ISO/ASTM 52900: 2015)*. German version EN ISO/ASTM, 2017. **52900**.
3. Mahesh, M., et al. *Benchmarking for decision making in rapid prototyping systems*. in *Automation Science and Engineering, 2005. IEEE International Conference on*. 2005. IEEE.
4. Richter, J. and P. Jacobs, *Accuracy.* Rapid Prototyping & Manufacturing, P. Jacobs, Society of Manufacturing Engineers, 1992: p. 287-315.
5. Byun, H.-S. and K.H. Lee. *Design of a new test part for benchmarking the accuracy and surface finish of rapid prototyping processes*. in *International Conference on Computational Science and Its Applications*. 2003. Springer.
6. Kruth, J.-P., et al., *Benchmarking of different SLS/SLM processes as rapid manufacturing techniques.* Proceedings of the International Conference Polymers & Moulds Innovations PMI*,* 2005.
7. Moylan, S., et al. *Proposal for a standardized test artifact for additive manufacturing machines and processes*. in *Proceedings of the 2012 annual international solid freeform fabrication symposium*. 2012. Austin, TX.
8. Loose, K. and T. Nakagawa. *Benchmarking various methods of layer manufacturing systems in Rapid Prototyping*. in *15th Rapid Prototyping Symposium, Japan Society of Die and Mould Technology (JSDMT)*. 1998.
9. Zhou, J.G., D. Herscovici, and C.C. Chen, *Parametric process optimization to improve the accuracy of rapid prototyped stereolithography parts.* International Journal of Machine Tools and Manufacture, 2000. **40**(3): p. 363-379.
10. Xu, F., Y. Wong, and H. Loh, *Toward generic models for comparative evaluation and process selection in rapid prototyping and manufacturing.* Journal of Manufacturing Systems, 2001. **19**(5): p. 283-296.
11. Grimm, T., *Fused deposition modelling: a technology evaluation.* Time-compression technologies, 2003. **11**(2): p. 1-6.
12. Castillo, L., *Study about the rapid manufacturing of complex parts of stainless steel and titanium.* TNO report with the collaboration of AIMME, 2005.
13. Pennington, R., N. Hoekstra, and J. Newcomer, *Significant factors in the dimensional accuracy of fused deposition modelling.* Proceedings of the Institution of Mechanical Engineers, Part E: Journal of Process Mechanical Engineering, 2005. **219**(1): p. 89-92.
14. Sercombe, T.B. and N. Hopkinson, *Process shrinkage and accuracy during indirect laser sintering of aluminium.* Advanced engineering materials, 2006. **8**(4): p. 260-264.
15. Dimitrov, D., et al., *Investigating the achievable accuracy of three dimensional printing.* Rapid Prototyping Journal, 2006. **12**(1): p. 42-52.
16. Hanumaiah, N. and B. Ravi, *Rapid tooling form accuracy estimation using region elimination adaptive search based sampling technique.* Rapid Prototyping Journal, 2007. **13**(3): p. 182-190.

17. Vandenbroucke, B. and J.-P. Kruth, *Selective laser melting of biocompatible metals for rapid manufacturing of medical parts.* Rapid Prototyping Journal, 2007. **13**(4): p. 196-203.
18. Kim, G. and Y. Oh, *A benchmark study on rapid prototyping processes and machines: quantitative comparisons of mechanical properties, accuracy, roughness, speed, and material cost.* Proceedings of the Institution of Mechanical Engineers, Part B: Journal of Engineering Manufacture, 2008. **222**(2): p. 201-215.
19. Pessard, E., et al., *Complex cast parts with rapid tooling: rapid manufacturing point of view.* The International Journal of Advanced Manufacturing Technology, 2008. **39**(9): p. 898-904.
20. Scaravetti, D., P. Dubois, and R. Duchamp, *Qualification of rapid prototyping tools: proposition of a procedure and a test part.* The International Journal of Advanced Manufacturing Technology, 2008. **38**(7-8): p. 683-690.
21. Kotlinski, J., et al., *Dimensional deviations of machine parts produced in laser sintering technology.* International Journal of Rapid Manufacturing, 2009. **1**(1): p. 88-98.
22. Espalin, D., et al. *Effects of vapor smoothing on ABS part dimensions*. in *Proceedings from Rapid 2009 Conference & Exposition, Schaumburg, IL*. 2009.
23. Bakar, N.S.A., M.R. Alkahari, and H. Boejang, *Analysis on fused deposition modelling performance.* Journal of Zhejiang University-Science A, 2010. **11**(12): p. 972-977.
24. Campanelli, S.L., et al., *Capabilities and performances of the selective laser melting process*, in *New Trends in Technologies: Devices, Computer, Communication and Industrial Systems*. 2010, InTech.
25. Cooke, A.L. and J.A. Soons. *Variability in the geometric accuracy of additively manufactured test parts*. in *Proceedings of 21st Annual International Solid Freeform Fabrication Symposium, Austin, TX*. 2010.
26. Johnson, W., et al. *Benchmarking evaluation of an open source fused deposition modeling additive manufacturing system*. in *Proceeding of the 22nd annual international solid freeform fabrication symposium*. 2011.
27. Fahad, M. and N. Hopkinson. *A new benchmarking part for evaluating the accuracy and repeatability of Additive Manufacturing (AM) processes*. in *2nd International Conference on Mechanical, Production and Automobile Engineering (ICMPAE 2012), Singapore, Apr*. 2012.
28. Williams, C.B. and C.C. Seepersad. *Design for additive manufacturing curriculum: A problem-and project-based approach*. in *International solid freeform fabrication symposium*. 2012. Austin, TX.
29. Roberson, D., D. Espalin, and R. Wicker, *3D printer selection: A decision-making evaluation and ranking model.* Virtual and Physical Prototyping, 2013. **8**(3): p. 201-212.
30. Yasa, E., et al. *Benchmarking of different powder-bed metal fusion processes for machine selection in additive manufacturing*. in *Proceedings of International Solid Freeform Fabrication Symposium*. 2014.
31. Meisel, N.A. and C.B. Williams. *Design for Additive Manufacturing: an investigation of key manufacturing considerations in multi-material PolyJet 3D printing*. in

Proceedings of the 25th Annual international solid freeform fabrication Symposium, Austin (TX), USA. 2014.

32. Cruz Sanchez, F.A., et al., *Towards a standard experimental protocol for open source additive manufacturing: This paper proposes a benchmarking model for evaluating accuracy performance of 3D printers.* Virtual and Physical Prototyping, 2014. **9**(3): p. 151-167.
33. Lanzotti, A., et al., *On the geometric accuracy of RepRap open-source three-dimensional printer.* Journal of Mechanical Design, 2015. **137**(10): p. 101703.
34. Thompson, M.K. and M. Mischkot, *Design of test parts to characterize micro additive manufacturing processes.* Procedia CIRP, 2015. **34**: p. 223-228.
35. Kruth, J.-P., *Material incress manufacturing by rapid prototyping techniques.* CIRP Annals-Manufacturing Technology, 1991. **40**(2): p. 603-614.
36. Lart, G. *Comparison of rapid prototyping systems*. in *Proceedings of First European Conference on Rapid Prototyping, University of Nottingham, Nottingham, UK, July*. 1992.
37. Van Putte, D.A. *A brief benchmarking study of rapid prototyping processes*. in *Third International Conference on Rapid Prototyping Datton*. 1992.
38. Childs, T. and N. Juster, *Linear and geometric accuracies from layer manufacturing.* CIRP Annals-Manufacturing Technology, 1994. **43**(1): p. 163-166.
39. Aubin, R.F., *A world wide assessment of rapid prototyping technologies.* United Technologies Research Center Report, East Hartford, CT, Report, 1994(94-13).
40. Iuliano, L., R. Ippolito, and A. De Filippi, *A new user part for performances evaluation of rapid prototyping systems.* 1994.
41. Reeves, P. and R. Cobb. *Surface deviation modeling of LMT processes—A comparative analysis*. in *Proceedings of the Fifth European Conference on Rapid Prototyping and Manufacturing, Helsinki, Finland, June*. 1995.
42. Fernandez-Vicente, M., M. Canyada, and A. Conejero, *Identifying limitations for design for manufacturing with desktop FFF 3D printers.* International Journal of Rapid Manufacturing, 2015. **5**(1): p. 116-128.
43. Meisel, N. and C. Williams, *An investigation of key design for additive manufacturing constraints in multimaterial three-dimensional printing.* Journal of Mechanical Design, 2015. **137**(11): p. 111406.
44. Islam, M.N. and S. Sacks, *An experimental investigation into the dimensional error of powder-binder three-dimensional printing.* The International Journal of Advanced Manufacturing Technology, 2016. **82**(5-8): p. 1371-1380.
45. Kniepkamp, M., J. Fischer, and E. Abele. *Dimensional accuracy of small parts manufactured by micro selective laser melting*. in *Proceedings of the 27th Annual International Solid Freeform Fabrication Symposium, Austin (TX), USA*. 2016.
46. Minetola, P., L. Iuliano, and G. Marchiandi, *Benchmarking of FDM machines through part quality using IT grades.* Procedia CIRP, 2016. **41**: p. 1027-1032.
47. Calignano, F., et al., *Investigation of accuracy and dimensional limits of part produced in aluminum alloy by selective laser melting.* The International Journal of Advanced Manufacturing Technology, 2017. **88**(1-4): p. 451-458.
48. Yap, Y.L., et al., *Material jetting additive manufacturing: An experimental study using designed metrological benchmarks.* Precision engineering, 2017. **50**: p. 275-285.

49. Kacmarcik, J., et al. *An investigation of geometrical accuracy of desktop 3D printers using CMM*. in *IOP Conference Series: Materials Science and Engineering*. 2018. IOP Publishing.
50. Gulanová, J., et al., *A comparative study of various AM technologies based on their accuracy.* Procedia CIRP, 2018. **67**: p. 238-243.
51. Mahmood, S., A. Qureshi, and D. Talamona, *Taguchi based process optimization for dimension and tolerance control for fused deposition modelling.* Additive Manufacturing, 2018. **21**: p. 183-190.
52. Dotchev, K. and M. Dotcheva, *Investigation of additive manufacturing processes to fabricate small components with mezzo features.* Procedia CIRP, 2019. **79**: p. 119-124.
53. Mou, Y.A. and M. Koc, *Dimensional capability of selected 3DP technologies.* Rapid Prototyping Journal, 2019.
54. Pillet, M., *Les plans d'expériences par la méthode Taguchi*. 2000: Maurice Pillet.
55. Raghunath, N. and P.M. Pandey, *Improving accuracy through shrinkage modelling by using Taguchi method in selective laser sintering.* International journal of machine tools and manufacture, 2007. **47**(6): p. 985-995.
56. Silva, D.N., et al., *Dimensional error in selective laser sintering and 3D-printing of models for craniomaxillary anatomy reconstruction.* Journal of cranio-maxillofacial surgery, 2008. **36**(8): p. 443-449.
57. Teeter, M.G., et al., *Metrology test object for dimensional verification in additive manufacturing of metals for biomedical applications.* Proceedings of the Institution of Mechanical Engineers, Part H: Journal of Engineering in Medicine, 2015. **229**(1): p. 20-27.
58. Basalah, A., et al., *Characterizations of additive manufactured porous titanium implants.* Journal of Biomedical Materials Research Part B: Applied Biomaterials, 2012. **100**(7): p. 1970-1979.
59. Hao, B., et al., *a novel test artifact for performance evaluation of additive manufacturing processes,* American Society for Precision Engineering Conference 2014.
60. Ferrar, B., et al., *Gas flow effects on selective laser melting (SLM) manufacturing performance.* Journal of Materials Processing Technology, 2012. **212**(2): p. 355-364.
61. Singh, S., V.S. Sharma, and A. Sachdeva, *Optimization and analysis of shrinkage in selective laser sintered polyamide parts.* Materials and Manufacturing Processes, 2012. **27**(6): p. 707-714.
62. Senthilkumaran, K., P.M. Pandey, and P. Rao, *New model for shrinkage compensation in selective laser sintering.* Virtual and Physical Prototyping, 2009. **4**(2): p. 49-62.
63. Van Bael, S., et al., *Micro-CT-based improvement of geometrical and mechanical controllability of selective laser melted Ti6Al4V porous structures.* Materials Science and Engineering: A, 2011. **528**(24): p. 7423-7431.
64. Vanderesse, N., et al., *Image analysis characterization of periodic porous materials produced by additive manufacturing.* Materials & Design, 2016. **92**: p. 767-778.
65. Mercelis, P., *Residual stresses in selective laser sintering and selective laser melting.* Rapid Prototyping Journal, 2006. **12**(5): p. 254-265.

66. Mukherjee, T., W. Zhang, and T. DebRoy, *An improved prediction of residual stresses and distortion in additive manufacturing.* Computational Materials Science, 2017. **126**: p. 360-372.
67. Engineers, A.S.o.M., *Mathematical Definition of Dimensioning and Tolerancing Principles: ASME Y14. 5.1 M-1994*. 1995: American Society of Mechanical Engineers.
68. GmbH, E.O.S., *Material Data Sheet: EOS Aluminium AlSi10Mg (for EOS M280).* 2016: p. 5.
69. Wohlers, T. and T. Caffrey, *Wohlers Report 2017: Additive Manufacturing and 3D Printing State of the Industry.* Annual Worldwide Progress Report, 2017.
70. Shiomi, M., et al., *Residual stress within metallic model made by selective laser melting process.* CIRP Annals-Manufacturing Technology, 2004. **53**(1): p. 195-198.
71. Wang, X., *Calibration of shrinkage and beam offset in SLS process.* Rapid Prototyping Journal, 1999. **5**(3): p. 129-133.
72. Zhu, H., L. Lu, and J. Fuh, *Study on shrinkage behaviour of direct laser sintering metallic powder.* Proceedings of the Institution of Mechanical Engineers, Part B: Journal of Engineering Manufacture, 2006. **220**(2): p. 183-190.
73. Galovskyi B, H.T., *Testing Workpieces for Selective Laser Sintering.* Proceedings of ASPE 2015 Spring Topical Meeting, 2015: p. 89-94.
74. Silva, D.N., et al., *Dimensional error in selective laser sintering and 3D-printing of models for craniomaxillary anatomy reconstruction.* Journal of Cranio-Maxillo-Facial Surgery, 2008. **36**(8): p. 443-449.
75. Abdel Ghany, K. and S. Moustafa, *Comparison between the products of four RPM systems for metals.* Rapid Prototyping Journal, 2006. **12**(2): p. 86-94.
76. Aidibe, A., A. Tahan, and V. Brailovski, *Metrological investigation of a selective laser melting additive manufacturing system: A case study.* IFAC-PapersOnLine, 2016. **49**(31): p. 25-29.
77. Rebaioli, L. and I. Fassi, *A review on benchmark artifacts for evaluating the geometrical performance of additive manufacturing processes.* The International Journal of Advanced Manufacturing Technology, 2017. **93**(5-8): p. 2571-2598.
78. Sing, S.L., F.E. Wiria, and W.Y. Yeong, *Selective laser melting of lattice structures: A statistical approach to manufacturability and mechanical behavior.* Robotics and Computer-Integrated Manufacturing, 2018. **49**: p. 170-180.
79. Calignano, F., *Investigation of the accuracy and roughness in the laser powder bed fusion process.* Virtual and Physical Prototyping, 2018. **13**(2): p. 97-104.
80. Wilcox, R., *Kolmogorov–smirnov test.* Encyclopedia of biostatistics, 2005.
81. Mooney, C.Z., *Monte carlo simulation*. Vol. 116. 1997: Sage Publications.
82. Standard, A., *ISO/ASTM 52900: 2015 Additive manufacturing-General principles-terminology.* ASTM F2792-10e1, 2012.
83. Huang, Q., et al., *Statistical predictive modeling and compensation of geometric deviations of three-dimensional printed products.* Journal of Manufacturing Science and Engineering, 2014. **136**(6): p. 061008.
84. Zongo, F., et al., *Intra-and inter-repeatability of profile deviations of an AlSi10Mg tooling component manufactured by laser powder bed fusion.* Journal of Manufacturing and Materials Processing, 2018. **2**(3): p. 56.

85. Calignano, F., et al., *Investigation of accuracy and dimensional limits of part produced in aluminum alloy by selective laser melting.* The International Journal of Advanced Manufacturing Technology, 2017. **88**(1-4): p. 451-458.
86. Li, C., et al., *Microstructure and mechanical properties of TiC/AlSi10Mg alloy fabricated by laser additive manufacturing under high-frequency micro-vibration.* Journal of Alloys and Compounds, 2019.
87. Liu, B., et al., *Performance Consistency of AlSi10Mg Alloy Manufactured by Simulating Multi Laser Beam Selective Laser Melting (SLM): Microstructures and Mechanical Properties.* Materials, 2018. **11**(12): p. 2354.
88. Del Re, F., et al., *Statistical approach for assessing the effect of powder reuse on the final quality of AlSi10Mg parts produced by laser powder bed fusion additive manufacturing.* The International Journal of Advanced Manufacturing Technology, 2018. **97**(5-8): p. 2231-2240.
89. Panda, B.K. and S. Sahoo, *Thermo-mechanical modeling and validation of stress field during laser powder bed fusion of AlSi10Mg built part.* Results in Physics, 2019. **12**: p. 1372-1381.
90. Brailovski, A.A.A.T.V., *A Novel Industrial Test Artifact for the Evaluation of Dimensional Capabilities of MetallicAdditive Manufacturing Systems.* © European Powder Metallurgy Association (EPMA), 2018(Euro PM2018): p. 6.
91. Liu, J., et al., *A review of computational modeling in powder-based additive manufacturing for metallic part qualification.* Rapid Prototyping Journal, 2018. **24**(8): p. 1245-1264.
92. Afazov, S., et al., *A methodology for precision additive manufacturing through compensation.* Precision Engineering, 2017. **50**: p. 269-274.
93. An, K., et al., *Neutron residual stress measurement and numerical modeling in a curved thin-walled structure by laser powder bed fusion additive manufacturing.* Materials & design, 2017. **135**: p. 122-132.
94. Caelers, M., *Study of in-situ monitoring methods to create a robust SLM process: Preventing collisions between recoater mechanism and part in a SLM machine*. 2017.
95. Nicoletto, G., *Anisotropic high cycle fatigue behavior of Ti–6Al–4V obtained by powder bed laser fusion.* International Journal of Fatigue, 2017. **94**: p. 255-262.
96. Gan, M.X. and C.H. Wong, *Practical support structures for selective laser melting.* Journal of Materials Processing Technology, 2016. **238**: p. 474-484.
97. Moges, T., G. Ameta, and P. Witherell, *A Review of Model Inaccuracy and Parameter Uncertainty in Laser Powder Bed Fusion Models and Simulations.* Journal of manufacturing science and engineering, 2019. **141**(4): p. 040801.
98. Dunbar, A.J., et al., *Experimental validation of finite element modeling for laser powder bed fusion deformation.* Additive Manufacturing, 2016. **12**: p. 108-120.
99. Mercelis, P. and J.-P. Kruth, *Residual stresses in selective laser sintering and selective laser melting.* Rapid prototyping journal, 2006. **12**(5): p. 254-265.
100. Denlinger, E.R., et al., *Thermomechanical model development and in situ experimental validation of the Laser Powder-Bed Fusion process.* Additive Manufacturing, 2017. **16**: p. 73-80.

101. François, M., et al., *Design for additive manufacturing (DfAM) methodologies: a proposal to foster the design of microwave waveguide components.* Virtual and Physical Prototyping, 2019. **14**(2): p. 175-187.
102. TC69, I., *SC4–Applications of statistical methods in process management: ISO*. 2013, TR 22514-4: 2007-Statistical methods in process management–Capability and performance–Part 4: Process capability estimates and performance measures. Published standard.
103. ANSYS, *ANSYS Additive User's Guide Release 19.2.* 2018: p. 62.
104. Jun-mei, C., et al., *Prediction of Welding Deformation With Inherent Strain Method Based On FEM*. Area.
105. Wang, Y.-X., et al., *Inherent strain method and thermal elastic-plastic analysis of welding deformation of a thin-wall beam.* Journal of Mechanics, 2008. **24**(4): p. 301-309.
106. ANSYS, *ANSYS Additive Print Calibration Guide Release 19.2.* 2018: p. 18.
107. Wang, J., S.R. Sama, and G. Manogharan, *Re-Thinking Design Methodology for Castings: 3D Sand-Printing and Topology Optimization.* International Journal of Metalcasting, 2019. **13**(1): p. 2-17.
108. *Aluminum A360.0-F Die Casting Alloy*. Available from: http://www.matweb.com/search/DataSheet.aspx?MatGUID=87a0d0817ebd44008a967cbf3e9cd378&ckck=1.
109. Dixon, W.J. and F.J. Massey Jr, *Introduction to statistical analysis.* 1951.
110. Barbero, B.R. and E.S. Ureta, *Comparative study of different digitization techniques and their accuracy.* Computer-Aided Design, 2011. **43**(2): p. 188-206.
111. Kessel, W., *Measurement uncertainty according to ISO/BIPM-GUM.* Thermochimica Acta, 2002. **382**(1-2): p. 1-16.
112. Zhu, Z., N. Anwer, and L. Mathieu, *Statistical Modal Analysis for Out-of-Plane Deviation Prediction in Additive Manufacturing Based on Finite Element Simulation.* Journal of Manufacturing Science and Engineering, 2019. **141**(11).